Simulation de la mise en forme de renforts NCF de composites basée sur des approches mesoscopiques

Ruochen Zheng

N°d'ordre NNT : 2023ISAL0128

THESE de DOCTORAT DE L'INSA LYON,
L'Institut National des Sciences Appliquées de Lyon

Ecole Doctorale N° 162
Mécanique, Energétique, Génie civil, Acoustique

Spécialité/ discipline de doctorat :

Génie Mécanique

Soutenue publiquement le 14/12/2023, par :
Ruochen ZHENG

Simulation de la mise en forme de renforts NCF de composites basée sur des approches mesoscopiques

---

Devant le jury composé de :

HIVET Gilles	Professeur, Polytech Orléans	Examinateur
MOULIN Nicolas	Professeur, Mines Saint-Étienne	Rapporteur
GAUTIER Karine	HDR, Université de Haute-Alsace	Rapporteure
MORESTIN Fabrice	Professeur, INSA Lyon	Directeur de thèse
NAOUAR Naim	Chargé de Recherche – CNRS, INSA Lyon	Co-directeur de thèse
COLMARS Julien	Maître de conférences, INSA Lyon	Co-encadrant de thèse
PLATZER Auriane	Maîtresse de conférences, INSA Lyon	Co-encadrante de thèse
KÄRGER Luise	Professeure, Karlsruhe Institute of Technology	Invitée
BOISSE Philippe	Professeur, INSA Lyon	Invité

Département FEDORA – INSA Lyon - Ecoles Doctorales

SIGLE	ECOLE DOCTORALE	NOM ET COORDONNEES DU RESPONSABLE
ED 206 CHIMIE	**CHIMIE DE LYON** https://www.edchimie-lyon.fr Sec. : Renée EL MELHEM Bât. Blaise PASCAL, 3e étage secretariat@edchimie-lyon.fr	**M. Stéphane DANIELE** C2P2-CPE LYON-UMR 5265 Bâtiment F308, BP 2077 43 Boulevard du 11 novembre 1918 69616 Villeurbanne directeur@edchimie-lyon.fr
ED 341 E2M2	**ÉVOLUTION, ÉCOSYSTÈME, MICROBIOLOGIE, MODÉLISATION** http://e2m2.universite-lyon.fr Sec. : Bénédicte LANZA Bât. Atrium, UCB Lyon 1 Tél : 04.72.44.83.62 secretariat.e2m2@univ-lyon1.fr	**Mme Sandrine CHARLES** Université Claude Bernard Lyon 1 UFR Biosciences Bâtiment Mendel 43, boulevard du 11 Novembre 1918 69622 Villeurbanne CEDEX e2m2.codir@listes.univ-lyon1.fr
ED 205 EDISS	**INTERDISCIPLINAIRE SCIENCES-SANTÉ** http://ediss.universite-lyon.fr Sec. : Bénédicte LANZA Bât. Atrium, UCB Lyon 1 Tél : 04.72.44.83.62 secretariat.ediss@univ-lyon1.fr	**Mme Sylvie RICARD-BLUM** Laboratoire ICBMS - UMR 5246 CNRS - Université Lyon 1 Bâtiment Raulin - 2ème étage Nord 43 Boulevard du 11 novembre 1918 69622 Villeurbanne Cedex Tél : +33(0)4 72 44 82 32 sylvie.ricard-blum@univ-lyon1.fr
ED 34 EDML	**MATÉRIAUX DE LYON** http://ed34.universite-lyon.fr Sec. : Yann DE ORDENANA Tél : 04.72.18.62.44 yann.de-ordenana@ec-lyon.fr	**M. Stéphane BENAYOUN** Ecole Centrale de Lyon Laboratoire LTDS 36 avenue Guy de Collongue 69134 Ecully CEDEX Tél : 04.72.18.64.37 stephane.benayoun@ec-lyon.fr
ED 160 EEA	**ÉLECTRONIQUE, ÉLECTROTECHNIQUE, AUTOMATIQUE** https://edeea.universite-lyon.fr Sec. : Philomène TRECOURT Bâtiment Direction INSA Lyon Tél : 04.72.43.71.70 secretariat.edeea@insa-lyon.fr	**M. Philippe DELACHARTRE** INSA LYON Laboratoire CREATIS Bâtiment Blaise Pascal, 7 avenue Jean Capelle 69621 Villeurbanne CEDEX Tél : 04.72.43.88.63 philippe.delachartre@insa-lyon.fr
ED 512 INFOMATHS	**INFORMATIQUE ET MATHÉMATIQUES** http://edinfomaths.universite-lyon.fr Sec. : Renée EL MELHEM Bât. Blaise PASCAL, 3e étage Tél : 04.72.43.80.46 infomaths@univ-lyon1.fr	**M. Hamamache KHEDDOUCI** Université Claude Bernard Lyon 1 Bât. Nautibus 43, Boulevard du 11 novembre 1918 69 622 Villeurbanne Cedex France Tél : 04.72.44.83.69 direction.infomaths@listes.univ-lyon1.fr
ED 162 MEGA	**MÉCANIQUE, ÉNERGÉTIQUE, GÉNIE CIVIL, ACOUSTIQUE** http://edmega.universite-lyon.fr Sec. : Philomène TRECOURT Tél : 04.72.43.71.70 Bâtiment Direction INSA Lyon mega@insa-lyon.fr	**M. Etienne PARIZET** INSA Lyon Laboratoire LVA Bâtiment St. Exupéry 25 bis av. Jean Capelle 69621 Villeurbanne CEDEX etienne.parizet@insa-lyon.fr
ED 483 ScSo	**ScSo**[1] https://edsciencessociales.universite-lyon.fr Sec. : Mélina FAVETON Tél : 04.78.69.77.79 melina.faveton@univ-lyon2.fr	**M. Bruno MILLY** (INSA : J.Y. TOUSSAINT) Univ. Lyon 2 Campus Berges du Rhône 18, quai Claude Bernard 69365 LYON CEDEX 07 Bureau BEL 319 bruno.milly@univ-lyon2.fr

[1] ScSo : Histoire, Géographie, Aménagement, Urbanisme, Archéologie, Science politique, Sociologie, Anthropologie

Remerciements

Avec l'achèvement de la thèse, ma recherche doctorale à l'INSA Lyon touche à sa fin. En regardant en arrière sur ma vie de recherche passée, je tiens à remercier toutes les personnes que j'ai rencontrées au cours de cette période de recherche heureuse et inoubliable en France.

Je tiens tout d'abord à exprimer ma sincère gratitude à mon premier directeur de thèse, le Professeur Philippe Boisse, qui m'a donné l'opportunité de faire cette thèse et m'a guidé au cours de mes deux premières années. J'espère qu'il se rétablira bientôt et qu'il restera en bonne santé.

Je tiens à remercier mon deuxième superviseur, le professeur Fabrice Morestin, pour son encadrement et son aide au cours de ma troisième année. J'aimerais également remercier mon co-directeur de thèse, Dr. Naim Naouar, ainsi que toute l'équipe, Dr. Julien Colmars et Dr. Auriane Platzer, pour leur aimable assistance et leur supervision de la recherche de thèse. Mes remerciements vont également à Professeur Philippe Chaudet pour son aide dans mes expériences.

Merci à l'équipe de KIT, à la Professeure Luise Kärger et à M. Bastian Schäfer, pour leur aide dans le projet AMECOMP.

Je tiens également à remercier mes collègues et amis, Renzi, Bo, Jin, Yining, Chunhui, Baptiste et toutes les autres personnes. Merci pour votre aide, votre participation et vos discussions sur la vie et la recherche.

Enfin, je remercie sincèrement mes parents pour leur soutien spirituel.

Ruochen ZHENG
06/10/2023

Résumé

Titre : Simulation de la mise en forme de renforts NCF de composites basée sur des approches mesoscopiques

Pour parvenir à une fabrication efficace et exempte de défauts de renforts fibreux tout en minimisant la nécessité de tests expérimentaux longs et coûteux, il est nécessaire de développer des techniques de simulation et d'optimisation fiables du procédé de mise en forme. Les renforts composites NCF (Non-Crimp Fabric) promettent des performances structurales exceptionnelles, mais la mise en forme de ces matériaux est délicate. Sa complexité découle des mécanismes de déformation spécifiques de ce type de renforts, principalement influencés par les motifs de couture complexes qui lient subtilement les fibres entre elles. Dans cette étude, nous proposons une approche de modélisation par éléments finis à l'échelle mésoscopique pour relever ce défi. Ici, nous traitons les mèches comme un milieu continu, tandis que les coutures environnantes sont soigneusement représentées à l'aide d'éléments poutres. Pour capturer les caractéristiques de déformation des mèches, nous utilisons une loi hyperélastique, complétée par des éléments poutres intégrés pour découpler leur comportement en flexion. De plus, nous introduisons une étape de précontrainte pour simuler la tension due au tricotage des coutures et modéliser l'interaction complexe entre les mèches et les coutures, en tenant compte des mécanismes de glissement propre aux matériaux NCF.

La crédibilité de notre modèle est attestée par des simulations de déformation en cisaillement dans le plan sur une cellule unitaire et des tests de cisaillement en bias-extension. Ces simulations mettent en évidence la polyvalence du modèle mésoscopique, permettant la caractérisation virtuelle des matériaux et réduisant les efforts expérimentaux généralement requis pour les simulations macroscopiques. De plus, notre approche offre des descriptions explicites des mèches et des coutures basées sur des observations en tomographie et générées à l'aide d'équations paramétriques. Cette fonctionnalité permet l'analyse de différents motifs de couture et de structures de tissu, offrant des opportunités

de personnaliser les matériaux NCF avec un comportement de déformation optimisé pour des applications spécifiques.

Conscient que le changement d'orientation des fibres influence considérablement le comportement mécanique de la pièce composite finale après l'étape de mise en forme, une méthode de post-traitement est proposée sur ce modèle mésoscopique pour suivre la direction des fibres et visualiser l'angle de cisaillement. Un avantage notable de notre approche de modélisation mésoscopique réside dans sa capacité à détecter et à analyser les défauts locaux, tels que le gaping, un défaut majeur dans la mise en forme des NCF difficile à observer directement via des simulations macroscopiques. Par conséquent, le modèle mésoscopique permet l'analyse et la prédiction de la formation et du développement des défauts du gaping, contribuant à améliorer la qualité et l'efficacité de la fabrication.

Abstract

Title : Forming simulation of NCF reinforcements based on mesoscopic approaches

The current challenge in achieving efficient and defect-free manufacturing of fibrous reinforcement while minimizing the need for time-consuming and costly experimental tests lies in the development of reliable simulation and optimization of the forming process. NCF composite reinforcements exhibit exceptional structural performance, but forming of these materials is delicate. The complexity of forming such fabric arises from the specific deformation mechanisms, predominantly influenced by the stitching patterns that intricately bond the fibers. A mesoscopic FE modelling approach is proposed in this study. The fiber yarns are considered as a continuous medium and the surrounding stitches are represented separately using beam elements. A hyperelastic law is used to describe the deformation modes of fiber yarns, supplemented by embedded beam elements to decouple their bending behavior. A pretension step is implemented to replicate the knitting of stitches and model the interaction between the yarns and stitches, considering the slip mechanisms in NCF.

The model is validated through the simulation of in-plane shear deformation on unit cell and on bias-extension test. It demonstrates that the mesoscopic model can be used to conduct virtual material characterization and reduce the experimental effort required for macroscopic simulation. Additionally, the geometry of fiber yarns and stitches are described explicitly through observation from tomography and generated through parametric equations. This allows for the analysis of various stitching patterns and fabric structures, offering opportunities to tailor NCF materials with optimized deformation behavior for specific applications.

Recognizing that the change in fiber orientation significantly influences the mechanical behavior of the final composite part after the forming step, a post-processing method is proposed on this mesoscopic model to track the fiber direction and visualize the shear

angle. A notable advantage of our mesoscopic modeling approach lies in its ability to detect and analyze local defects, such as gaping, a main defect in NCF forming that is challenging to observe directly through macroscopic simulations. Consequently, the mesoscopic model allows for the analysis and prediction of the formation and development of gaping defects, contributing to enhanced manufacturing quality and efficiency.

Contents

List of Figures

List of Tables

Introduction générale

Les composites à fibres continues sont couramment utilisés dans les domaines aéronautique, automobile et maritime en raison de leur grande résistance et de leur légèreté. Parmi les renforts possibles, les Biaxial Non-crimp Fabrics sont une solution intéressante. Ils se composent de deux couches de nappes fibreuses non tissées disposées perpendiculairement, et des coutures de polyester sont utilisées pour percer les deux couches à des positions spécifiques entre les mèches et ainsi les lier ensemble. En raison de leurs excellentes propriétés, les NCFs sont de plus en plus utilisés dans les composants d'aéronefs, tels que les panneaux de fuselage et les structures d'aile, dans le but de réduire le poids et d'améliorer l'efficacité énergétique. Dans le secteur automobile, les NCFs sont utilisés pour réduire le poids des composants structurels. De plus, les NCFs trouvent de plus en plus d'applications dans le secteur des énergies renouvelables, notamment dans la fabrication de pales d'éoliennes, en raison de leur rapport résistance-poids impressionnant et de leur résistance à la fatigue.

Les principaux défis tournent autour des taux de production qui peuvent être atteints avec les processus de fabrication actuels pour les pièces composites. Pour obtenir la pièce composite finale, la mise en forme est une étape clé de la fabrication au cours de laquelle les tissus plats en 2D sont façonnés en une forme 3D et subissent d'importantes déformations. À cette étape, le renfort fibreux est pressé dans un outil conçu pour la géométrie 3D souhaitée, puis de la résine est injectée dans le cadre des processus de moulage de composites liquides (LCM). Les importantes déformations auxquelles il est soumis ont un impact direct sur la perméabilité et les propriétés mécaniques du matériau. Par conséquent, les NCFs sont plus susceptibles de présenter des défauts de la mise en form tels que le gaping, le glissement des coutures et les ondulations des fibres. Afin de parvenir à une fabrication efficace et sans défauts tout en minimisant le besoin d'essais expérimentaux longs et coûteux, il est nécessaire de disposer d'une simulation fiable et d'une optimisation du processus de la mise en forme.

Les renforts fibreux sont des matériaux hautement multi échelles : les phénomènes que nous modélisons dépendent de l'échelle à laquelle le renfort est observé. On distingue

l'échelle microscopique des filaments, l'échelle mésoscopique des mèches et l'échelle macroscopique ou structurale du textile dans son ensemble. Dans la littérature, les approches macroscopiques sont plus couramment utilisées pour prédire le comportement de mise en forme des renforts fibreux, mais elles peuvent rencontrer des difficultés lorsqu'il s'agit de détecter certains défauts locaux, tels que le gaping qui se produit lorsque les deux fils adjacents s'éloignent l'un de l'autre et laissent une zone vide sans fibres. Ces défauts de gaping sont souvent détectés grâce à un résultat numérique de la déformation macroscopique transverse dans le plan. De plus, les glissements mèche-mèche et aussi mèche-couture, qui se produisent généralement sur les NCFs, sont difficiles à observer via une approche macroscopique continue. Une alternative consiste à utiliser des approches microscopiques, où chaque filament du fil de fibres est modélisé à l'aide d'éléments poutres ou solides. Ce micro-modèle est réaliste mais complexe et chronophage. Par conséquent, l'approche mésoscopique est une solution intéressante. À cette échelle, la déformation locale des NCF, telle que la compression de la mèche, le glissement entre les mèches et les coutures, ainsi que le développement du gaping, est visible. L'objectif de ma thèse est d'établir un modèle mésoscopique de Biaxial NCF au sein du logiciel commercial Abaqus. Ce modèle permettra la caractérisation virtuelle des matériaux, l'analyse de différents motifs de couture, la simulation du processus de mise en forme et la détection des défauts de mise en forme.

Le premier chapitre est consacré à la présentation des renforts composites, en mettant particulièrement l'accent sur la structure des composites textiles et le processus de fabrication. On y aborde également le comportement mécanique du renfort fibres ainsi que les approches de simulation à différentes échelles.

Le chapitre 2 introduit la modélisation mésoscopique du NCF biaxial étudié, y compris la modélisation géométrique et mécanique. La modélisation géométrique du NCF biaxial à l'échelle mésoscopique implique la modélisation séparée des coutures et des mèches. Les mèches sont initialement construits sous forme de formes ovales en coupes transversales et sont supposés droits le long de l'orientation des fibres, en négligeant de petites distorsions créées par la tension de la couture. Ses dimensions sont déterminées à l'aide de la tomographie par rayons X. Le modèle de couture est exprimé en fonction du processus de tricotage et à travers une série d'équations en le divisant en segments. La couture en polyester est modélisée comme un matériau élastique linéaire, tandis qu'une loi constitutive hyperélastique développée par Charmetant est utilisée pour la mèche de carbone. Les paramètres du modèle de matériau pour les mèches et les coutures à l'échelle mésoscopique sont identifiés grâce à des essais expérimentaux. La couture est modélisé à l'aide d'un élément d'expansion thermique de section générale, permettant de découpler son comportement en tension et en flexion, ainsi que de modéliser l'interaction entre les mèches et les coutures grâce à une nouvelle étape de précontrainte.

Chapitre 3 présente les méthodes de validation utilisées pour le modèle mésoscopique du NCF biaxial. La simulation débute par l'analyse de la déformation en cisaillement dans le plan d'un modèle de cellule unitaire, qui est la taille la plus petite pour représenter efficacement le comportement du matériau équivalent homogénéisé dans son ensemble. Pour ce faire, des périodicités et des conditions aux limites sont introduites. Un test de

Picture Frame est effectué pour valider les résultats, en supposant qu'une déformation en cisaillement pur se produit. De plus, une simulation de test de biais-extension est réalisée pour mettre en évidence le potentiel du modèle pour des applications à plus grande échelle et la capacité à observer des déformations locales telles que le glissement entre les couches de fibres et la formation du gaping. L'étude compare la force de cisaillement normalisée, l'angle de cisaillement et le développement du gaping.

Dans le chapitre 4, divers types d'essais de mise en forme sont menés en utilisant différentes formes de poinçons, types de tissus et orientations des fibres. La déformation du renfort au cours de la mise en forme est mesurée par corrélation d'images numeriques, en suivante une grille de points blancs qppliquée préablement sur les mèches de carbonne. De plus, une analyse complète est entreprise, en tenant compte des forces de poinçonnage, des contours extérieurs, des déformations macroscopiques et des défauts de mise en forme. Ensuite, des simulations numériques du processus de mise en forme sont effectuées à l'aide du modèle élément fini mésoscopique du NCF biaxial. Lafidélité des modèles est démontrée par comparaison du contour extérieur de la configuration finale et de l'angle de cisaillement avec les résultats expérimentaux. L'apparition de défauts du gaping est également analysée et comparée. La modélisation à l'échelle mésoscopique offre l'avantage supplémentaire d'observer le glissement entre les plis.

General Introduction

Continuous fiber composites are commonly used in aeronautical, automotive and marine applications for their high strength and light weight. Among the possible reinforcements, bi-axial non crimp fabrics (biaxial NCF) are an interesting solution. It consists of two layers of non-woven fibrous plies laid in perpendicular directions and polyester stitches are used to pierce the two plies at specific positions between the fiber yarns and to bond the plies together. Due to their excellent properties, NCFs have become increasingly used in aircraft components, such as fuselage panels and wing structures, with the aim of reducing weight and enhancing fuel efficiency. In the automotive sector, NCFs are employed for weight reduction purposes in structural components. Moreover, NCFs are finding growing application in the renewable energy sector, particularly in the production of wind turbine blades, owing to their impressive strength-to-weight ratio and resistance to fatigue.

The challenges primarily revolve around the production rates that can be achieved using current manufacturing processes for composite parts. To obtain the final composite part, the fabric forming is a key manufacturing step during which 2D flat fabrics are shaped to a 3D shape and undergo large deformations. In this step, the fibrous stack is pressed into a tool designed for the desired 3D geometry, following which resin is injected in liquid composite molding (LCM) processes. The large deformations it undergoes directly impact the reinforcement's permeability and mechanical properties. Thereby, NCFs are more susceptible to forming defects like gaping, rovings slippage and fiber waviness. In order to achieve efficient and defect-free manufacturing while minimizing the need for time-consuming and costly experimental tests, it is necessary to have a reliable simulation and optimization tool of the forming process.

Fibrous reinforcements are highly multi-scale materials: the phenomena we model depend on the scale at which the reinforcement is observed. A distinction is made between

the microscopic scale of filaments, the mesoscopic scale of fiber yarns, and the macroscopic or structural textile scale as a whole. In the literature, macroscopic approaches are more commonly used to predict the forming behavior of fibrous reinforcements, however it may encounter difficulties when seeing some local defects, such as the gaping which occurs when the two adjacent yarns move away from each other and leave an empty zone without fibers. These gaping defects are often detected through a numerical result of the in-plane transverse strain at this macro scale. Furthermore, the slippage of yarn-yarn and also stitch-yarn, which usually occurs on non-crimp-fabrics, is hardly captured by a macroscopic continuous approach. An alternative is using microscopic approaches, where each filament of the fiber yarn is modelled by beam or solid elements. This micro-model is realistic but complex and time-consuming. Therefore, mesoscopic approach is an interesting solution. From the view at this scale, the local deformation of NCFs, such as the yarn's compression, the slippage between yarns and stitches, as well as the development of gap, is visible. The objective of my thesis is to establish a mesoscopic model of biaxial NCF within the commercial Abaqus software. This model will enable virtual material characterization, analysis of various stitching patterns, simulation of the forming process, and detection of forming defects.

The first chapter is dedicated to the presentation of composite reinforcements, with special attention on the structure of textile composite and the manufacturing process. The mechanical behavior of fibrous reinforcement and the simulation approaches at different scales are introduced and discussed.

Chapter 2 introduces the mesoscopic modeling of the studied biaxial NCF, including the geometrical modeling and mechanical modeling. The geometrical modeling of biaxial NCF at a mesoscopic scale involves separate modeling of stitches and fibre yarns. The fibre yarns are initially constructed as oval shapes in cross-sections and are assumed to be straight along the fibre orientation, neglecting small distortions created by the tensioned stitch. Their dimensions are determined using X-ray tomography. The stitch model is expressed based on the knitting process and through a series of equations by dividing it into segments. The polyester stitch is modelled as a linear elastic material, while a hyperelastic constitutive law developed by Charmetant is employed for the carbon fibre yarn. The material model parameters for fiber yarns and stitching at the meso level are identified through experimental tests. The stitch is modeled using a general section thermo expansion element, enabling decoupling of its tension and bending behavior, as well as modeling the interaction between fiber yarns and stitches through a novel pretension step.

Chapter 3 presents the validation methods employed for the mesoscopic model of biaxial NCF. We firstly analyze in-plane shear deformation of a unit cell model, which is the smallest size to effectively represent the behavior of the entire homogenized equivalent material. To achieve this, periodicities and boundary conditions are introduced. A picture frame test was conducted to validate the result, where we assume that pure shear deformation occurs. Additionally, a bias-extension test simulation is carried out to showcase the model's potential for larger scale applications and the ability to observe local deformations such as sliding between fiber layers and the formation of gaps. The

study compares the normalized shear force, shear angle, and development of gaps.

In Chapter 4, various types of forming experiments are conducted using different punch shapes, fabric types, and orientations of the fibers. The deformation behavior of the fabrics is captured throughout the forming process via Digital Image Correlation (DIC) strain measurement. Furthermore, a comprehensive analysis is undertaken, considering punch forces, outer contours, macroscopic strains, and forming defects. Subsequently, numerical simulations of the forming process are conducted using the mesoscopic finite element model of biaxial NCF. The accuracy of the models is validated through a comparison of the final configuration's outer contour and shear angle with experimental results. The occurrence of gaping defects is additionally analyzed and compared. The mesoscale modeling offers the added advantage of observing inter-ply sliding.

Résumé de Thèse en Français

Chapitre 1 Le matériau composite et sa modélisation numérique

1.1 Introduction au matériau composite

En général, un matériau composite est formé en combinant deux ou plusieurs composants pour créer un matériau supérieur aux performances améliorées. Cette définition large englobe une grande variété de matériaux, y compris à la fois des substances naturelles utilisées depuis longtemps, telles que le bois, les os ou le torchis, ainsi que des innovations modernes comme les pneus ou le béton armé. La caractéristique définissante de tous ces matériaux est qu'ils se composent de deux phases principales : la phase de renforcement, responsable de la maîtrise des propriétés mécaniques du produit final, et la phase de matrice, qui assure la cohésion de toute la structure en incorporant des fibres ou des particules.

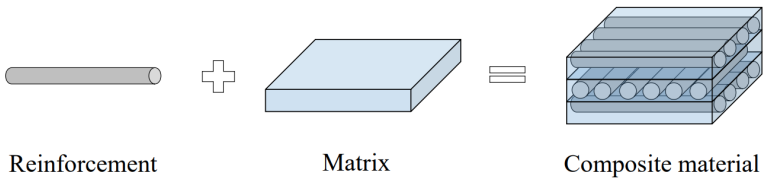

Fig. 1: Composition des matériaux composites [1]

Non crimp fabrics (NCFs) sont l'un des types de renforts les plus prometteurs pour la fabrication de pièces composites dans les industries automobile et aéronautique. Par rapport aux tissus tissés, les NCFs offrent un potentiel encore plus élevé en termes de légèreté. Les fibres dans les NCF sont droites, sans les ondulations que l'on trouve dans les tissus tissés. Leurs propriétés mécaniques peuvent être adaptées pour répondre aux exigences spécifiques de diverses applications.

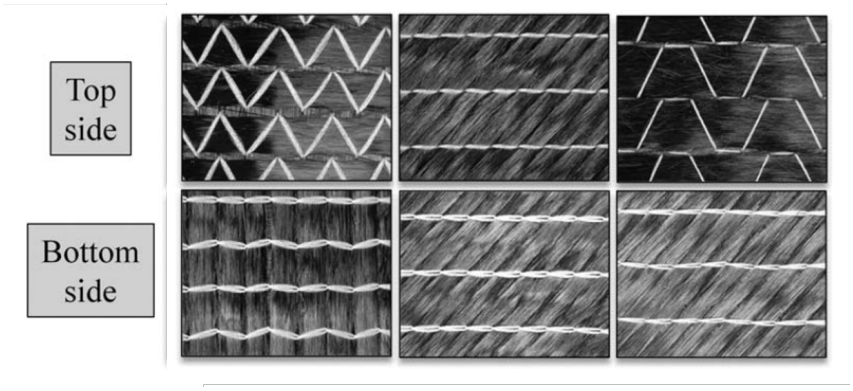

Fig. 2: Différents types de NCF [2]

Les défis concernent principalement les taux de production pouvant être atteints avec les processus de fabrication actuels pour les pièces composites. Pour obtenir la pièce composite finale, la formation du tissu est une étape clé de la fabrication au cours de laquelle des tissus plats en 2D sont transformés en une forme 3D et subissent de grandes déformations. Au cours de cette étape, le empilement fibreux est pressé dans un outil conçu pour la géométrie 3D souhaitée, après quoi de la résine est injectée dans le cadre des processus de moulage de composites liquides.

1.2 Projet AMECOMP

AMECOMP est un projet de recherche collaboratif international de Karlsruhe Institute of Technology (KIT) et de l'Institut national des sciences appliquées de Lyon (INSA Lyon), financé par la Fondation allemande pour la recherche (DFG) et l'Agence nationale de la recherche française (ANR). L'objectif central du projet est le développement de méthodes de simulation de mise en forme capables de décrire les mécanismes de déformation complexes des renforts NCF. Ces renforts sont utilisés pour la fabrication de pièces composites dans les industries automobile et aéronautique. L'objectif de ma thèse est de réaliser des modélisations mésoscopiques et M. Bastian Schäfer, docteur au KIT, se concentrera sur l'échelle macroscopique.

1.3 Comportement mécanique et simulation à multi-échelle

La simulation de la mise en forme du renfort permettrait l'optimisation numérique des moules et des renforts, évitant ainsi une phase coûteuse d'essais et d'erreurs lors de la conception de pièces composites. D'importants efforts de recherche sont consacrés au comportement du renfort sec et à la simulation de sa déformation. L'objectif est de prédire les caractéristiques géométriques et mécaniques qui peuvent apparaître lors de la mise en forme. Les renforts fibreux sont des matériaux hautement multi-échelles : les phénomènes que nous modélisons dépendent de l'échelle à laquelle le renfort est observé. On distingue l'échelle microscopique des filaments, l'échelle mésoscopique de la mèche, et l'échelle macroscopique ou structurale du textile dans son ensemble. Pour chaque échelle, un matériau représentatif équivalent est défini en utilisant des modèles de milieu continu

dans lesquels les phénomènes hérités des échelles inférieures ne sont pas explicitement représentés, mais intégrés dans la loi constitutive.

Échelle à microscopique L'échelle microscopique permet l'étude de la microstructure du matériau (voir Figure 3) et, par conséquent, la simulation de mécanismes localisés tels que la déformation d'une fibre ou leurs interactions à une échelle suffisamment fine. C'est l'échelle la plus précise. Cependant, le coût de cette précision se mesure en temps de calcul en raison du grand nombre de corps constituant le modèle, en particulier le contact entre ces corps.

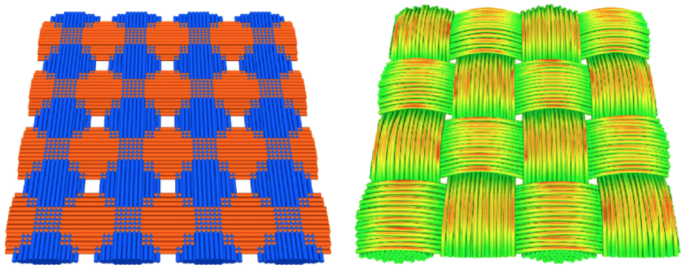

(a) Initial state (a) Woven state

Fig. 3: Modélisation du VER d'un renfort après tissage [3]

Échelle à mesoscopique Les modèles à l'échelle mésoscopique se concentrent généralement sur le comportement d'une unité élémentaire du renfort, en considérant la mèche comme un milieu continu (voir Figure 4). La simulation est basée sur une compréhension du comportement des mèches. Cette approche permet de déduire un comportement plus global à l'échelle macroscopique ainsi que la perméabilité locale du renfort en fonction de la déformation de l'unité élémentaire.

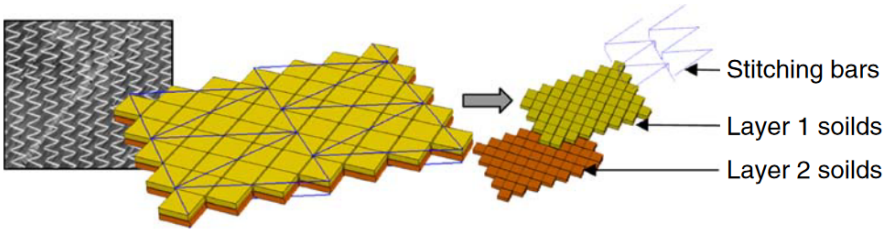

Fig. 4: Modèle mésoscopique de NCF biaxial développé par G. Creech [4]

Échelle à macroscopique À cette échelle, des essais mécaniques sont réalisés sur des échantillons de grande taille contenant plusieurs volumes elementaires représentatives (VER). La simulation à l'échelle macroscopique vise à simuler la mise en forme du renfort textile à l'échelle de la pièce entière (voir Figure 5).

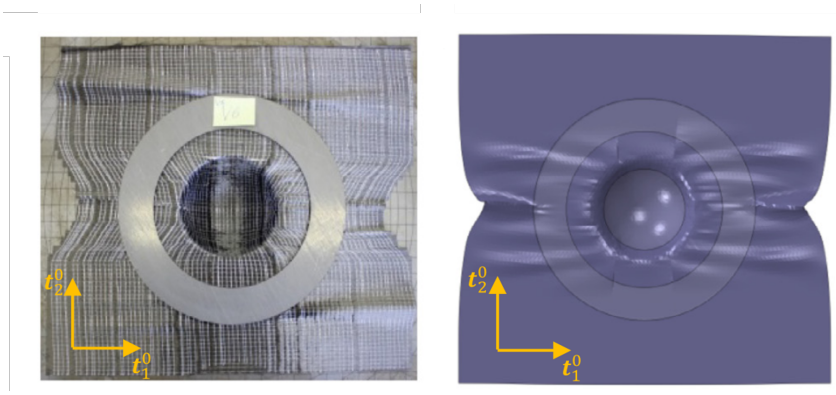

Fig. 5: Modèle macroscopique de UD NCF par F. Schirmaier [5], comparaison des résultats expérimentaux et des résultats de simulation

Chapitre 2 Modélisation mésoscopique du biaxial NCF à partir d'observations expérimentales

2.1 Stratégie de modélisation

Afin de développer un modèle d'éléments finis (EF) mésoscopique approprié, deux aspects principaux doivent être pris en compte : la création d'un modèle géométrique précis et l'obtention de données matérielles appropriées pour le modèle constitutif.

La tomographie par rayons X a été utilisée pour mesurer les paramètres géométriques des mèches de chaîne et de trame, tandis que les coutures environnants ont été décrits de manière explicite à partir du motif de tricot. La loi constitutive hyperélastique est appliquée à la mèche de fibres, avec un élément de poutre incorporé pour découpler la rigidité à la flexion, et des éléments de poutre de section générale sont définis pour les coutures. Des essais expérimentaux appropriés sur des mèches individuelles et des coutures à l'échelle mésoscopique sont conçus et réalisés pour obtenir des données matérielles d'entrée. Dans ces essais, la mèche individuelle et la couture sont isolées des renforts bi-axiaux NCF en coupant les connexions de boucle de la couture. Une étape de précontrainte est introduite pour prendre en compte l'interaction entre la mèche et la couture.

2.2 Matériau étudié

Le matériau utilisé dans cette étude est un biaxial non-crimp-fabric qui est produit par Zoltek, un fabricant allemand, à partir d'une mèche en fibre de carbone continu dit PX35. Il contient deux couches avec une orientation $0°/90°$ avec une densité surfacique de 608 g/m2. La couture est un matériau Poly-Ester.

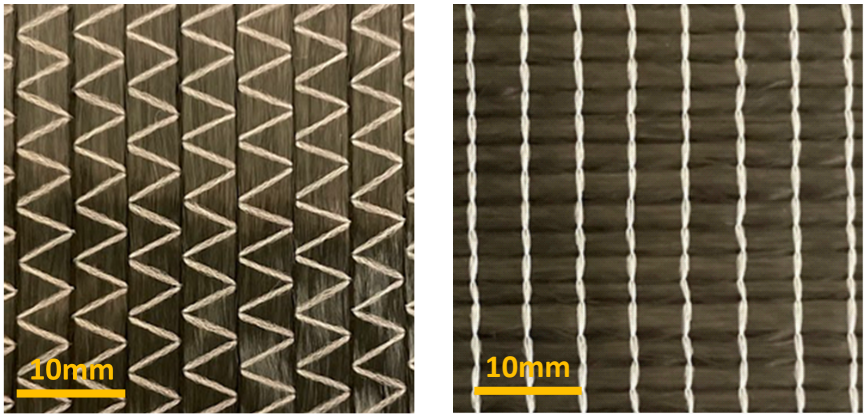

Fig. 6: Presentation of studied bi-axial NCF

2.3 Modèle géométrique de NCF

Les modèles géométriques jouent un rôle vital dans les études numériques. Dans cette thèse, un modèle géométrique 3D de NCF biaxial qui consiste en la modélisation des mèches chaîne et trame et de la couture a été établi à partir du résultat de la tomographie (voir Figure 7). Dans cette structure, la mèche doit être droite comme état initial idéal. La section transversale est considérée comme une forme elliptique. La largeur de la mèche trame définie par la couture du motif tricot est presque deux fois supérieure à celle de la mèche chaîne définie par la couture du motif chaîne après l'observation.

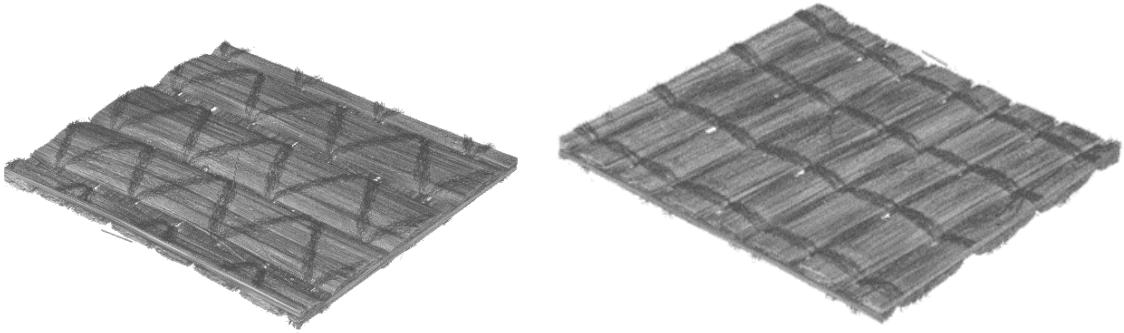

(a) (b)

Fig. 7: Vue tomographique 3D d'un échantillon NCF bi-axial

A l'aide du logiciel ImageJ, nous pouvons mesurer avec précision tous les paramètres géométriques détaillés, y compris l'épaisseur de la mèche et l'écart entre les mèches, à partir du résultat de la tomographie. Tous les résultats sont présentés ici.

L'équation elliptique est utilisée pour générer le modèle de la mèche :

$$\left(\frac{X}{\frac{w_c}{2}}\right)^2 + \left(\frac{Z}{\frac{h}{2}}\right)^2 = 1, \tag{1}$$

Avec w_c est la largeur de la mèche et h est la hauteur de la mèche. Le nombre d'éléments

dépend de la taille du maillage.

La géométrie de la couture est décrite en fonction de son motif de tricot. Le diamètre de la couture est considéré comme constant. On suppose que la couture traverse les deux plis en ligne droite. Pour un exemple de la couture unitaire , la couture s'enroule autour de la mèche par le haut, puis à travers deux couches de la mèche, et enfin fait le tour par le bas et fait le tour de la couture précédente. Si nous avons déjà la géométrie de la mèche et supposons que la couture est étroitement liée à la mèche, nous pouvons utiliser les équations pour tracer tous les nœuds et générer l'image de la couture. Tous les nœuds sont générés à l'aide d'équations dans Matlab avant d'être transférés au format de fichier ABAQUS (.inp).

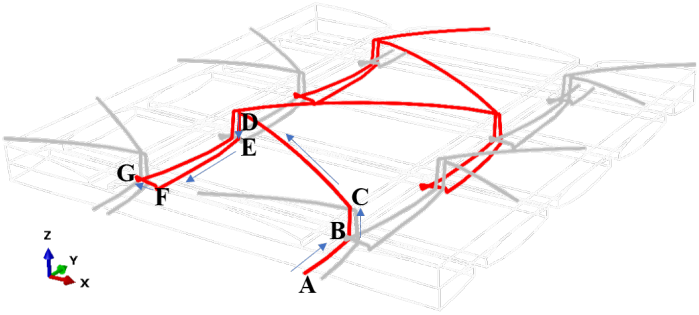

Fig. 8: Modèle géométrique de la couture avec une boucle entière de point en rouge

2.4 Modélisation éléments finis de la mèche

Pour les mèches de NCF, la loi hyperélastique qui a été proposée par Charmetant est utilisée. Le développement de la loi hyperélastique se base sur des invariants de la transformation. La fonction densité d'énergie de déformation peut s'écrire en fonction d'invariants de la transformation :

$$w = w(I_1, I_2, I_3, I_4, I_5) \tag{2}$$

I_1, I_2, I_3 sont les invariants standards du tenseur de déformation de Cauchy-Green $\underline{\underline{C}}$, I_4 et I_5 sont les invariants mixtes définis à partir du tenseur de structure $\underline{\underline{M}}$ qui est défini par la direction d'orientation des fibres $\underline{M}$.

$$I_1 = trace(\underline{\underline{C}}) \tag{3}$$

$$I_2 = \frac{1}{2}(trace(\underline{\underline{C}})^2 - trace(\underline{\underline{C}}^2)) \tag{4}$$

$$I_3 = det(\underline{\underline{C}}) \tag{5}$$

$$I_4 = \underline{\underline{C}} : \underline{\underline{M}} \tag{6}$$

$$I_5 = \underline{\underline{C}}^2 : \underline{\underline{M}} \tag{7}$$

La mèche qui est supposée isotrope transverse est considérée comme ayant quatre modes de déformation (voir Figure 9) : l'élongation dans la direction des fibres (a), la compaction dans le plan transverse (b), la distorsion dans le plan transverse (c) et le cisaillement transverse (d). L'énergie de déformation est décomposée en quatre fonctions énergie de

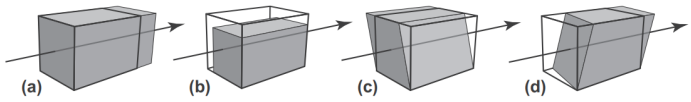

Fig. 9: Modes de déformation de la mèche

déformation associées à chaque mode de déformation.

$$\begin{aligned} w =& w_{\text{elong}}(I_{\text{elong}}) + w_{\text{comp}}(I_{\text{comp}}) \\ &+ w_{\text{dist}}(I_{\text{dist}}) + w_{\text{sh}}(I_{\text{sh}}) \end{aligned} \tag{8}$$

Les invariants physiques (élongation, compaction, distorsion, cisaillement) sont calculés à l'aide des invariants standards, I_1, I_2, I_3, I_4 et I_5 comme suit:

$$I_{elong} = \frac{1}{2}\ln I_4 \tag{9}$$

$$I_{comp} = \frac{1}{4}\ln\left(\frac{I_3}{I_4}\right) \tag{10}$$

$$I_{sh} = \sqrt{\frac{I_5}{I_4^2} - 1} \tag{11}$$

$$I_{dist} = \frac{1}{2}\ln\left(\frac{I_1 I_4 - I_5}{2\sqrt{I_3 I_4}} + \sqrt{\left(\frac{I_1 I_4 - I_5}{2\sqrt{I_3 I_4}}\right)^2 - 1}\right) \tag{12}$$

Le second tenseur de Piola-Kirchhoff $\underline{\underline{S}}$ est calculé selon la formule standard:

$$\begin{aligned} \underline{\underline{S}} &= 2\frac{\partial w}{\partial \underline{\underline{C}}} \\ &= 2\left(\frac{\partial w_{elong}}{\partial I_{elong}}\frac{\partial I_{elong}}{\partial \underline{\underline{C}}} + \frac{\partial w_{comp}}{\partial I_{comp}}\frac{\partial I_{comp}}{\partial \underline{\underline{C}}}\right. \\ &\quad \left. + \frac{\partial w_{dist}}{\partial I_{dist}}\frac{\partial I_{dist}}{\partial \underline{\underline{C}}} + \frac{\partial w_{sh}}{\partial I_{sh}}\frac{\partial I_{sh}}{\partial \underline{\underline{C}}}\right), \end{aligned} \tag{13}$$

De plus, nous proposons d'incorporer éléments poutres au sein des mèches pour découpler la rigidité à la flexion du matériau. Ces éléments poutres sont situés au centre de chaque mèche et partagent les mêmes nœuds que les mèches. Le partage des nœuds élimine la nécessité de considérer le contact entre les éléments poutres et solides. Étant donné que l'on suppose que les mèches sont inextensibles, le comportement en traction des éléments poutres peut être négligé, car il n'affecte pas le mécanisme de déformation global. Ainsi, la rigidité à la flexion de ces éléments poutres est déterminée exclusivement par leur module de Young et leur moment d'inertie.

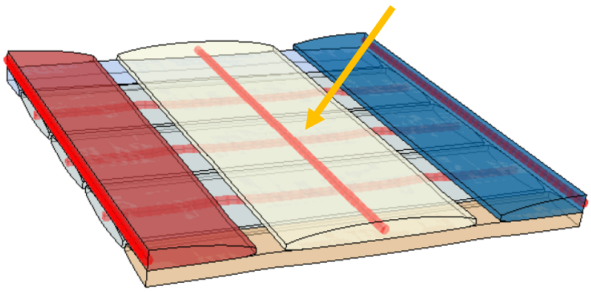

Fig. 10: Elément de poutre incorporés pour renfort

Afin de caractériser le comportement d'une mèche, la couture tricotée est coupée à la main pour extraire une seule mèche du NCF. Le comportement en allongement est souvent directement identifié à partir d'un essai de traction d'une seule mèche. Le comportement de compaction et de déformation du matériau est caractérisé à l'aide d'essais de compression. En ce qui concerne le cisaillement longitudinal, un test de traction uniaxial a été réalisé dans l'étude de Charmetant sur le tissu tissé. Lors de ce test, l'allongement et la déformation de cisaillement longitudinal se produisent. Ensuite, le paramètre de cisaillement longitudinal peut être identifié par une approche inverse après avoir connu le comportement à l'allongement. Cependant, pour le matériau NCF biaxial, étant donné qu'il n'a pas d'embuvage, aucune déformation de cisaillement longitudinal ne se produit dans ce test. Un nouveau test de cisaillement est introduit. Un test de flexion a également été réalisé pour caractériser la rigidité de flexion hors du plan.

2.5 Modélisation éléments finis du fil de couture

Le modèle aux éléments finis de la couture est représenté par des éléments de poutre à section générale afin de spécifier un moment d'inertie défini par l'utilisateur. La rigidité à la flexion est calculée directement à partir de ce moment d'inertie comme suit :

$$G_s = E_s \cdot I \tag{14}$$

Un test de traction simple de la couture a été réalisé pour déterminer son module d'élasticité en traction E_s, tandis qu'un test de cantilever a été effectué pour déterminer sa rigidité à la flexion G_s.

Le défi le plus complexe dans la modélisation des renforts composites de NCF réside dans l'interaction entre la couture et la mèche. Les glissements entre les deux plis des mèches et la couture sont plus importants par rapport à ceux dans le tissu tissé. Une étape de précontrainte thermoélastique est introduite pour simuler ce processus avant l'étude numérique au lieu de mettre en œuvre une loi de frottement spéciale. Avec la baisse de la température, la couture rétrécit naturellement afin de simuler l'état de tension de la couture et l'état de compaction de la mèche.

Sa déformation thermique ϵ_x^{th} est donnée par le coefficient de dilatation thermique

défini par l'utilisateur α et le changement de température Δt comme suit :

$$\epsilon_x^{th} = \alpha \cdot \Delta t \tag{15}$$

Puisque la déformation de la couture est ensuite limitée par les mèches de chaîne et de trame, la tension de couture donnée σ_x peut être exprimée comme suit :

$$\sigma_x = E_s \cdot (\epsilon_x - \epsilon_x^{th}) \tag{16}$$

Où E est le module de Young et ϵ_x est la déformation de la couture. Il faut trouver une bonne valeur pour la déformation thermique de la couture. Si la couture est trop serrée, la mèche sera déformée; si elle est trop lâche, il y aura encore beaucoup de glissement. Une approche empirique est utilisée ici pour déterminer une déformation thermique realiste de la couture.

L'ensemble du processus de modélisation mésoscopique par éléments finis est résumé sur la Figure 11.

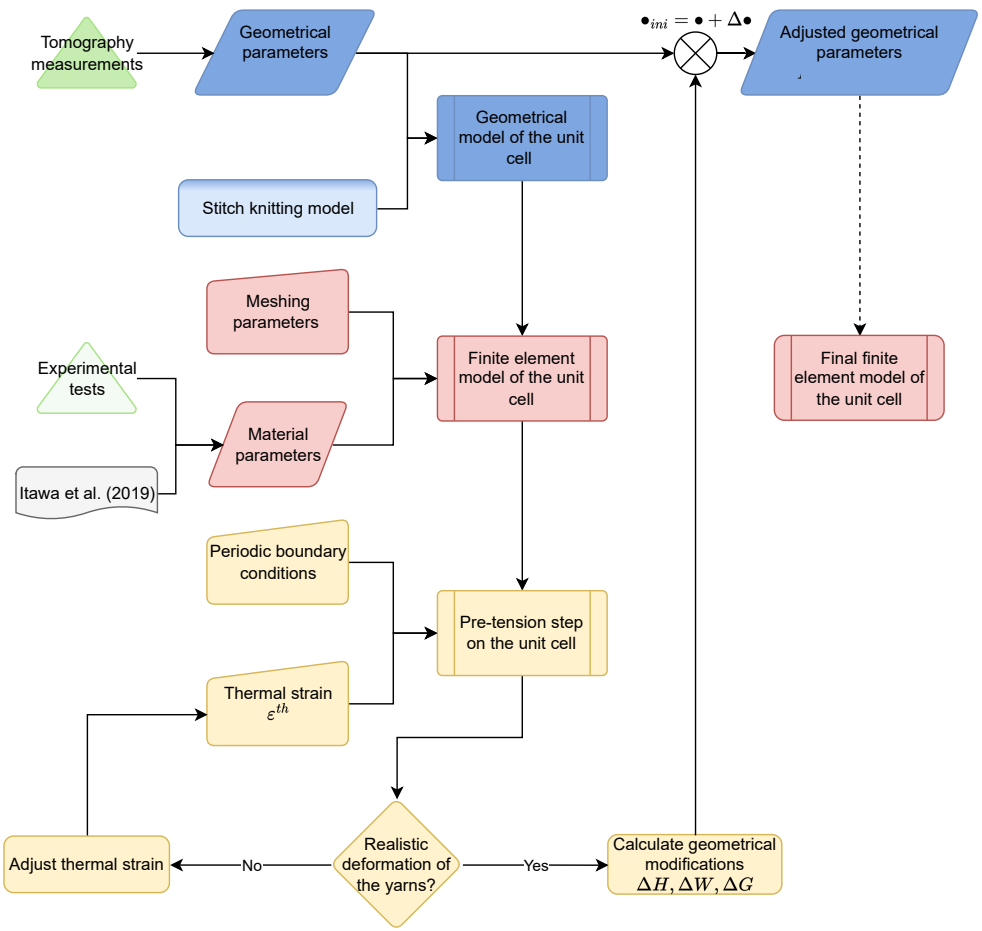

Fig. 11: Le diagramme de flux représentant l'ensemble du processus de modélisation mésoscopique

Le modèle d'assemblage final est présenté (voir Figure 12).

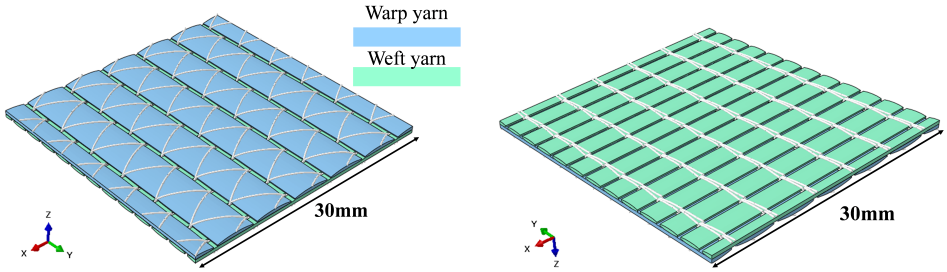

Fig. 12: Le modèle d'assemblage final

Chapitre 3 Validation du modèle mésoscopique

3.1 Essais expérimentaux

Des tests expérimentaux de cisaillement en plan sont utilisés pour valider le modèle mésoscopique du NCF. La déformation de cisaillement en plan se produit lorsque les fils de chaîne et de trame pivotent pour former un angle de cisaillement γ. Deux tests expérimentaux sont principalement utilisés par les chercheurs pour analyser le comportement de cisaillement dans le plan : le Picture frame test et le Biax-extension test (voir Figure 13). Le Picture frame test est une méthode relativement simple. Le NCF échantillon est encastré dans un cadre articulé constitué de quatre barres rigides de même longueur de telle sorte que les fibres sont parallèles aux bords du cadre. L'échantillon est découpé en forme de croix dont le centre est la zone utile. Pour le bias-extension test, des échantillons de NCF ont été serrés à chaque extrémité et étendus axialement. Après deformation, il existe une zone de cisaillement pur au milieu de l'échantillon où l'angle de cisaillement est deux fois supérieur à la zone de demi-cisaillement.

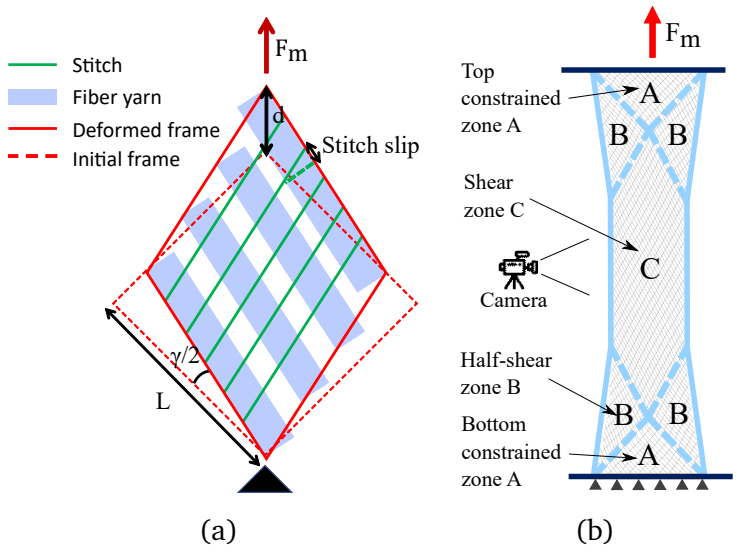

(a) (b)

Fig. 13: (a) Picture Frame Test (b) Bias Extension Test

3.2 Simulation numérique sur cellule unitaire

La simulation commence par un modèle de cellule unitaire, ce qui est une approche recommandée en raison de l'effort de calcul réduit impliqué. Les conditions aux limites et les périodicités sont définies. Un déplacement macroscopique est appliqué aux deux coins du modèle dans une direction qui forme un angle de 45 degrés par rapport à l'orientation des fibres. Le schéma et l'équation cinématique utilisés dans le Picture frame test peuvent être appliqués à l'analyse de la déformation en cisaillement pur dans cette cellule unitaire en considérant que la longueur du cadre est équivalente à la longueur du tissu. Les formes déformées sont représentées sur la Figure 14. La force de cisaillement sur le modèle de la cellule unitaire est également normalisée, puis elle est utilisée pour la comparer avec la force de cisaillement expérimentale.

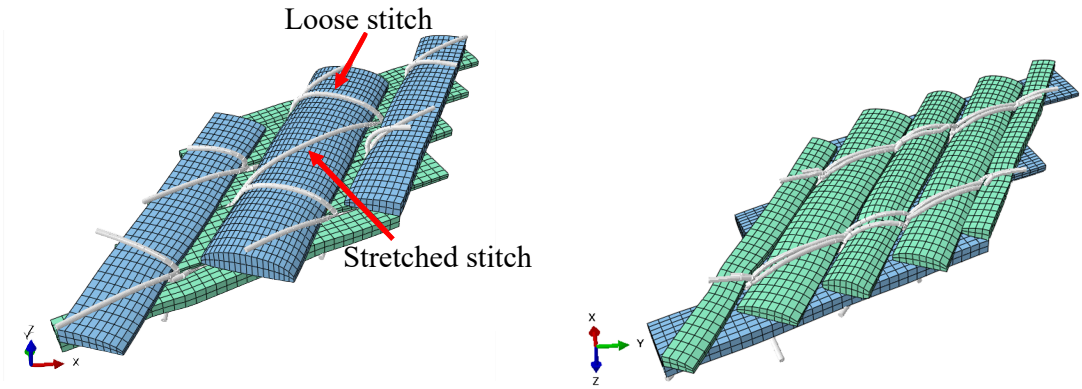

(a) (b)

Fig. 14: Configuration déformée d'une cellule unitaire sous test de cisaillement pur.

3.2 Simulation numérique sur BET

En raison de l'imposition de contraintes strictes, le modèle de cellule unitaire ressemble davantage à un Picture frame test. Des conditions de déplacement sont appliquées à l'intersection des fils de chaîne et de trame (position de deux demi-fils). L'angle de cisaillement réel correspond systématiquement à l'angle théorique calculé à l'aide des équations cinématiques. Pour observer le glissement entre les fils de chaîne et de trame, une simulation du BET est nécessaire. De plus, les performances du modèle doivent être illustrées à plus grande échelle.

Trois zones différentes peuvent être observées dans les résultats du BET (voir Figure 15), ce qui est en bon accord avec les résultats expérimentaux. Au bord de la demi-zone de cisaillement, un glissement inter-plis peut être observé, et une vue agrandie de la zone de cisaillement centrale permet d'observer le fil de couture tendu et le fil de couture comprimé.

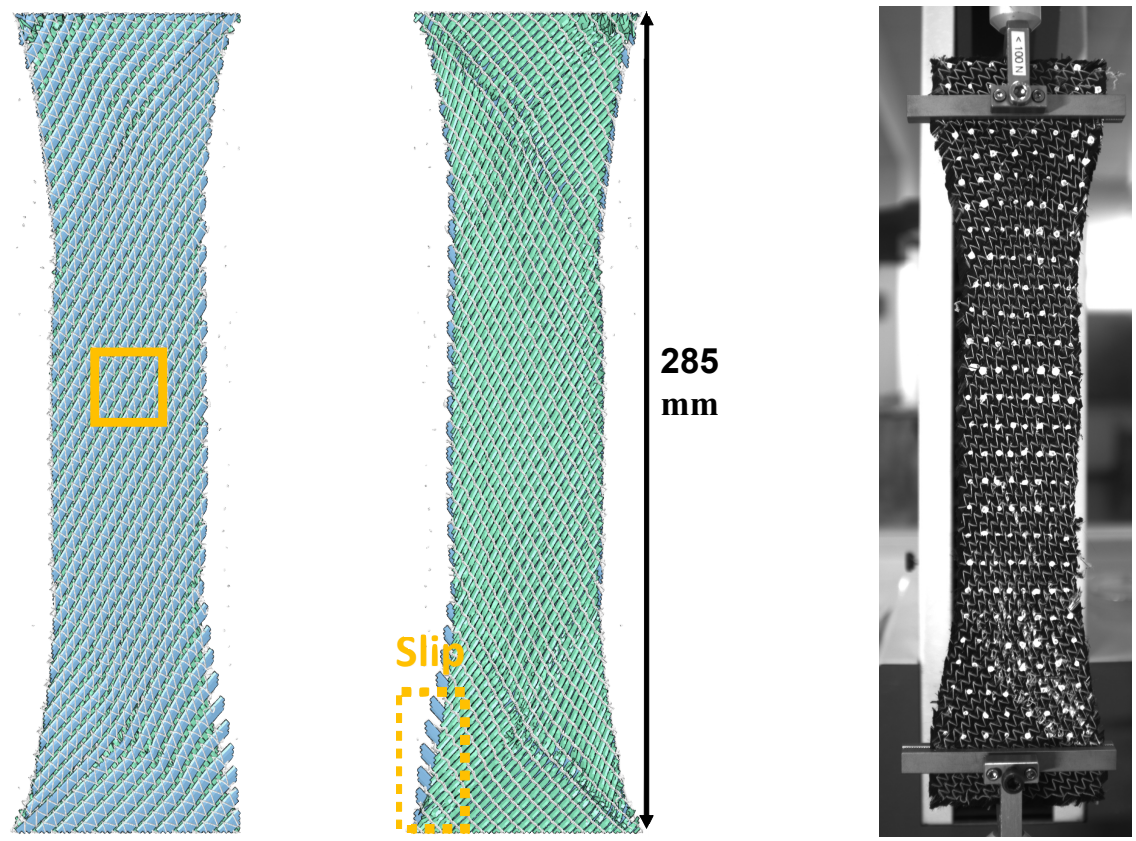

(a) (b) (c)

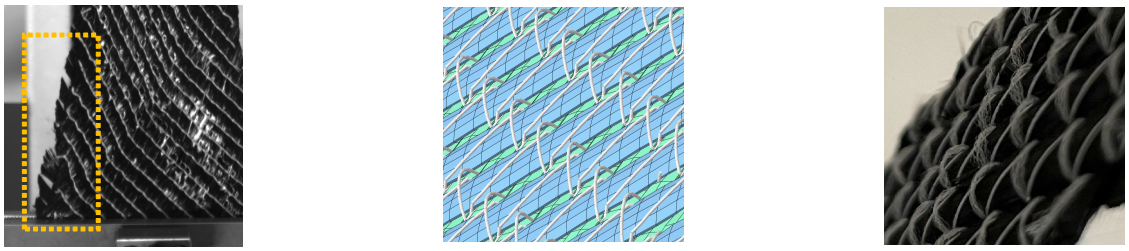

(d) (e) (f)

Fig. 15: Résultats du BET

3.3 Résultats et discussion

Deux aspects sont examinés pour comparer les résultats expérimentaux et la simulation numérique : la validation géométrique et la validation mécanique. La validation géométrique démontre la capacité de ce modèle à détecter les défauts locaux, tandis que la validation mécanique montre le potentiel de ce modèle pour effectuer une caractérisation virtuelle des matériaux. L'excellente concordance entre les forces de cisaillement obtenues à partir des tests expérimentaux et de la simulation numérique valide le potentiel de ce modèle pour les essais de matériaux virtuels.

Chapitre 4 Analyse numérique et expérimentale de la mise en forme des NCFs

4.1 Expérimentale de la mise en forme

Des tests expérimentaux de la mise en forme sur les NCFs ont été réalisés en collaboration entre l'INSA-LaMCoS et le KIT-FAST dans le cadre du projet AMECOMP afin d'étudier leur comportement lors de la mise en forme. Différentes formes de poinçons académiques (hémisphère, tétraèdre, boîte carrée), types de tissus (NCF unidirectionnel, NCF biaxial) et orientations des fibres (0°, 45°, double couche 0°/45°) ont été analysés. La déformation du renfort au cours de la mise en forme est mesurée par corrélation d'images numeriques, en suivante une grille de points blancs qppliquée préablement sur les mèches de carbonne. Une analyse complète est réalisée en se basant sur les forces de poinçonnage nécessaires, le contour extérieur, les déformations macroscopiques et les défauts de mise en forme observés. Dans les tests en une seule couche en particulier, des gapings se forment en raison d'une forte tension dans la direction des coutures ou d'une forte flexion dans le plan des mèches, car il n'est pas possible d'avoir du cisaillement perpendiculaire à la direction des fibres. Moins de défauts ont été observés dans les tests en double couche en raison de l'interaction entre la rigidité élevée des couches individuelles superposées.

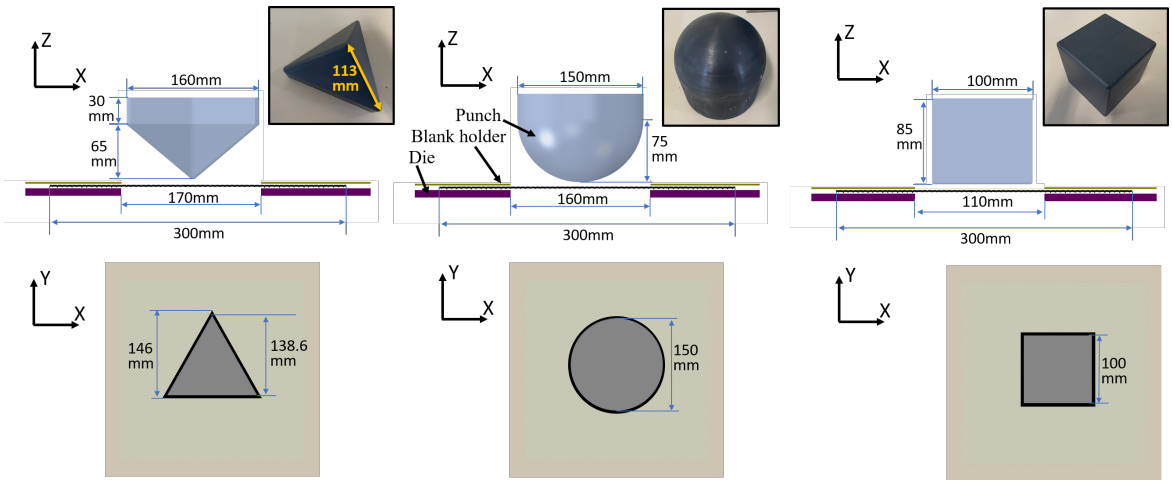

Fig. 16: Expérimentale de la mise en forme

4.2 Résultats de simulation numérique

Les tests de la mise en forme sont simulés numériquement à l'aide d'ABAQUS/Explicit. Le modèle mésoscopique de NCF biaxial présenté dans le chapitre précédent est utilisé. En raison de la symétrie du NCF biaxial, les poinçons hémisphériques et carrés symétriques sont modélisés à l'aide d'un échantillon d'un quart de taille ($150\,\mathrm{mm} \times 150\,\mathrm{mm}$), tandis que la forme tétraédrique axiale est modélisée à l'aide d'un échantillon de moitié de taille ($150\,\mathrm{mm} \times 300\,\mathrm{mm}$) pour minimiser les coûts de calcul. Le modèle de quart de taille comprend 57 840 éléments solides pour deux plis de mèche, 10 858 éléments et

58 441 éléments de poutre pour les coutures. Le modèle de moitié de taille contient le double du nombre d'éléments. Les modèles pour le poinçon, la matrice et le serre-flanc pour différentes formes sur les mêmes dimensions que ceux utilisés dans les tests expérimentaux. Les résultats sont présenté dans le Figure 17.

4.3 Observation des défauts

Les défauts peuvent survenir lors du processus de mise en forme en raison des variations de géométrie de la pièce, du type de renforcement et de la configuration expérimentale. La détection de la présence de défauts est un objectif principal de la réalisation de ces tests de la mise en forme et de simulations. L'occurrence des défauts du gaping est discutée. Il est constaté que les formes de tétraèdre et de boîte carrée posent plus de défis, en particulier au niveau des coins où des fentes peuvent être observées après la mise en forme. Le glissement entre les plis peut également être observé, ce qui constitue un avantage de la modélisation à l'échelle mésoscopique.

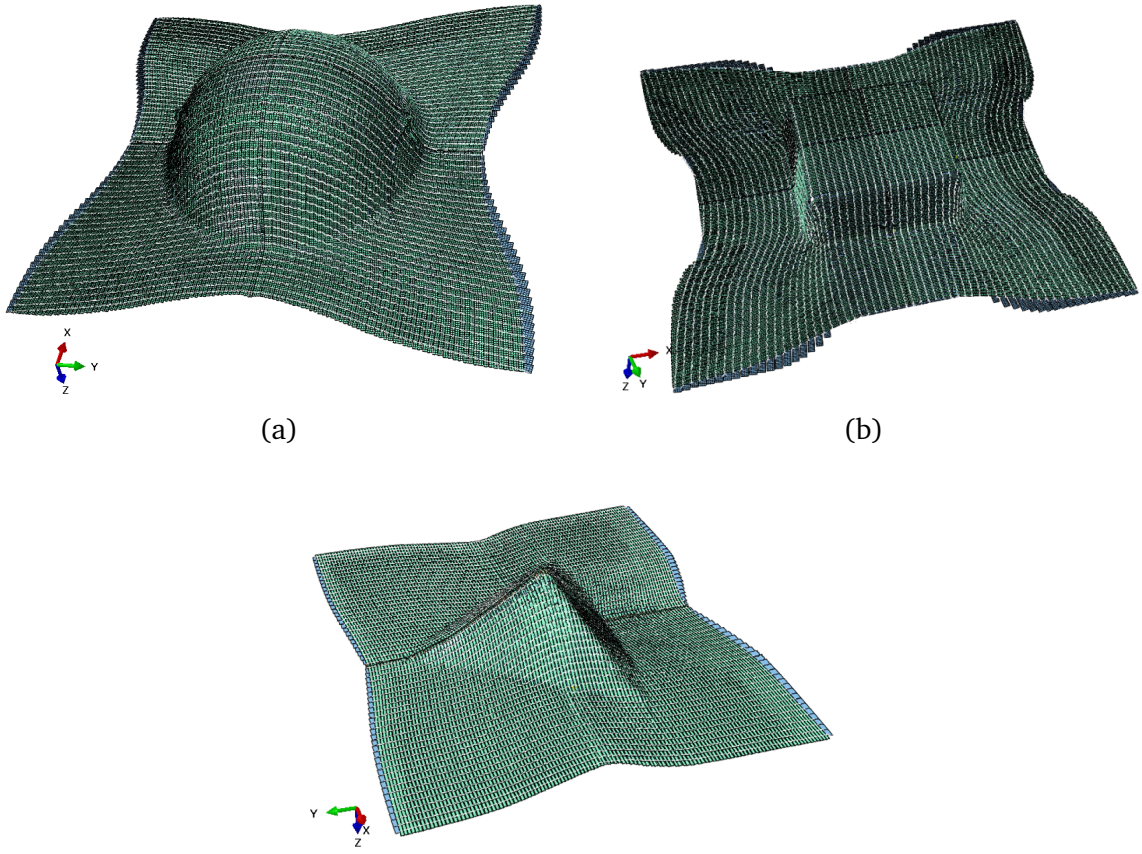

(a) (b)

(c)

Fig. 17: Vue 3D de la simulation de la mise en forme

CHAPTER 1

Introduction to the composite material and simulation approach

This chapter provides an overview of composite materials, their significance, and the need for a comprehensive understanding of their mechanical behavior. It begins by introducing the composite materials and their exceptional mechanical properties, such as high strength-to-weight ratios. Among them, non-crimp-fabric composite reinforcements are one of the most promising types of reinforcements for the manufacturing of composite parts in both the automotive and aeronautical industries. Their manufacturing process is introduced. Furthermore, this chapter elucidates the complexity of studying the mechanical behavior of NCF composites, characterized by various deformation modes like tension, compression, shear, and bending, necessitating a multi-scale approach to comprehend their performance comprehensively. In this context, the chapter introduces the simulation approaches employed in the literature at different scales to model and predict the mechanical behavior of fibrous reinforcements.

Contents

1.1 Introduction to the composite material

1.1.1 Composite material

Composite materials have gained significant attention from both industry and the scientific community due to their unique properties. Generally, a composite material is formed by combining two or more components to create a superior material with enhanced performance. This broad definition encompasses a wide variety of materials, including both natural substances that have been utilized for an extended period, such as wood, bones, or wattle and daub, as well as modern innovations like tires or reinforced concrete. The defining characteristic of all these materials is that they consist of two primary phases: the reinforcement phase, responsible for controlling the mechanical properties of the final product, and the matrix phase, which ensures the cohesion of the entire structure, incorporating fibers or particles.

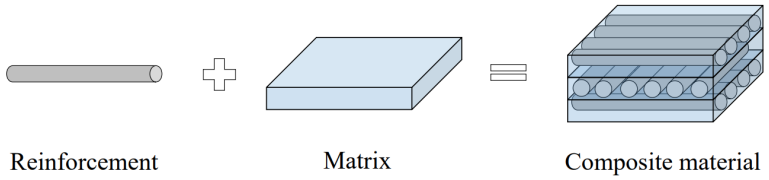

Fig. 1.1: Composition of composite materials [1]

Humans have been using composite materials for a long time. Ancient Chinese adobe bricks, for instance, were composed of two materials, rice straw and clay. Rice straw reinforced the clay, resulting in strong and durable buildings made from these materials. In modern times, with the invention of fiberglass (1893), fiber-reinforced organic matrix composites were gradually employed in various industries. Glass fiber composite reinforcement played a major role in reducing the weight of aircraft and ships. In the 1950s, glass fiber composite reinforcement began to be used in construction, transportation machinery, electrical and electronic products, as well as in sports products. Since the 1960s, with the advent of high-strength, high-modulus carbon fiber, the use of carbon fiber has led to even more high-performance composites, making it more suitable for applications in aerospace, transportation machinery, wind turbine blades, military equipment, and medical devices.

Matrix materials used in modern composite materials are typically classified into two main categories:

- Organic Matrices: These matrices are available in the form of thermoplastic, thermosetting, or elastomeric resins. They are widely used in various industries, includ-

ing both consumer and high-tech products. Their primary advantages are low cost and ease of manufacturing processes.

- Mineral Matrices: Mineral matrices consist of ceramics, metals, or graphite. They are specifically employed in advanced sectors such as military and aerospace, as well as in environments with challenging conditions like high temperatures and adverse humidity, which are detrimental to organic matrices. However, the manufacturing process for mineral matrices is difficult and complex, leading to higher costs.

The choice of matrix material depends on the specific requirements of the application, including factors such as cost, environmental conditions, desired properties, and the intended use of the composite material. Organic matrices are more common in everyday products, while mineral matrices are reserved for specialized and high-performance applications where their unique properties are essential.

Reinforcements can generally be categorized into several categories based on their geometric structure. They can be made of discontinuous fibers, continuous fibers, or particulate fillers.

- Particulate reinforcements: In this category, the matrix is reinforced with a dispersed phase of particles, with or without a preferred orientation. These are typically granular (such as chalk), lamellar (like talc or mica), or acicular (e.g., wollastonite, short fibers). Composites with particulate reinforcements are less commonly used for structural purposes and are more often employed in specific applications or consumer products. This type of reinforcement is often used with metallic matrices.

- Short fiber reinforcements: The matrix is reinforced with dispersed short fibers, where the length of the fibers is less than a hundred times their diameter, with or without preferential orientation. Various types of fibers can be used, with glass fibers and carbon fibers being widely utilized. Steel fiber is also emerging as a new component that combines exceptional stiffness and ductility.

- Continuous fiber reinforcements: These are composed of an ordered assembly of continuous fibers, where the fiber length is of the same order of magnitude as the dimensions of the final part. The preferred directions of the continuous fibers determine the main mechanical characteristics of the final part, and the behavior of the matrix is of secondary importance in these directions. In this type of reinforcement, the matrix serves to provide cohesion to the whole and offer resistance to stresses applied in directions different from those of the fibers.

A composite material possesses superior properties that can meet specific needs that cannot be individually satisfied by the basic components. Among the major properties they offer, we can observe:

- Strength: Composite materials often exhibit higher strength compared to their individual components, making them suitable for applications requiring durability and load-bearing capabilities.

- Lightweight: Composites are known for their high strength-to-weight ratio, making them ideal for industries like aerospace and automotive, where weight reduction is crucial.
- Corrosion Resistance: Many composite materials are highly resistant to corrosion, which is particularly valuable in environments where exposure to moisture or chemicals is a concern.
- Tailored Properties: Composites can be engineered to have specific properties such as electrical conductivity, thermal insulation, or fire resistance, making them versatile for a wide range of applications.
- Design Flexibility: Composites can be molded into complex shapes and structures, offering designers greater freedom and flexibility in creating innovative products.
- Fatigue Resistance: Composites often have excellent fatigue resistance, making them suitable for components that experience repeated loading and unloading cycles.

In this thesis, we will focus our attention on continuous carbon fiber reinforcements.

1.1.2 Composite materials of Non-crimp fabric

The Non-crimp fabric (NCF) reinforcements consist of multiple layers of unidirectional plies bound together by stitches that pass through their thickness. Each ply is positioned at a specific angle relative to the machine's manufacturing direction, and the fiber yarns are straight without any undulations. This type of reinforcement offers a significant advantage in achieving mechanical stiffness greater than that of a fabric with the same thickness. The architecture of NCFs indicates that stitching plays a critical role in the deformation behavior of the reinforcement during forming. Various stitching types are available, with the most common being chain stitching, tricot, or a combination of both using alternating tricot-chain patterns, as depicted in Figure 1.2. The stitching is continuous and runs through the reinforcement in the direction of stitching. It creates a series of loops (illustrated schematically in Figure 1.3), which securely hold the fibers of the stack together. The characteristic stitching pattern is visible on the front side, while the back side shows a series of loops.

The continuous manufacturing process for NCF reinforcements is illustrated in Figure 1.4. Spools of "roving" feed the production line. The rovings are spread into fiber bands with the desired orientation by automated heads (Figure 1.4a). As the production line progresses, a stack of plies is constructed. The stack is finally stitched together by a row of needles with a predetermined spacing. The stitch length serves as an input parameter for the production line. The details of loop formation are illustrated in Figure 1.4b. The knit stitching is achieved by shifting a row of thread guide bars, located opposite the needles, with each stitch.

The orientation of unidirectional (UD) plies and the stitching parameters influence the organization of fibers within the reinforcement. Each stitching point causes the fibers

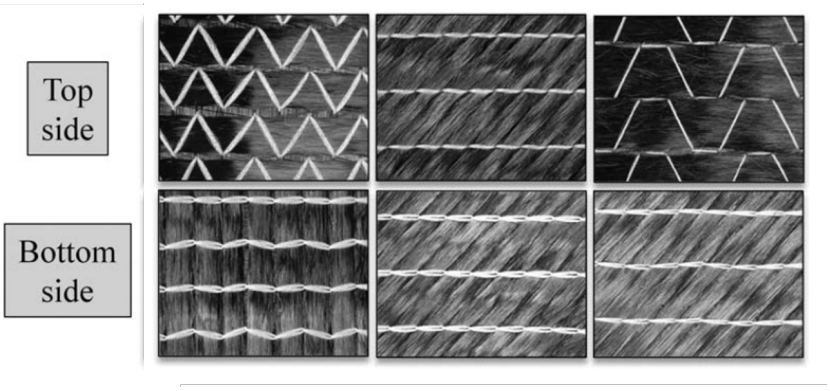

Fig. 1.2: Different types of NCF [2]

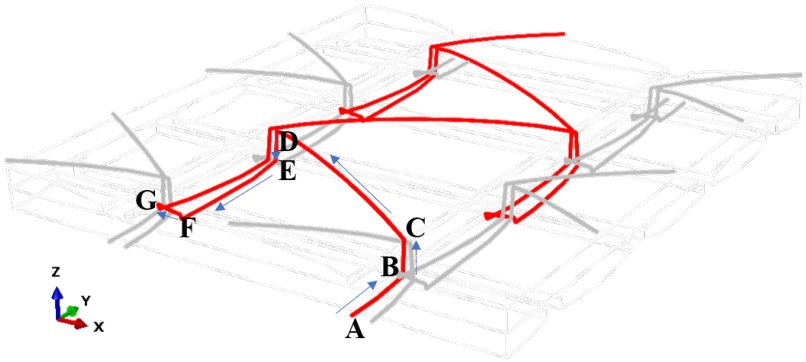

Fig. 1.3: Stitch structure

to be separated by the needles, resulting in gaps. When the grid formed by the stitching points aligns with the fibers, these gaps form channels. The fibers are then organized into bundles. This phenomenon is observed in specific architectures where the stitching grid points align with the fiber direction. The most common case is with biaxial NCF reinforcements where the fibers are oriented at 0°/90°. Previous research in the laboratory has focused on studying the 0°/90° configuration, which exhibits strong tendencies for ply sliding during forming [6].

1.1.3 Manufaturing process

The manufacturing processes for composite materials are numerous and diverse. Its goal is to shape flat 2D fabric plies into complex 3D shapes according to the geometry of the target component [8]. From primarily manual processes, the techniques have continually evolved to meet the increasing use of these materials. The need for higher production rates and parts with better-controlled and optimized characteristics has led to various types of processes being chosen based on requirements (shape, production rate, series, mechanical characteristics, etc.). Vacuum infusion and Resin Transfer Moulding (RTM) are the most commonly used. These are "closed mold" processes, meaning that the resin is not in direct contact with the ambient atmosphere. This allows for strict control of volatile

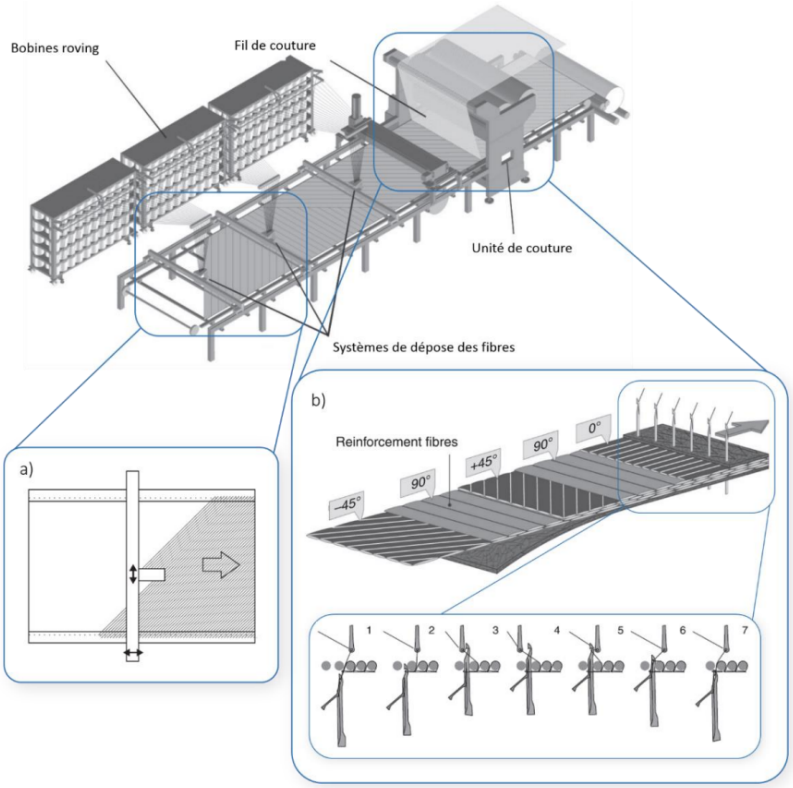

Fig. 1.4: Manufacturing process of NCF reinforcements [7]: a) details of the fiber deposition device b) details of the stitching step

organic compounds emitted during the manufacturing of parts.

Vacuum infusion

In the vacuum infusion process, the fibrous reinforcement is positioned directly on the surface of the mold (as shown in 1.5). By evacuating the air from this area, the vacuum pump presses the reinforcement against the mold using the membrane and the flow of resin. A drainage mesh, made of a porous material, is placed between the membrane and the reinforcement to facilitate the distribution of resin within the reinforcement. This process is less expensive and easier to implement compared to RTM. However, controlling the thickness and surface quality of both sides, especially the side against the membrane, is more challenging compared to the RTM process.

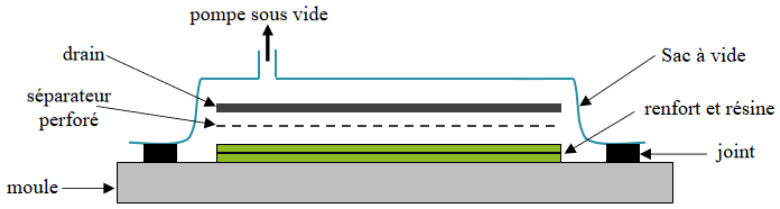

Fig. 1.5: Schematic diagram of the vacuum infusion process [9]

Resin transfer molding (RTM)

The Resin Transfer Molding process is widely used for the manufacturing composite part in medium to large quantities. It is characterized by the ability to produce a wide range of parts, from a few centimeters to several meters in size, while ensuring excellent reproducibility. It consists of three steps (see Figure 1-8):

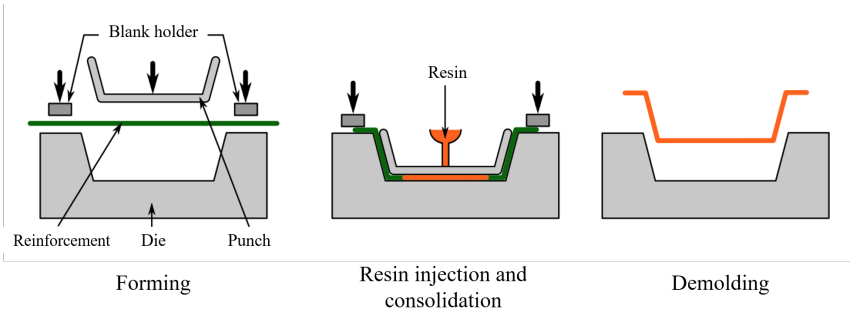

Fig. 1.6: Steps of RTM process [10]

- The first step, called preforming, follows the placement of the dry reinforcement on the mold which consists of a punch and a matrix. Its purpose is to press the reinforcement onto the final part's shape using an external force through the punch. Both parts of the mold are rigid, making it possible to control the thickness of the part and achieve a good surface finish on both sides, which is not the case for vacuum infusion. Blank holders are generally used during this step to tension the fabric and delay the appearance of wrinkles.
- Once the reinforcement is shaped into the desired form, the liquid resin is then injected at low pressure into this reinforcement. The pressure must be sufficient for the resin to flow throughout the entire space inside the mold cavity, but it should not be too high to avoid damaging the fibers. The matrix consolidation is then carried out by heating for a thermosetting matrix and by cooling for a thermoplastic matrix.
- When the resin has solidified, the part is finally demolded. The surface finish after demolding is controlled, resulting in a smooth appearance of the part.

The RTM process allows for the production of parts with complex geometries. The viscosity of the resin must be relatively low to completely infiltrate the preform. Pressure in the mold is not uniform during resin injection and reinforcement impregnation throughout the part. Controlling this pressure throughout the manufacturing process is challenging. The traditional RTM process is designed to operate at low pressure (less than 10 bar) and low flow rates (on the order of liters per minute). However, some variants have been developed to accelerate or facilitate injection in the case of poorly permeable reinforcements or highly viscous resins: vacuum assistance can be used (Vacuum Assisted RTM) or high-pressure injection (High Speed RTM). These variations make the RTM process adaptable to many types of reinforcements, and therefore to a wide range of achievable parts. Large-sized parts can be produced using this method.

In the RTM forming process, the different defects will appear depending on the forming parameters and the used material including mechanical defects (like wrinkles, buckling, fiber gap or overlap), the fluid defects (like resin void).

1.2 Project AMECOMP

This thesis is part of the work of AMECOMP which is an international collaborative research project involving the Karlsruhe Institute of Technology (KIT) and the National Institute of Applied Sciences of Lyon (INSA Lyon), funded by the German Research Foundation (DFG) and the French National Research Agency (ANR). It is a collaborative research project PRCI. It has been registered in phase 1 of the AAPG 2019. The central objective of the project is the development of forming simulation methods capable of describing the complex deformation mechanisms of NCF reinforcements.

Since forming defects such as gaping and wrinkles occur during the draping process and they need to be avoided as they are a major drawback for the final composite, accurate forming simulation approach should be developed to predict local effects and also inversely to design the forming process in such a way that an overall optimal fibre alignment is achieved and local defects are minimized. Mesoscopic modeling of UD-NCF and biaxial NCF will be developed to analyse the formation of gaping during forming and to conduct virtual material characterisation to parameterize the macroscopic approaches based on generalized continua. Macroscopic forming simulation methods for UD-NCF and biaxial NCF based on generalized continua approaches will be developed to correctly describe the influence of both the slip between the fibres and the bending stiffness of the fibres, in order to predict forming effects like fibre wrinkling and gaping. The material parameters will be identified through experimental tests. The project structure with responsibilities indicated by colours is shown in Figure 1.7.

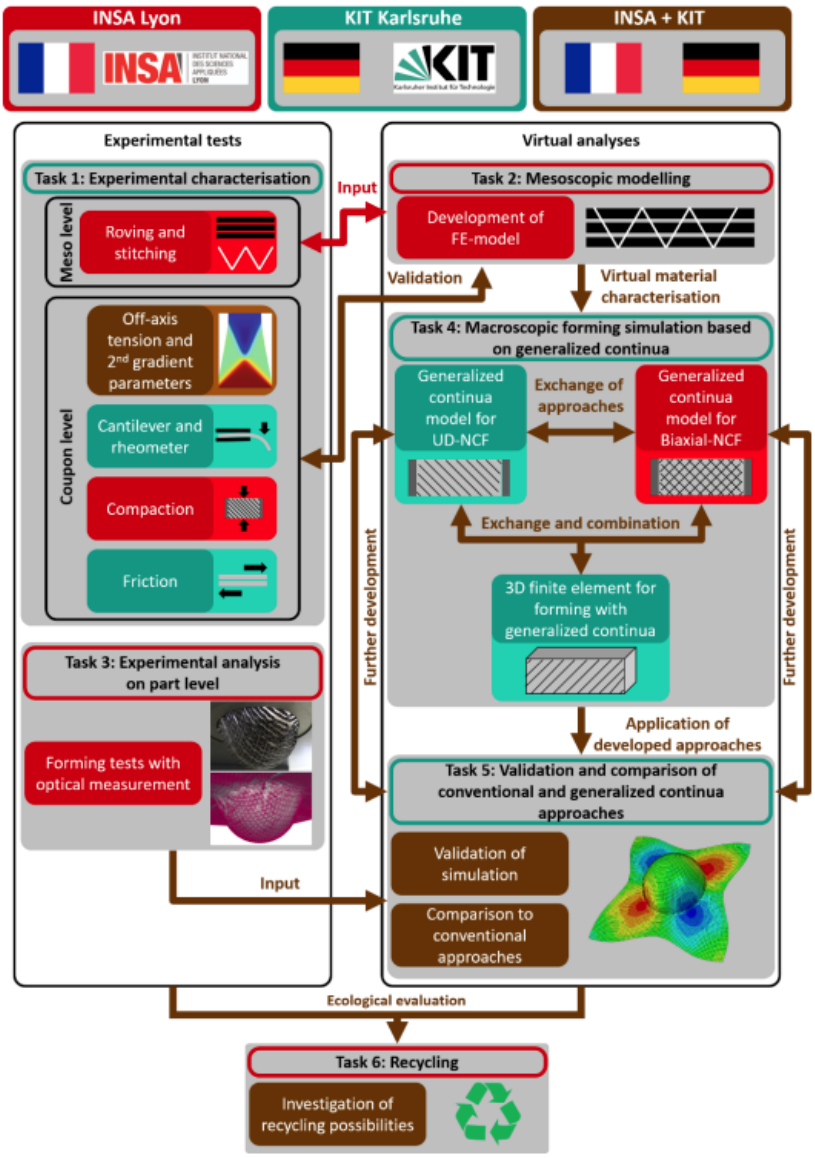

Fig. 1.7: Project structure with responsibilities indicated by colours

1.3 Mechanical behavior and simulation approach

Simulating the shaping of the reinforcement would allow for numerical optimization of molds and reinforcements, thus avoiding a costly trial-and-error phase during the design of composite parts. Significant research efforts are devoted to the behavior of dry reinforcement and the simulation of its deformation. The objective is to predict the geometric and mechanical characteristics that may appear during forming. Fibrous reinforcements are highly multi-scale materials: the phenomena we model depend on the scale at which the reinforcement is observed. A distinction is made between the microscopic scale of filaments, the mesoscopic scale of tows, and the macroscopic or structural textile scale as a whole. For each scale, an equivalent representative material is defined using continuous medium models in which the phenomena inherited from lower scales are not explicitly represented but integrated into the constitutive law.

1.3.1 Mechanical behavior and simulation approach at microscopic scale

The microscopic scale allows for the study of the material's microstructure and, as a result, simulating localized mechanisms like the deformation of a fiber or their interactions at a sufficiently fine scale. This is the most precise scale. However, the cost of this precision is measured in computation time due to the numerous bodies constituting the model, especially the contact between these bodies.

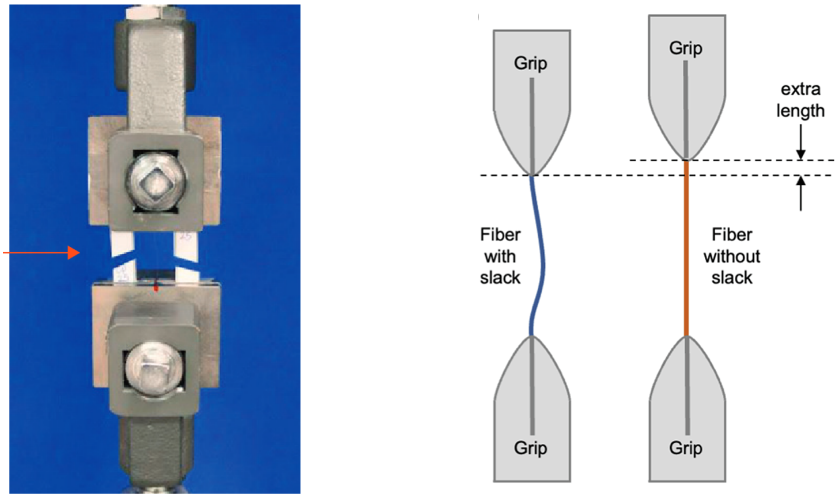

(a) (b)

Fig. 1.8: Tensile tests on single fiber yarn (a) specimen on ASTM C1557[11] (b) a schematic of gripped fiber with and without slack. [12]

In a microscopic-scale approach, the basic constituent is the fiber. Thus, it is important to understand all of the mechanical properties of single fibers [13]. However, the mechanical characterization of fibers is challenging due to their small size. To obtain the mechanical properties of fibers, a test conducted on a single fiber is usually performed [14]. Achieving precise measurements of deformation and initial diameter is a real challenge, as is holding a single fiber securely in the grips of the experimental setup. Two standard tests: ASTM C1557 "Standard Test Method for Tensile Strength and Young's Modulus of Fibers" [15], and ASTM D3822 "Standard Test Method for Tensile Properties of Single Textile Fibers" [16] are widely used in single fiber testing. The fiber is glued to paper or plastic, and the whole assembly is cut before testing (cf. Figure 1.8). All of these preparations are done to securely hold the fiber in the experimental setup and reduce stress concentrations at the fiber ends [15]. In ASTM D3822, a grip error length is added to the gauge length to account for grip effects on failure strain [16]. Non-contact strain measurements such as laser extensometers or digital image correlation (DIC) has also been demonstrated successful [17, 18], but these measurements are challenging, particularly because of the increased fiber manipulation required that may damage the sample.

Currently, several researches are focused on this scale. A weaving model was developed by Zhou [19] in order to predict the geometry of elementary woven meshes within certain

limits (cf. Figure 1.9). The work of Durville [3] has shown promising results for the microscopic-scale simulation of reinforcements. Models of elementary meshes have been developed to visualize the positioning of tows and their rearrangement during loading, as shown in Figure 1.10. The main limitation of this type of simulation is the computational time associated with the number of fibers to model. For this reason, groups of fibers are modeled within the tows, reducing the number of virtual fibers to a few dozen instead of the thousands of real fibers. The result is directly dependent on the discretization: the coarser the discretization, the closer the behavior of the fiber groups is to that of the tows, which is much more complex.

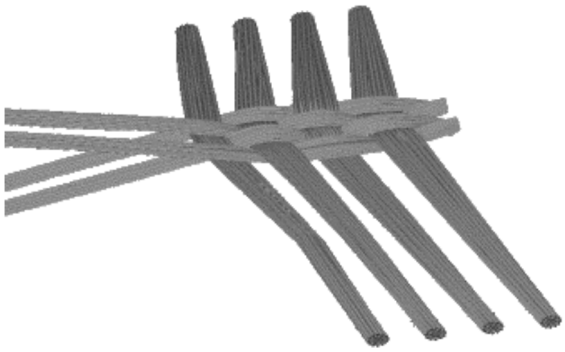

Fig. 1.9: 2D woven reinforcement generated by the Zhou model [19]

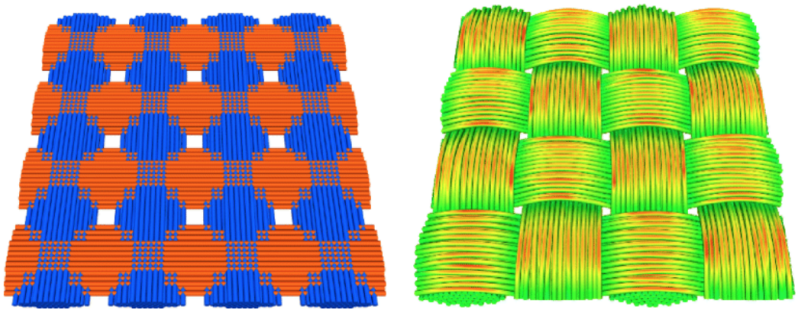

(a) Initial state (a) Woven state

Fig. 1.10: Modeling of the RVE of a reinforcement after weaving [3]

1.3.2 Mechanical behavior and simulation approach at mesoscopic scale

Mesoscale models usually focus on the behavior of an elementary unit of the reinforcement, considering the yarn as a continuous medium. The simulation is based on an understanding of the behavior of the tows. This approach allows for deriving a more global behavior at the macroscopic scale and also the local permeability of the reinforcement as a function of the deformation of the elementary unit.

One effective method, currently used to observe deformation mechanisms at this scale, is X-ray microtomography. This technique holds promise for a detailed understanding

of the internal movements within the tow [20, 21, 22, 23]. X-ray tomography is a non-destructive imaging technique that enables the reconstruction of cross-sectional or 3D images of solid objects. Its fundamental principle is based on the interaction of X-rays with matter, specifically the attenuation properties of X-rays as they pass through an object, akin to conventional radiography. The data collection process involves a meticulous examination of the sample under investigation, involving the acquisition of numerous radiographic images from various viewing angles. Subsequently, advanced mathematical algorithms are applied to these datasets to reconstruct the 3D geometry within the sample. The core concept of tomography revolves around the reconstruction of the sample's volume through a sequence of radiographs that represent cross-sectional slices along the sample, with these slices being perpendicular to the axis of rotation of the object. This methodology closely resembles medical scanning techniques, where radiographs are acquired while systematically altering the viewing angle of the object to capture a complete revolution's worth of data. From this set of radiographs, a high-resolution map of local absorption coefficients can be computationally reconstructed for every point within the sample. In contrast to medical scanning, wherein the patient remains stationary while the device rotates, tomography operates in the reverse manner. Diverse types of tomography devices [24] are available, all comprising essential components: a source of X-rays, a precision rotation stage, and an X-ray detector (as illustrated in Figure 1.11). The collective performance of these three components profoundly influences the final image resolution. The characteristics of the X-ray source are particularly pivotal in ensuring superior resolution. The mechanical precision of the rotation stage is crucial to prevent any degradation of image quality. Additionally, the X-ray detector plays a pivotal role by converting incident X-rays into visible light through luminescent materials. The resultant image is then magnified and projected onto a CCD sensor through optical components.

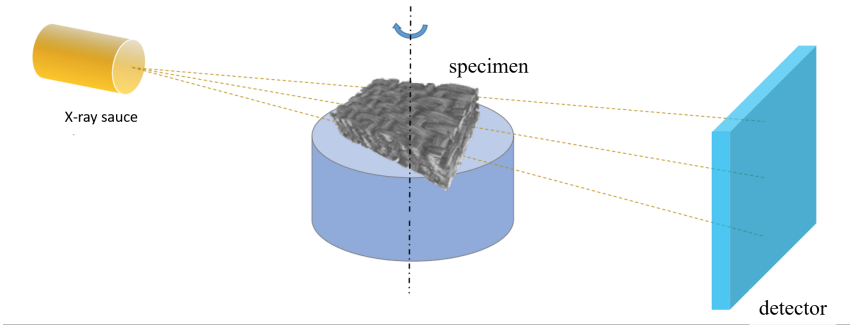

Fig. 1.11: Schematic diagram of an X-ray tomograph [25]

Multiple mechanical tests on fiber yarns, although delicate, are conducted in the literature, including tension, compression, shear and bending tests.

Tension. The fiber yarns are composed of a large number of fibers. When a yarn is subjected to tension, not all of these fibers tense simultaneously [26]. The gradual tensioning of the fibers leads to a nonlinear behavior of the yarn at the beginning of loading. This nonlinearity depends on the material as well as the tow's manufacturing process. It can be observed that it is much less pronounced for a carbon tow than for a glass

tow from Figure 1.12. Quantifying stiffness using the concept of stress is quite challenging. If we consider two different cross-sectional areas of tows, both having the same number of fibers but one with smaller gaps between the fibers and the other with wider gaps, then for the same deformation, the required force is the same. Determining the effective cross-sectional area of the tow under loading is crucial, but it's not straightforward due to the geometric complexity of tows. Therefore, it's more common to characterize the tensile behavior using stiffness in Newtons (N), which is the ratio of force to deformation, rather than using a modulus.

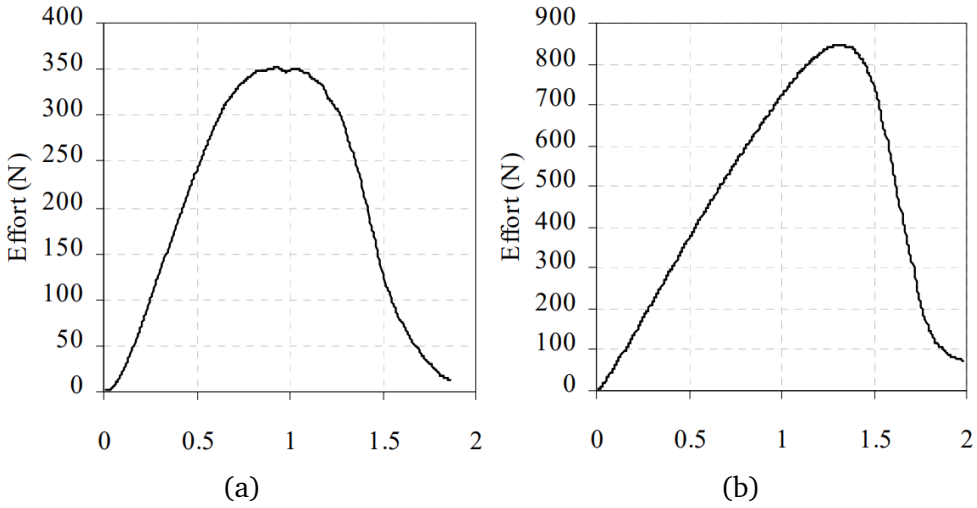

Fig. 1.12: Tensile Behavior of Glass (a) and Carbon (b) yarns [26]

Compaction. The compaction of fiber yarn is the change in its cross-sectional area, which is perpendicular to the fiber direction, as shown in Figure 1.13. When the yarn undergoes compaction, the fibers come closer together, and the voids are filled. The compaction of a yarn involves two major stages: initially, the fibers reorganize to fill the void spaces, often resulting in the formation of fiber bends that give this mode of deformation its elastic behavior. This reorganization gradually halts when no more free space can be filled by fibers. A state of blocking then occurs, where the compression rigidity of the tow tends toward the compression rigidity of the material constituting the fibers. Experimentally identifying this behavior is challenging because conducting pure compaction tests on a yarn removed from the fabric is not easily feasible.. In previous studies describing yarn behavior at the mesoscopic scale, the compaction behavior of the yarn is generally identified through an inverse method based on macroscopic-scale testing [22, 27, 28]. Compaction is one of the primary modes of deformation for a yarn, and it occurs in most of the loadings to which the fabric can be subjected. Intrinsically tied to this compaction is the yarn's fiber density, which has a significant influence on the local permeability of the yarn. Therefore, identifying the compaction behavior is crucial when the objective is to calculate the local permeability of the reinforcement.

Shear. Two modes of shear exist within the fiber yarn: distortion (i.e., shearing within the transverse plane of the yarn) and longitudinal shear (i.e., in the fiber direction). Similar to compaction, the direct identification of these deformation modes is challenging.

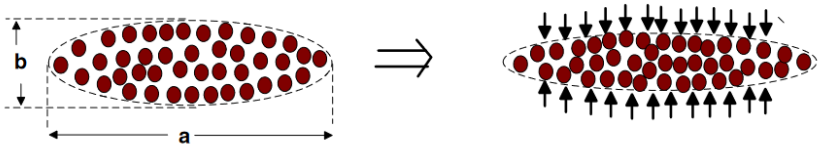

Fig. 1.13: Compaction of yarn due to external pressure. [28]

Distortion corresponds to the change in shape of the yarn within the transverse plane, i.e., its deformation without compaction. Figure 1.14 illustrates two specific transformations corresponding to this mode of deformation. During such a transformation, the fibers rearrange themselves by sliding relatively to each other to adapt to the deformation. At the microscopic scale, flexions of fibers can appear because the fibers are not perfectly aligned. When the yarn is not compacted, there are few interactions between the fibers, so these rearrangements between the fibers are easy. When the yarn is compacted, the numerous interactions between the fibers stiffen this distortion behavior. There is thus a coupling between these two modes of deformation, but its experimental characterization remains challenging.

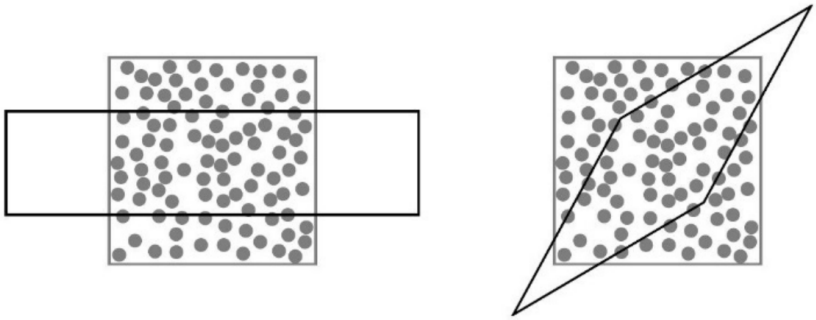

Fig. 1.14: Distorsion of yarn in the transverse plane [10]

Longitudinal shear refers to the longitudinal slipping of the yarns relatively to each other. Figure 1.15 illustrates this transformation. Ideally, this slipping is constrained only by the friction between the yarns. In reality, the sizing and twisting of the yarns stiffen this mode of deformation. Therefore, we are quantifying the cohesion of the fibers within the yarn.

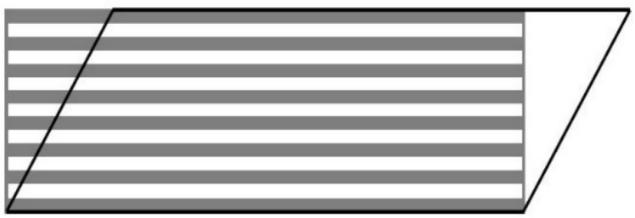

Fig. 1.15: Longitudinal shear of yarn [10]

Bending. While the bending behavior of yarns is still relatively poorly understood, it is important to characterize it, especially when modeling the bending response of an entire

reinforcement. This behavior is also of significant interest in the context of continuous media, as it is directly related to material curvature, a variable not influential in classical theories (related to the first derivative of displacement). When a tow is subjected to three-point bending, three phenomena may occur:

- Longitudinal shearing of the yarn.
- Bending of each fiber.
- Lateral buckling of the fibers at the central support point.

Each fiber inherits its flexural stiffness from its constituent material and geometry, which can be quantified relatively easily assuming the constituent material of the fiber is a linear orthotropic material. Longitudinal shear stiffness can be attributed to the tow due to friction between the fibers. This stiffness is generally too high (i.e., the cohesion among the fibers within the tow is too strong) for longitudinal shear to propagate to the ends of the tested tow, which is why the tow buckles laterally (see Figure 1.16). The bending behavior of the tow, therefore, depends on both longitudinal shear (i.e., local deformation) and the curvature of the fibers within the yarn (i.e., local curvature of the yarn). This dependence on local curvature suggests that the bending behavior of the yarn is not a classical continuum behavior (i.e., Cauchy behavior): since the local behavior depends on local rotations within the medium, the yarn can be considered as a micropolar medium [29, 30]. A model that explicitly takes into account the influence of curvature on the behavior of the reinforcement is proposed in [31].

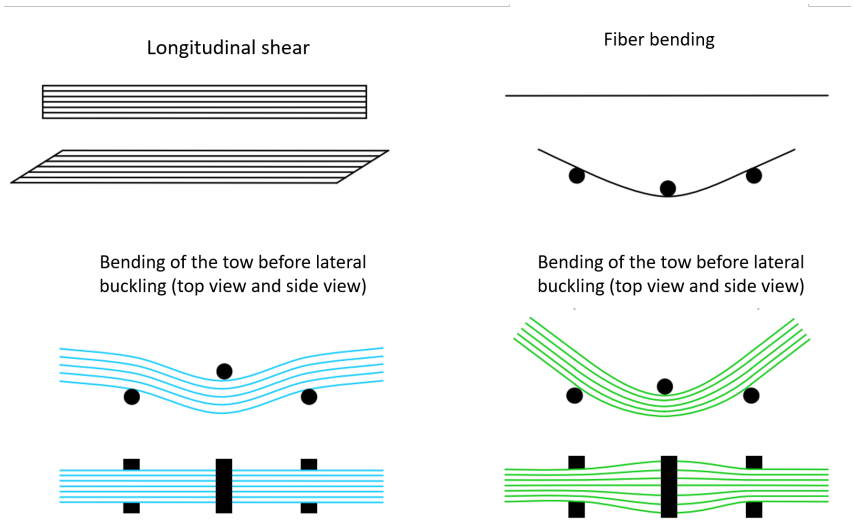

Fig. 1.16: Mechanisms involved in the bending of a yarn [32]

One mesoscopic modeling approach of biaxial NCF at the mesoscopic level is developed by G. Creech and A. K. Pickett in [4] (See Figure 1.17). In the proposed approach, each ply is represented by a layer of solid elements, allowing for the modeling of each tow. Bar elements are added to represent the stitches. The local deformation mechanisms in a biaxial NCF such as the tow compaction, the inter-tow shear and sliding, cross over point

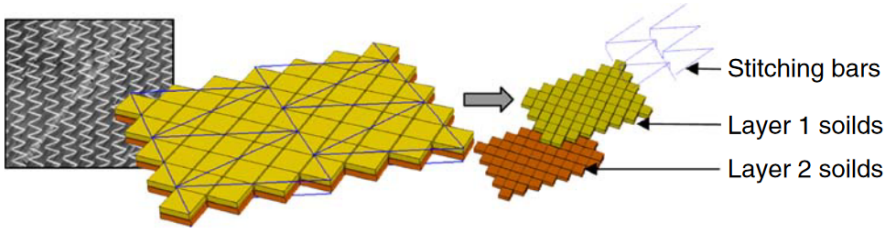

Fig. 1.17: Mesoscopic model of biaxial NCF by G. Creech [4]

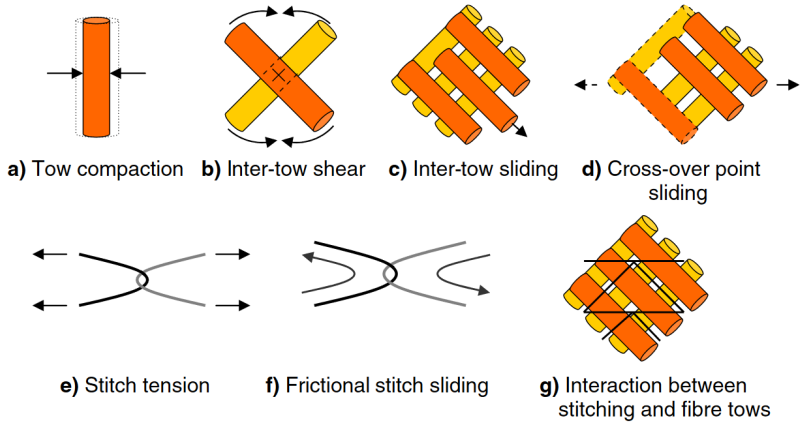

Fig. 1.18: Mesoscale deformation mechanisms in a biaxial NCF [4]

sliding, stitch tension, frictional sliding and interaction between stitch and fiber tows are taken into consideration (See Figure 1.18). The contact behavior between the stitch and the fiber yarns are modelled by adding an additional two node beam element which connects the node on the stitch and the node on the fiber tow. Friction between the yarns and the tool is handled using a contact algorithm with a simple Coulomb coefficient. The model is then used for simulating a Picture frame test and Bias-extension test and draping over a dome. The advantage of this method is to account for local phenomena, notably observing the yarn slippage on the edge of the Bias-test specimen (see Figure 1.19). The mesoscopic analysis effectively captures the asymmetric behavior of the reinforcement in shear. It provides an advantage compared to a macroscopic approach with shell elements and homogenized anisotropic behavior law, which does not account for the asymmetric shear behavior. The mesoscopic model developed therein for the analysis of the draping of NCF composite reinforcements demonstrates interesting capabilities as it allows for the representation of local phenomena. The sliding that occurs within the reinforcement during shaping, the position of the stitches, and their tension are aspects that cannot be currently captured by a macroscopic approach.

However, this model has several limitations. Many parameters are introduced, and not all of them have a clear physical explanation. This can lead to determining some of these parameters through curve fitting rather than actual physical testing. The computational cost is not discussed. The mesh of the Bias-test specimen consists of 36,000 solid elements and 21,000 bar elements. Contact must be managed between all the tows and with the stitches. Although it's not addressed therein, the computational cost is likely to be high.

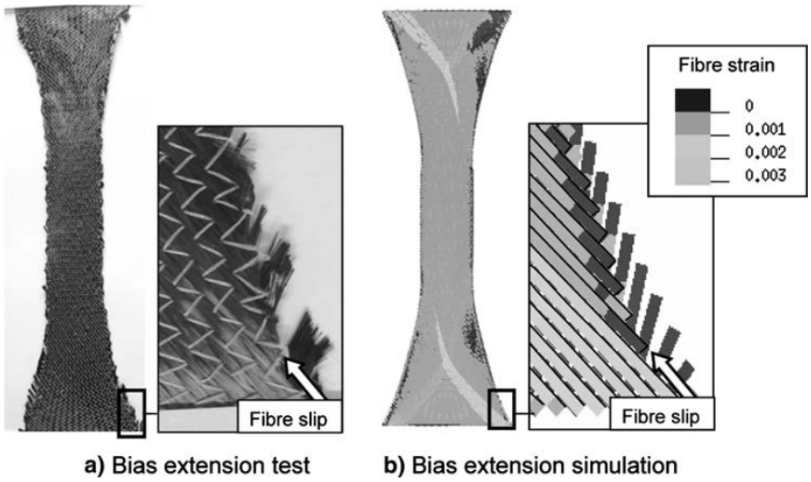

Fig. 1.19: Comparison of bias extension test between experiment and simulation [4]

1.3.3 Mechanical behavior and simulation approach at macroscopic scale

At this scale, mechanical testing is conducted on large sample sizes containing multiple Representative Unit Cells (RUC). Uniaxial or biaxial tension tests are often conducted on woven fabrics due to its initial undulation of yarn. Once the undulation in the loaded direction is reduced to zero, the tows will elongate in the loaded direction. However, NCF has straight fiber yarns, making the tension test results closer to the single yarn tension test. The behavior of the reinforcement in compression in the transverse plane has a significant influence on the quality of the shaping and resin injection steps during the RTM process. When shaping the dry reinforcement, the fiber density and the mechanical performance-to-mass ratio increase as the reinforcement is compressed. The increase in fiber density directly affects the permeability of the reinforcement and, consequently, the flow of resin during the injection step [33, 34]. Compaction tests on UD- and biaxial NCF for different layup-types and relative fiber orientations at the interfaces were conducted in [34]. The experimental setup is shown in Figure 1.20. A specimen of the NCF under study is placed between the two parallel plates of the device and gradually compressed by applying pressure to the upper plate. At the beginning of compression, when the tows reorganize to minimize voids in the reinforcement, the initial stiffness is very low. Then, the stiffness increases significantly as the fiber density becomes sufficiently high. The results allow for a better understanding of their compaction behavior which will be used to parameterize an analytical or simulation model.

The in-plane shear deformation is a major mode in the forming process. The shear behavior of the reinforcement is highly nonlinear because various deformation mechanisms are involved. Characterizing the shear behavior of the reinforcement is essential. Two tests are commonly used by the researchers to investigate the in-plane shear behavior of fabric: the Picture frame test (PFT) and the Bias-extension test (BET) [35].

In a Picture frame test [35, 36, 37], the fabric is placed within an articulated frame, initially in a square shape. The frame is then placed in a tensile testing machine and

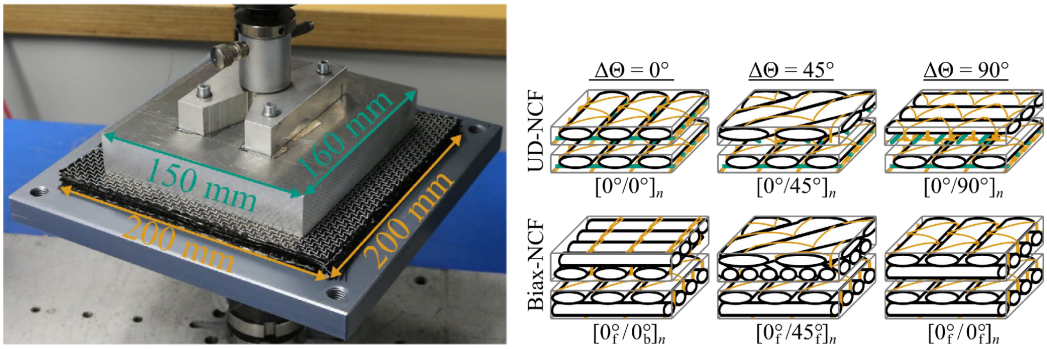

(a) (b)

Fig. 1.20: Compaction tests on NCF (a) Experimental setup (b) Schematic [34]

deformed into a rhombus shape, imposing a pure shear deformation on the fabric (Figure 1.21). The shear angle is defined as the change in angle between the two networks of tows. A simple kinematic calculation allows to relate the frame displacement d to the shear angle γ:

$$\gamma = 90° - 2\arccos\left(\frac{\sqrt{2}L + d}{2L}\right) \tag{1.1}$$

Where L is the frame length and l is the fabric length. The main challenge, even for thin

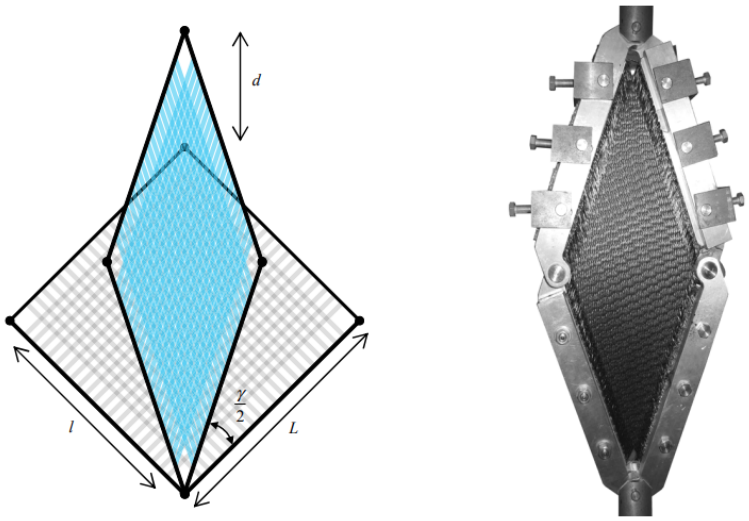

Fig. 1.21: Picture frame test

fabrics, arises from the initial alignment of the fabric, which must be precisely identical to that of the frame. During this test, the aim is to subject the fabric to pure shear, but there inevitably remains an initial angular defect; thus, the kinematics generate tension in the yarns. Thus, the PFT results in pure shear deformations throughout the sample but requires a longer testing time and is more complex to implement [38]. A bias extension test is preferred over it.

The bias-extension test [35, 37, 39] is a simple tensile test on the fabric, in a direction oriented at 45° to the warp and weft networks (Figure 1.22). Assuming infinite tow tensile stiffness and zero fabric shear stiffness, and if the no-slip assumption between the networks is satisfied, three zones form within the specimen: a non-sheared zone, a sheared zone with an angle γ, and a so-called "half-sheared" zone, sheared at an angle $\gamma/2$. With the previous assumptions, a theoretical shear angle can be calculated based on the elongation of the specimen:

$$\gamma = \frac{\pi}{2} - 2\cos^{-1}\left(\frac{D+d}{\sqrt{2}D}\right) \tag{1.2}$$

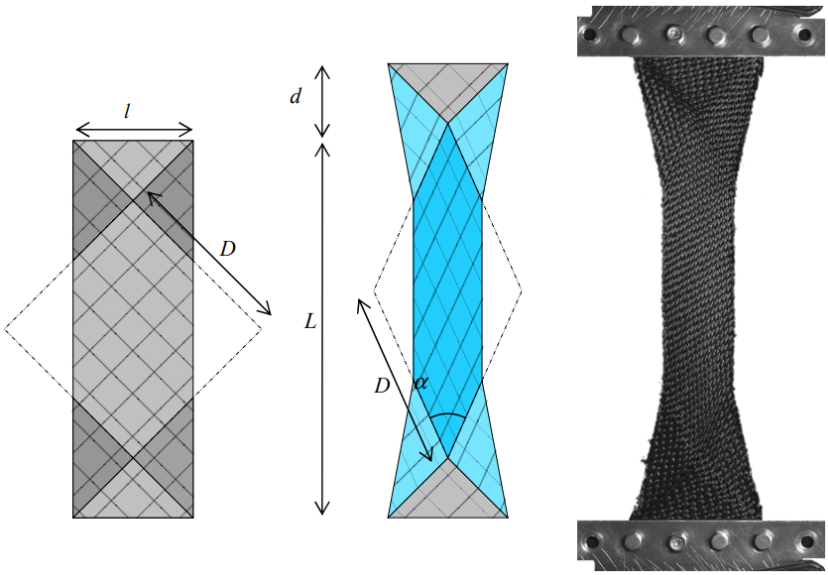

Fig. 1.22: Bias-extension test

Compared to the PFT, the BET offers a simple and quick testing procedure. However, the analysis of results is more complex due to the interaction of components unrelated to shear.

The simulation at macroscopic scale aims to simulate the shaping of textile reinforcement at the scale of the entire part. Two types of models are proposed: the geometric approach and the mechanical approach. The geometric (kinematic) approach is based on simplifications, assuming fiber inextensibility, no shear stiffness, and no specific deformation. In this case, with the absence of different deformation modes, identical results will be presented for the same forming process even if different materials are used. Within the mechanical approach, there are three types of approaches: discrete, semi-discrete, and continuous.

The discrete model considers each individual component of the material, and the model is a discontinuous assembly of finite elements (cf. Figure 1.23). The reinforcement is modeled by nodes connected to each other by bars, shells, and springs aimed at modeling the response in tension, shear, torsion, and bending. This method can simulate wrinkling and reinforcement failure. Two examples are shown in [40, 41].

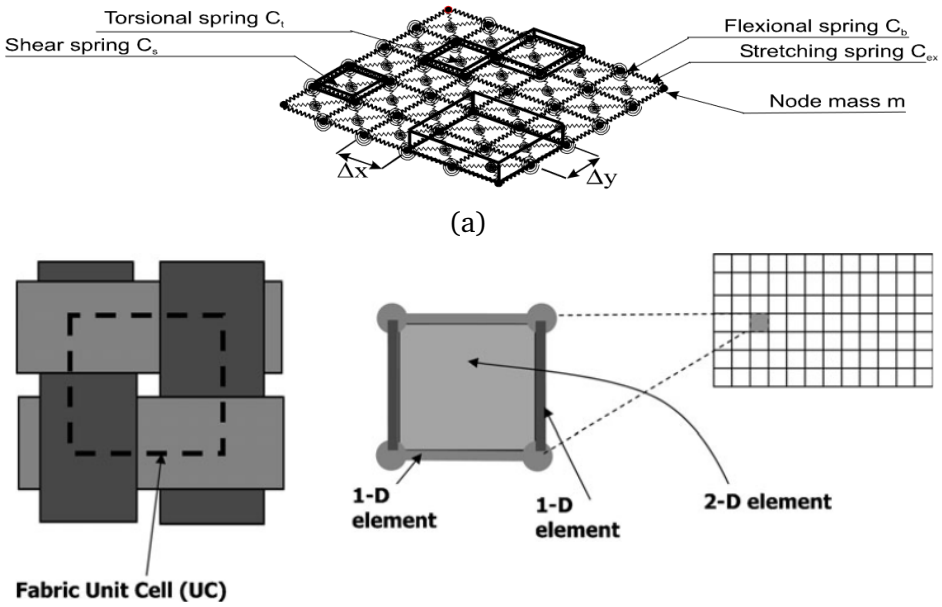

Fig. 1.23: Discrete model (a) [BOU07] [40] (b) [Jau10]] [41]

The continuous model is based on the mechanics of continuous media and considers the reinforcement as an anisotropic continuum (cf. Figure 1.24). The medium is typically discretized using shell or membrane elements or volumetric elements for thick 3D fabrics and interlocks. Several constitutive models have been considered. Hypoelastic models [42, 43, 44] or hyperelastic models [45] have provided satisfactory results. Good results for simulating the stamping of prepregs are presented in [46, 47].

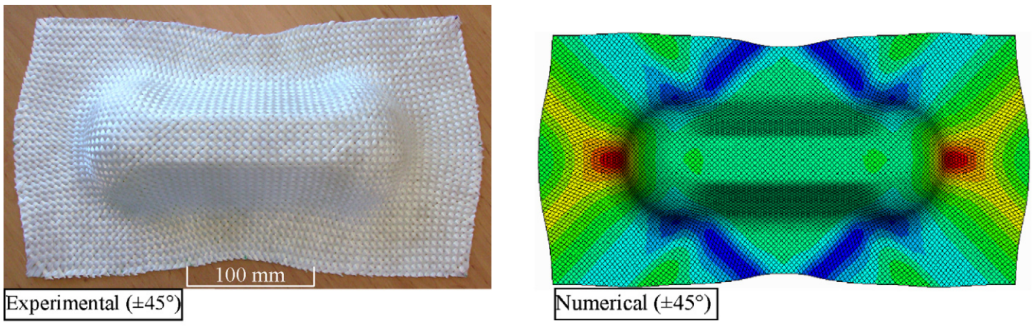

Fig. 1.24: Experimental and numerical results of forming on a double dome [42]

The semi-discrete approach combines both approaches. A specific finite element is constructed based on the behavior of the mesoscopic unit cell, and the textile composite is then seen as a collection of discrete woven unit cells subjected to membrane [48] and bending loads [49].

For the simulation of NCF, a macroscopic model is developed at KIT [5]. In this model the fabric is modelled by membrane elements (cf. Figure 1.25). Superimposed shell elements are then applied to achieve the bending stiffness independent of the membrane

stiffness. Thus, membrane and bending stiffness are decoupled. It is shown that the model is well suited to predict fibre orientation, preform contour as well as the formation of macroscopic winkling. Moreover, critical areas for gaping can be estimated based on the in-plane transverse strain field.

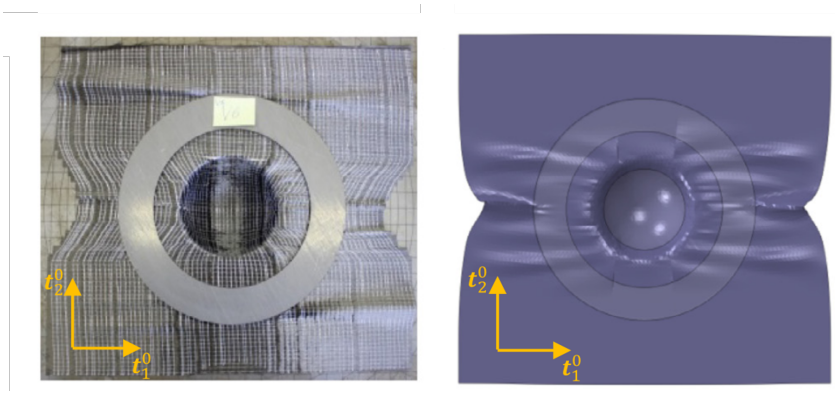

Fig. 1.25: Macroscopic model of UD NCF by F. Schirmaier [5], comparison of experimental results and simulation results

CHAPTER 2

Mesoscopic modeling of Bi-axial NCF from experimental observation

A mesoscopic finite element (FE) model is proposed in this chapter to integrate a description of fiber yarn reinforcement at a mesoscopic level, enabling the simulation of shaping large preforms. This approach differs from previous research by utilizing a more accurate FE model. When dealing with NCFs, the fiber yarns and stitches are discretely modeled and individually treated as a continuum. The geometrical aspects of the stitches and fiber yarns are explicitly defined using X-ray tomography results. The mechanical properties of the individual fiber yarns and stitches are determined through experimental testing at the mesoscopic level. This model is developed in the commercial FE simulation software, ABAQUS-Explicit. The possible benefits of this model are the accurate observation of local deformations and the prediction of local defects, particularly gaping and inter-fiber slippage, which are hardly treated from macroscopic FE methods.

Contents

2.1 modeling strategy

In order to develop a suitable mesoscopic finite element (FE) model, two main aspects must be considered: generating an accurate geometrical model and obtaining appropriate material data for the constitutive model.

To understand its 3D internal geometry, the X-ray tomography is an effective tool [21, 50]. Section 2.3.1 and 2.3.2 present the geometrical modeling of fiber yarns based on this method. The explicit description of the local configuration of stitches is crucial as different stitch patterns exist due to varying types of NCFs and manufacturing processes, and these patterns significantly influence the mechanical properties of the entire NCF [51]. A number of studies have provided mathematical descriptions of different stitch patterns [52, 53, 54], and the use of a trace fiber technique for stitching path analysis was introduced in [55]. This technique relies on the principles of light refraction and reflection. Section 2.3.3 presents the geometrical modeling of a tricot stitch based on its knitting pattern.

Section 2.4 and Section 2.5 present the constitutive laws that are applied to the fiber yarns and stitches, respectively. Appropriate experimental tests on single yarns and stitches at the mesoscopic level are designed and conducted to obtain input material data. In these tests, the individual yarn and stitch are isolated from bi-axial NCFs by cutting the stitch loop connections. Section 2.5.2 presents a new method for considering the interaction between yarn and stitch.

2.2 Studied biaxial NCF

A biaxial (MD600) non-crimp fabric without binder is studied in the present work, as shown in Figure 2.1. The fabrics are manufactured by Zoltek™, an American manufacturer and produced from their PX35-50K continuous carbon fibre (CF) heavy tows. The two carbon fiber yarn layers which orient $0°/90°$ are bound together during the production process with loop formation in the warp direction with a polyester (PE) yarn in a tricot pattern. The material characteristics are shown in Table 2.1 from the technical documents of Zoltek.

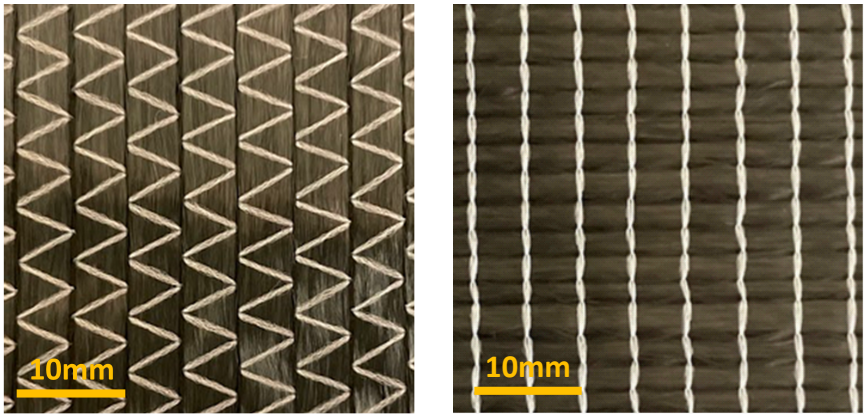

Fig. 2.1: Presentation of studied biaxial NCF

Manufacturer's style	**ZOLTEK™ PX35 MULTI-DIRECTIONAL FABRICS**
Fiber	50K Carbon
Fiber Diameter	7.2 microns
Fiber Orientation	$0°/90°$
Stitch	polyester
Areal density	
Fiber yarn	300 (8.85)g/m^2
Stitch	8 (.235)g/m^2
Fabric	608 (17.9)g/m^2

Tab. 2.1: Characteristics of studied biaxial NCF from technical documents of Zoltek

2.3 Geometrical modeling of Bi-axial NCF

Geometrical models play a vital role in numerical studies, especially at the mesoscopic scale, by accurately predicting the forming process and mechanical properties of composites. In recent years, two primary approaches have emerged for creating geometrical models of composite reinforcements:

- Software tools such as TexGen [56] and WiseTex [57, 58]
- Directly from tomography results [21, 50, 59]

The first widely used approach involves automatically generating a finite element model from the textile simulation software based on a pure geometrical approach (cf. Figure 2.2a). These software tools make certain assumptions about the shapes, offering a convenient and automated method for creating the model. The input parameters for the model often comes from the manufacturer's specification and the measured or estimated dimensions [60]. The second approach provides a higher level of accuracy and variability in describing the geometrical details. Figure 2.2b shows the model of a woven fabric from a view of XY plane [25]. However, when dealing with biaxial NCFs, the tomography

method faces challenges in the image segmentation process for stitches since the geometric information of stitches is hidden within the warp and weft fiber yarns.

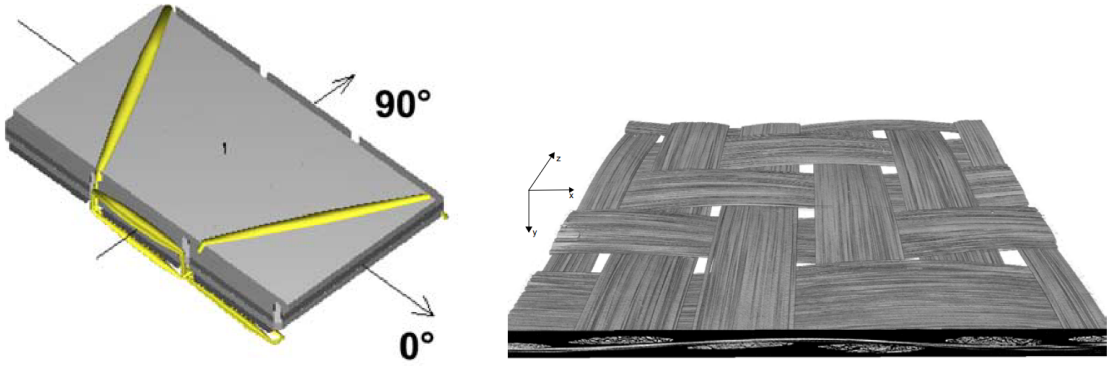

(a) (b)

Fig. 2.2: Two approaches for creating geometrical model (a) NCF model from software tools [57] (b) Model from tomography [25]

This section presents a combination of the purely geometrical approach and X-ray tomography to create an accurate 3D geometrical model of biaxial NCF with separate modeling of stitches and fiber yarns. Detailed geometrical parameters obtained from the tomography results are used as inputs to create nodes and elements in the model using equations in MATLAB. Discretization of the resulting geometrical descriptions will then be used to produce FE meshes. The adjustability of these equations enables greater flexibility in modifying the geometry, thereby facilitating the development of tailored fabrics with optimized deformation behavior.

2.3.1 X-ray tomography

The X-ray tomography was conducted on a new microCT platform developed by the company RX Solutions in collaboration with LaMCoS and Mateis laboratories. A resolution of the order of 15 μm utilized, enabling the reconstruction of several elementary cells within the same reinforcement, which is ideal for mesoscopic observations. These observations at the mesoscopic scale allow for the exploration of real geometries. Figure 2.3 presents a 3D view of an $18 \times 18\,\mathrm{mm}^2$ bi-axial NCF sample, showcasing both the weft and warp yarn faces using Fiji software [61].

To implement a pure geometry approach, accurate geometrical parameters of biaxial NCF must be considered, which include the gap between adjacent fiber yarns and the section (thickness and width) of both weft and warp yarns. In an ideal NCF, assuming no crimp is present, the small compression of the fiber yarn caused by the tensioned stitch is neglected. The gap arises as an opening area between fiber yarns when the knitting needle pierces the two fibrous plies during the knitting process. Furthermore, the stretching of the stitch during the forming process can cause changes in the thickness and width of the weft and warp yarns, resulting in a larger gap. During the preform impregnation process, this gap provides pathways for resin flow. Once the composite is fully consolidated, this

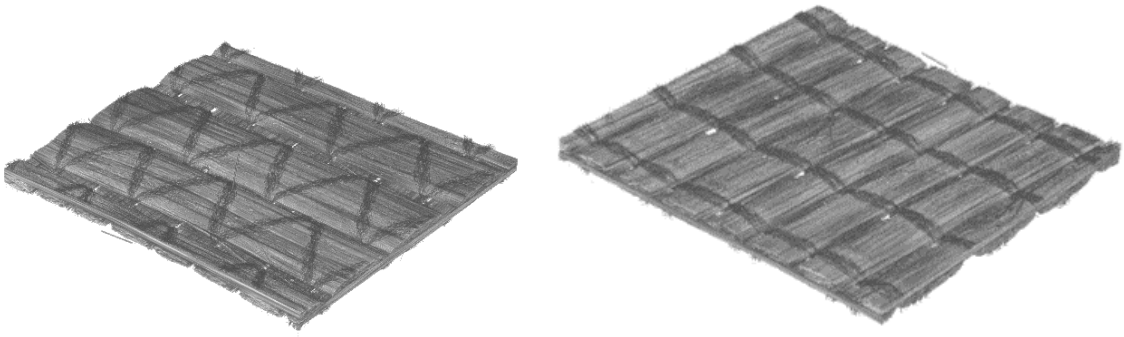

(a) (b)

Fig. 2.3: Tomography 3D view of a Bi-axial NCF sample ($18 \times 18mm^2$) (a) View of warp yarn with *zig-zag* stitch pattern (b) View of weft yarn with *looped* stitch pattern

gap may contribute to the formation of resin-rich areas, which can play a crucial role in the initiation of damage. By incorporating these parameters into a precise geometric model, further investigations can be conducted to predict the forming behavior of NCFs.

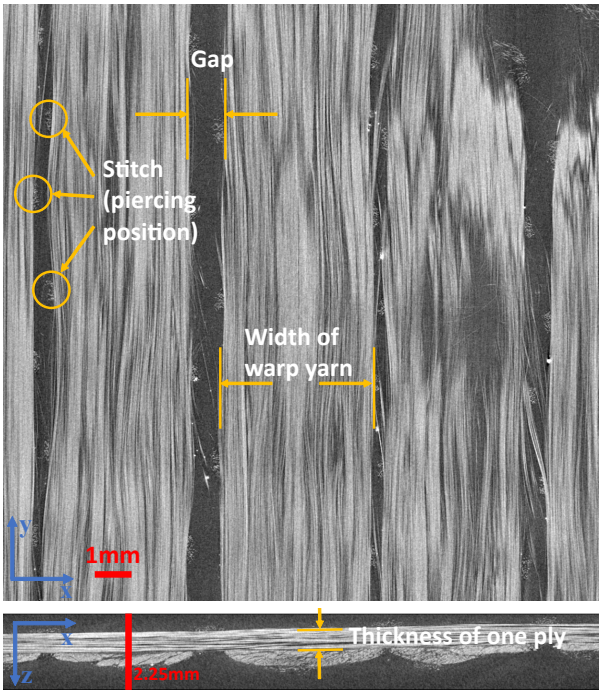

Fig. 2.4: Orthogonal views of biaxial NCF

Figure 2.4 illustrates the orthogonal views obtained from the tomography results. From these views, measurements of the gap, width, and thickness are conducted, and average values are calculated. The geometrical parameters are shown in Table 2.3.

	Width W	Thickness H	Gap G
Warp yarn	4.59 mm	0.38 mm	0.39 mm
Weft yarn	2.08 mm	0.38 mm	0.40 mm

Tab. 2.2: Geometrical parameters (average values) measured on tomography images of a biaxial NCF sample.

2.3.2 Geometrical modeling of fiber yarn

At the mesoscopic scale, the individual fiber yarns are regarded as continuous media. The initial configuration of the fiber yarns of NCF assumes a straight form without any undulations. Thus, only the assumptions about cross-section shapes of fiber yarns should be made. Figure 2.5 shows fiber yarns' model with different cross-section shape, which includes the circular [62, 63], flat [64], elliptical [65], runway [66], biconvex [67] and rectangular [4] shapes.

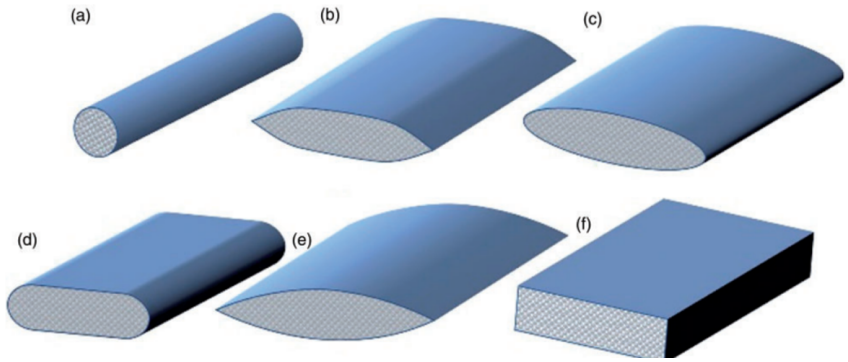

Fig. 2.5: Common cross-sections of yarns: (a) circular; (b) flat; (c) elliptical; (d) runway; (e) biconvex; (f) rectangular [55]

In our case, the cross-sectional area is mathematically modeled as an elliptical shape, while the fiber yarns are represented using hexahedral solid elements. Figure 2.6 shows the geometrical parameters on a finite element model of biaxial NCF. The geometrical characteristics of the fiber yarns are determined by the following parameters:

- n_c: Number of warp yarns in the model
- n_t: Number of weft yarns in the model
- w_c: Initial width of warp yarn model
- w_t: Initial width of weft yarn model
- g_c: Initial gap between warp yarn
- g_t: Initial gap between weft yarn
- h: Initial thickness of one ply of yarn
- hr_c: Used to define the thickness of the edge of warp yarn
- hr_t: Used to define the thickness of the edge of weft yarn
- ms_c: Mesh size of warp yarn

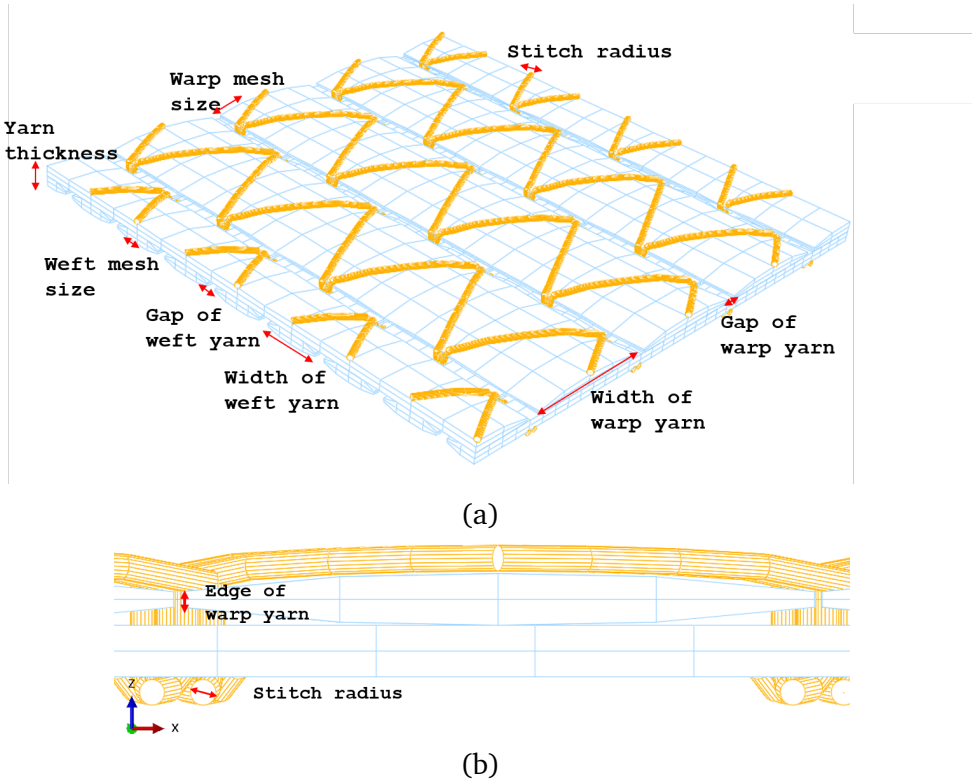

Fig. 2.6: Geometrical parameters (a) on a finite element model of biaxial NCF (b) section view

- ms_t: Mesh size of weft yarn
- ms_h: Mesh size in thickness direction

The nc and nt define the dimension of the model and the codes' repetitions to create model. The final model length L_c and width L_t are:

$$L_c = n_t \cdot (w_t + g_t) \tag{2.1}$$

$$L_t = n_c \cdot (w_c + g_c) \tag{2.2}$$

The w_c, w_t, g_c, g_t and h are geometrical parameters obtained from tomographic measurements. Additionally, the parameters hr_c and hr_t are introduced to account for the non-zero thickness of the hexahedral elements at the edges. The ms_c, ms_t and ms_h define the mesh size. To establish the nodal coordinates for constructing the finite elements, elliptical equations are employed. In the case where the fiber yarns have a thickness comprising two elements ($ms_h = \frac{h}{2}$), the coordinates of the warp yarn nodes on the $x-z$ section are determined by the following set of three equations:

$$\begin{cases} z_{top} = \frac{h}{2} + \frac{h}{2}\sqrt{1 - \left(\frac{x}{w_c/2+hr_c}\right)^2}, \\ z_{middle} = \frac{h}{2}, \\ z_{bottom} = \frac{h}{2} - \frac{h}{2}\sqrt{1 - \left(\frac{x}{w_c/2+hr_c}\right)^2}, \end{cases} \tag{2.3}$$

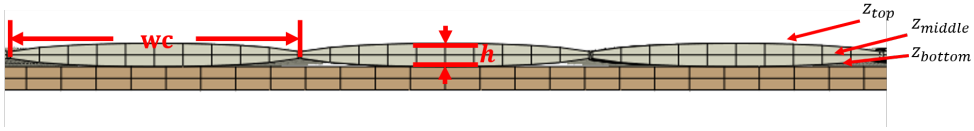

Fig. 2.7: Section view of warp yarn of bi-axial NCF

The sectional model of warp yarn of biaxial NCF is shown in Figure 2.7.

And for the weft yarn which is straight along the X direction:

$$\begin{cases} z_{top} = -\frac{h}{2} + \frac{h}{2}\sqrt{1 - \left(\frac{x}{w_t/2 + hr_t}\right)^2}, \\ z_{middle} = -\frac{h}{2}, \\ z_{bottom} = -\frac{h}{2} - \frac{h}{2}\sqrt{1 - \left(\frac{x}{w_t/2 + hr_t}\right)^2}, \end{cases} \tag{2.4}$$

After obtaining the coordinates for all the nodes on the yarn, hexahedral first-order elements are generated by connecting the nodes in a specified order. As shown in Figure 2.8, the black number is the local node number and the green number represents its order in forming an element. Thus, the red Element N will be generated through the following code:

$*Element$

$N, 312, 315, 316, 313, 375, 378, 379, 376$

The fiber orientation should be specified on each element since the fabric has a specific behavior along this orientation. In ABAQUS, this is set up by "**ORIENTATION, DEFINITION=OFFSET TO NODES**" . This code helps to define a coordinate system by giving node number order (4,7,8) for point $a, b,$ and c, where point c is the origin of the local coordinate system and the connection of points $a - c$ helps to define the local X direction, which in our case is known as the fiber orientation.

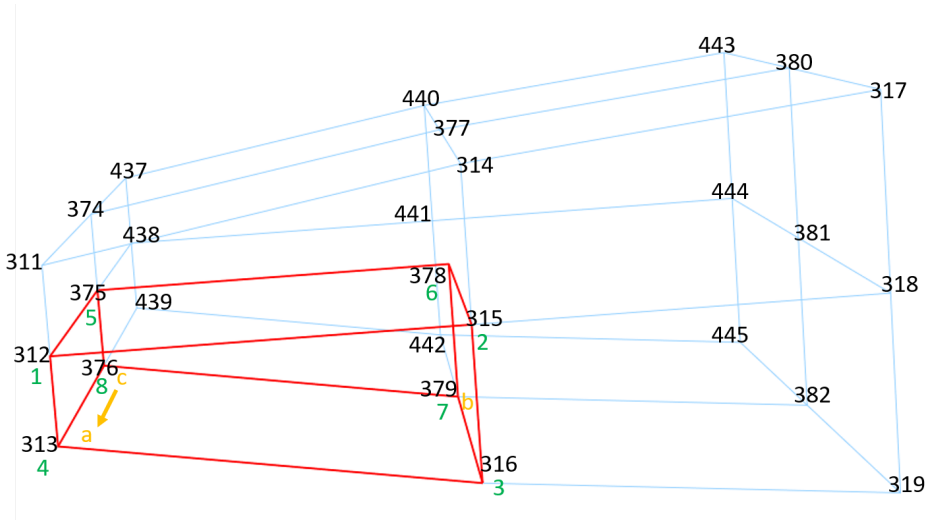

Fig. 2.8: Set up fiber orientation on one element

2.3.3 Geometrical modeling of tricot stitch

The loop geometry of stitch is described based on its knitting pattern. The diameter of stitch is considered to be constant. The stitch that wraps around the warp and weft yarn is computed based on the equilibrium equations of the yarn as suggested in [68]. It is assumed that the stitch pierces through the two plies in a straight line. The parameters utilized for the stitch are:

- r: Radius of the cross section
- gs_t: Initial spacing between stitch and yarn in the Z axis
- gs_w: Initial spacing between stitch and yarn in the X or Y axis
- ms_s: Mesh size of stitch

In order to ensure the continuity and smoothness of the interpolation points along the yarn path, a set of discrete points is employed to fit the 3D trajectory of the stitches. Figure 2.9 depicts a unit cell model of biaxial NCF, highlighting a single stitch loop represented in red. The starting point of the stitch loop is chosen as Node A (x_a, y_a, z_a), located at the half-stitch position on the bottom side. Subsequently, it wraps around the half weft yarn, progressing from Node A to Node B (x_b, y_b, z_b). A straight stitch then penetrates the two plies, connecting Node B to Node C (x_c, y_c, z_c). From Node C, the stitch meanders around the warp yarn, advancing towards Node D (x_d, y_d, z_d). At Node D, another straight stitch is formed, piercing the plies to reach Node E (x_e, y_e, z_e). Continuing on, the stitch warps around the second weft fiber yarn, proceeding towards Node F (x_f, y_f, z_f). Finally, the stitch follows a straight path from Node F to Node G (x_g, y_g, z_g) and wraps around the previous stitch loop, forming a loop connection. The functions used to describe the stitch loop that wraps around the kth warp yarn are expressed as:

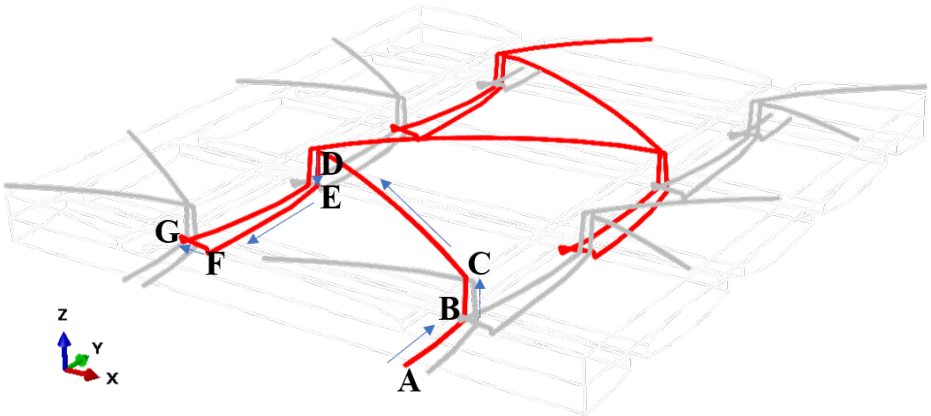

Fig. 2.9: Geometrical model of stitch with one entire loop of stitch in red

From Node A to Node B:

$$\begin{cases} x = (x_b - x_a)/(y_b - y_a) \cdot (y - y_a) + x_a, \\ \\ z = -\frac{h}{2} - gs_t - r - \left(\frac{h}{2}\right)\sqrt{1 - \left(\frac{y}{y_b - y_a}\right)^2}, \end{cases} \quad 0 \le y \le y_b \tag{2.5}$$

Where

$$\begin{cases} x_a = k \cdot (w_c + g_c) + w_c/2 + (g_c - 4 \cdot r)/2), \\ x_b = k \cdot (w_c + g_c) + w_c/2 + g_c - 5 \cdot r - gs_w, \\ y_a = 0, \\ y_b = (w_t + g_t)/2 + r, \end{cases} \tag{2.6}$$

From Node B to Node C:

$$\begin{cases} x = x_b, \\ \\ y = y_b, \end{cases} \quad -\frac{h}{2} \le z \le \frac{h}{2} \tag{2.7}$$

Where

$$\begin{cases} x_c = x_b, \\ y_c = y_b, \end{cases} \tag{2.8}$$

From Node C to Node D:

$$\begin{cases} y = (y_d - y_c)/(x_d - x_c) \cdot (x - x_c) + y_c, \\ \\ z = \frac{h}{2} + gs_t + r + \left(\frac{h}{2}\right)\sqrt{1 - \left(\frac{x - (x_c + x_d)/2}{(x_d - x_c)/2}\right)^2}, \end{cases} \quad x_d \le x \le x_c \tag{2.9}$$

Where

$$\begin{cases} x_d = (k-1) \cdot (w_c + g_c) + w_c/2 + g_c - 3 \cdot r - gs_w, \\ y_d = \frac{3}{2} \cdot (w_t + g_t) + r, \end{cases} \tag{2.10}$$

From Node D to Node E:

$$\begin{cases} x = x_d, \\ \\ y = y_d, \end{cases} \quad -\frac{h}{2} \le z \le \frac{h}{2} \tag{2.11}$$

Where

$$\begin{cases} x_e = x_d, \\ y_e = y_d, \end{cases} \tag{2.12}$$

From Node E to Node F:

$$\begin{cases} x = (x_f - x_e)/(y_f - y_e) \cdot (y - y_e) + x_e, \\ \\ z = -\frac{h}{2} - gs_t - r - \left(\frac{h}{2}\right)\sqrt{1 - \left(\frac{y - (y_e + y_f)/2}{(y_e - y_f)/2}\right)^2}, \end{cases} \quad y_f \le y \le y_e \tag{2.13}$$

Where

$$\begin{cases} x_f = (k-1) \cdot (w_c + g_c) + w_c/2 + 5 \cdot r + gs_w, \\ y_f = \frac{1}{2} \cdot (w_t + g_t) - r, \end{cases} \tag{2.14}$$

From Node F to Node G:

$$\begin{cases} y = y_f, \\ \qquad\qquad x_g \leq x \leq x_f \\ z = z_f + r, \end{cases} \tag{2.15}$$

Where

$$x_g = x_f - 6 \cdot r, \tag{2.16}$$

These steps can be sequentially repeated to form a complete stitch model, and all the

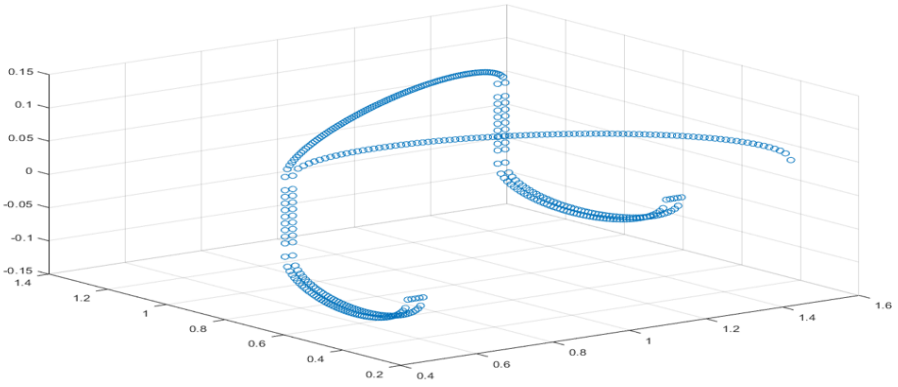

Fig. 2.10: Nodes on the stitch model created by equations in MATLAB

nodes are generated using equations in Matlab before being transferred to ABAQUS inp file format. Figure 2.10 illustrates the scatterplot generated in MATLAB.

2.4 Finite element modeling of fiber yarn

Once the geometrical model of biaxial NCF is established, the next step is to develop a finite element model that accurately represents the material behavior. This section introduces the constitutive material modeling of fiber yarn deformation and experimental tests at mesoscopic scale. Based on prior studies [45, 69, 70], the mesoscopic scale considers each fiber yarn as a homogeneous and continuous medium. In ABAQUS, C3D8 solid hexahedral elements with a sufficient number of integration points are used to simulate the fiber yarns. A minimum of two elements in the cross-section was empirically determined as a suitable compromise between accuracy and computational cost. The transverse shear test and bending test are implemented on single yarn for the experimental characterization.

2.4.1 Constitutive material modeling of fiber yarn deformation

The carbon fiber yarns consist of numerous individual filaments, leading to high stiffness along the fiber orientation and relatively low shear stiffness. Additionally, considering the potential for filament slip and the inextensibility assumption made for the yarn, the bending stiffness of carbon fiber yarns is small and should be treated independently from

other deformation mechanisms. The constitutive law utilized for the carbon fiber yarn is a hyperelastic model developed by A. Charmetant [45]. This model accounts for four deformation modes of the fiber yarn: elongation along the fiber direction, cross-sectional compaction, transverse shear (cross-sectional distortion), and longitudinal shear along the fiber direction. This theory does not take its bending behavior into account and only the

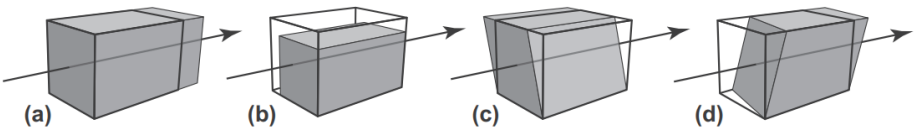

Fig. 2.11: Four deformation modes of fiber yarn (a) elongation (b) compaction of cross section (c) transverse shear (d) longitudinal shear [45]

transverse shear behavior gives a very little bending stiffness. To incorporate the desired bending stiffness, reinforced beam elements are embedded within each fiber yarn.

Hyperelastic constitutive law

The hyperelastic equation defines the stress-strain relation for the solid by specifying its strain energy density w as a function of deformation gradient tensor:

$$w = w(\underline{\underline{F}}) \tag{2.17}$$

The general form of the strain energy density is determined through experimental observation. The formula for strain energy density always incorporates material properties that can be tailored to accurately describe the behavior of a specific material [71]. It has been revealed [72] that to obey the principle of material indifference, it is necessary and sufficient that the strain energy is a function of the right Cauchy-Green tensor $\underline{\underline{C}}$ and the invariants of $\underline{\underline{C}}$ is used to ensure that the constitutive equation is objective (recall that the invariants of a tensor remain constant regardless of changes in basis).

$$w = w(I_1, I_2, I_3, I_4, I_5) \tag{2.18}$$

Where I_1 to I_3 are the classical invariants of the right Cauchy-Green strain tensor $\underline{\underline{C}}$ and I_4 to I_5 are invariants mixed the structure tensors $\underline{\underline{M}} = \underline{M} \otimes \underline{M}$ and $\underline{M}$ is a unit vector of fiber orientation.

$$I_1 = \operatorname{tr} \underline{\underline{C}}, \tag{2.19}$$

$$I_2 = \frac{1}{2}\left(\operatorname{tr} \underline{\underline{C}}^2 - \operatorname{tr} \underline{\underline{C}}^2\right), \tag{2.20}$$

$$I_3 = \det \underline{\underline{C}}, \tag{2.21}$$

$$I_4 = \underline{\underline{C}} : \underline{\underline{M}}, \tag{2.22}$$

$$I_5 = \underline{\underline{C}}^2 : \underline{\underline{M}}. \tag{2.23}$$

The four deformation modes are translated in the form of combinations of physical invariants, linked to the invariants of the right Cauchy-Green tensor $\underline{\underline{C}}$. The four physical invariants associated with each deformation mode are defined as:

$$I_{\text{elong}} = \frac{1}{2} \ln I_4 \tag{2.24}$$

$$I_{\text{comp}} = \frac{1}{4} \ln \left(\frac{I_3}{I_4} \right) \tag{2.25}$$

$$I_{\text{sh}} = \sqrt{\frac{I_5}{I_4^2} - 1} \tag{2.26}$$

$$I_{\text{dist}} = \frac{1}{2} \ln \left(\frac{I_1 I_4 - I_5}{2\sqrt{I_3 I_4}} + \sqrt{\left(\frac{I_1 I_4 - I_5}{2\sqrt{I_3 I_4}} \right)^2 - 1} \right) \tag{2.27}$$

Based on the decoupling hypothesis, the strain energy density can then be expressed as a function of these physical invariants relating to the different deformation modes:

$$\begin{aligned} w &= w\left(I_{\text{elong}}, I_{\text{comp}}, I_{\text{dist}}, I_{\text{sh}}\right) \\ &= w_{\text{elong}}(I_{\text{elong}}) + w_{\text{comp}}(I_{\text{comp}}) + w_{\text{dist}}(I_{\text{dist}}) + w_{\text{sh}}(I_{\text{sh}}) \end{aligned} \tag{2.28}$$

And the second Piola–Kirchhoff stress tensor can be obtained based on this energy density:

$$\underline{\underline{S}} = 2\frac{\partial w}{\partial \underline{\underline{C}}} = \sum_{mode} 2\frac{\partial w}{\partial I_{mode}} \frac{\partial I_{mode}}{\partial \underline{\underline{C}}} \tag{2.29}$$

The stress tensor of Cauchy is expressed as:

$$\underline{\underline{\sigma}} = \frac{1}{J} \underline{\underline{F}} \cdot \underline{\underline{S}} \cdot \underline{\underline{F}}^T \tag{2.30}$$

The strain energy density functions associated with elongation (w_{elong}), transverse (w_{dist}) and longitudinal (w_{sh}) shear are defined as standard quadratic elastic potentials [45]:

$$w_{\text{elong}} = \frac{1}{2} K_{\text{elong}} I_{\text{elong}}^2, \tag{2.31a}$$

$$w_{\text{dist}} = \frac{1}{2} K_{\text{dist}} I_{\text{dist}}^2, \tag{2.31b}$$

$$w_{\text{sh}} = \frac{1}{2} K_{\text{sh}} I_{\text{sh}}^2. \tag{2.31c}$$

For the cross-sectional compaction strain energy density w_{comp}, Charmetant et al. proposed a power-based function to represent the microscopic nonlinear phenomena that occur during transverse compaction of the yarn [45]:

$$w_{\text{comp}} = \begin{cases} K_{\text{comp}} \left| I_{\text{comp}} \right|^p & \text{if } I_{\text{comp}} \leq 0, \\ 0 & \text{otherwise.} \end{cases} \tag{2.31d}$$

Abaqus User subroutine VUMAT

The hyperelastic constitutive law for the carbon fiber yarn is implemented in ABAQUS Explicit using the user subroutine VUMAT. Within VUMAT, two variables must be defined:

- $stressNew$: Stress tensor at each material point at the end of the increment
- $stateNew$: State variables at each material point at the end of the increment.

The steps can be described as follows:

- Read deformation gradient $\underline{\underline{F}}$ (variable: $defgradNew$) and right stretch tensor $\underline{\underline{U}}$ (variable: $strectchNew$) in the base of the initial orientation
- Calculate Right Cauchy Green tensor $\underline{\underline{C}}$ in the base of the initial orientation and the classical invariants I_1, I_2, I_3, I_4, I_5
- Calculate physical strain invariants $I_{\text{elong}}, I_{\text{comp}}, I_{\text{sh}}, I_{\text{dist}}$ and store them in $stateNew$
- Calculate the energy associated with these four deformation modes $w_{\text{elong}}, w_{\text{comp}}, w_{\text{sh}}, w_{\text{dist}}$ and store them in $stateNew$
- Calculate the second Piola-Kirchhoff tensor $\underline{\underline{S}}$ and the stress tensor $\underline{\underline{\sigma}}$ (variable: $stressNew$)

Embedded beam element for reinforcement

In the 3D finite element modeling of textile reinforcements on a macroscopic scale, it has been demonstrated that a Cauchy mechanical model cannot simultaneously possess a significantly low shear stiffness (due to potential fiber slippage) and a bending stiffness originating from the fibers themselves [73]. This limitation arises from the standard continuum mechanics approach of Cauchy. Figure 2.12a showcases a three-point bending test conducted on an interlock reinforcement, while Figure 2.12b demonstrates a simulation based on a macroscopic hyperelastic model for anisotropic materials. This model accounts for six deformation modes: elongation in warp and weft directions, in-plane shear, transverse shear in warp and weft directions, and transverse compaction. The results reveal that the two outer portions remain nearly horizontal, resembling the behavior observed in models utilizing bar elements (Figure 2.12d). Conversely, the experimental results align more closely with a vertical orientation.

Three approaches are commonly used to correctly model the bending of fibrous materials. The first approach is the neighboring element method [74]. This method calculates the curvature of a finite element from the position of its neighboring elements. The second approach is the second gradient approach where the strain energy density depends both on the right Cauchy green tensor $\underline{\underline{C}}$ and on its gradient [75]. The last approach is the laminate approach, which considers the single layer of fiber composite as a laminate with varying Young's modulus settings [76].

modeling single carbon fiber yarn at the meso scale presents a similar challenge due to the presence of 50,000 filaments in each yarn, resulting in a very high tensile stiffness and a very low shear stiffness. Therefore, we propose the integration of embedded beam elements within the fiber yarns to enhance the material's bending stiffness. These beam

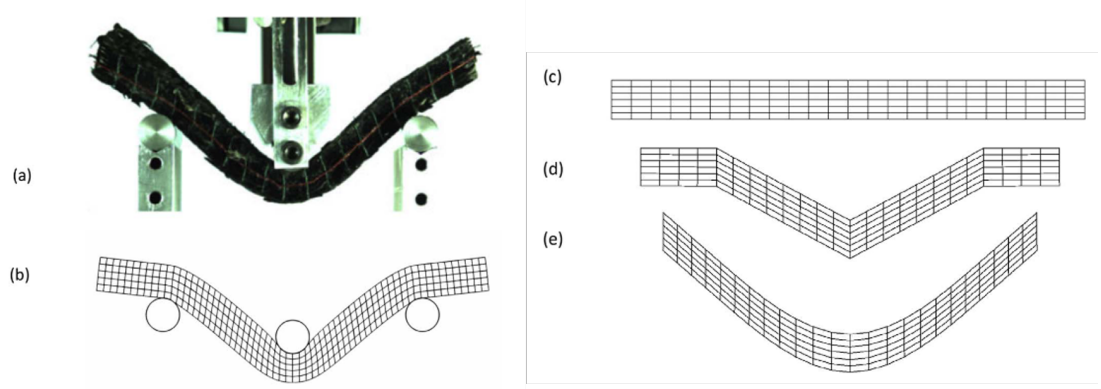

Fig. 2.12: Three point bending of an interlock reinforcement. (a) Experiment, (b) simulation based on a model of Cauchy, (c) hinged bar system: initial, (d) hinged bar system: deformed shape, (e) beams instead of bars [73]

elements are located at the center of each fiber yarn and share the same nodes as the yarns. Sharing nodes eliminates the need to consider contact between the beam and solid elements. Since the fiber yarns are assumed to be inextensible, the tensile behavior of the beam elements can be disregarded, as it does not impact the overall deformation mechanism. Thus, the bending stiffness of these beam elements is determined exclusively by their Young's modulus and moment of inertia. Tests of shear simulation (Unit cell simulation and Bias-extension test simulation) will be introduced in Chapter 4 to validate that these beam elements have little effects on the shear deformation modes. A simulation

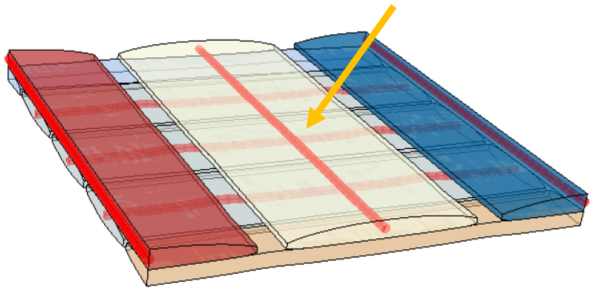

Fig. 2.13: Embedded beam element for reinforcement

of a three-point bending test was conducted with the hyperelastic constitutive law (see Figure 2.14b) and hyper + embedded beam elements (see Figure 2.14c). The length of the specimen of bi-axial NCF is $150\,\mathrm{mm}$ along the warp yarn direction with only one ply and the imposed load is a displacement of $30\,\mathrm{mm}$ at the central support point. It can be observed that with the embedded beam elements, the two outer parts are rising. Consequently, the incorporation of these beam elements improves the material's out-of-plane bending stiffness.

It is worth noting that characterizing the in-plane bending stiffness of fiber yarns remains a challenging task, and it has not been considered in our study. To account for the in-plane and out-of-plane bending, an anisotropic beam element could be defined

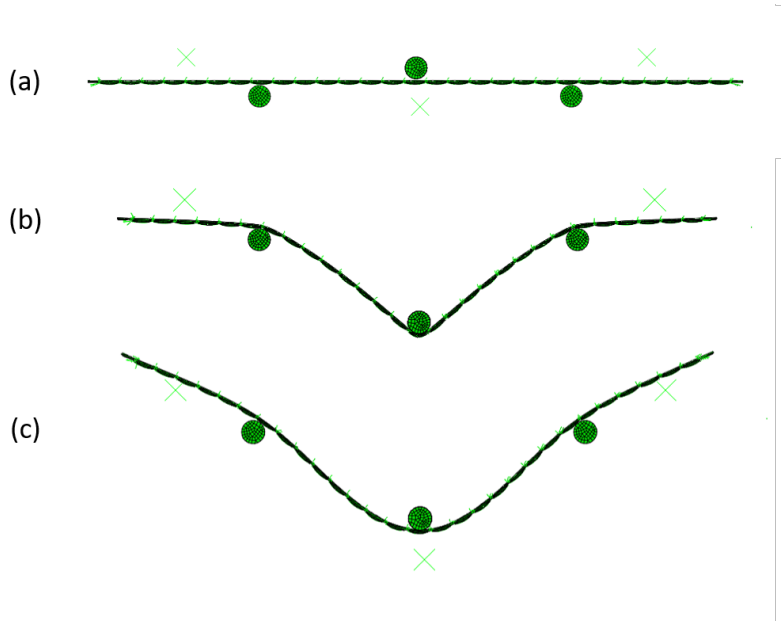

Fig. 2.14: Three point bending test simulation (a) Initial configuration (b) Hyperelastic law (c) Hyperelastic law and embedded beam elements

by incorporating the respective section inertia moments, denoted as I_{11} and I_{22}, after determining the in-plane shear stiffness.

2.4.2 Experimental test observation

Experimental tests shoud be carried out to characterize the parameters associated with these deformation modes in Equations 2.31 [77, 78]. The elongation behavior is often directly identified from the tensile test of a single yarn, as shown in Figure 2.15a. The carbon fiber reinforcement exhibits a special material behavior, resulting in significantly higher tensile stiffness in the warp and weft yarn direction compared to other material properties. The material can be considered as quasi-insensible in the yarn direction. Therefore, in our study, we have selected an exceptionally large and constant tensile stiffness (which is same as in [78]) to represent the material's elongation behavior.

The compaction and distortion behavior of the material is characterized using compression tests conducted on single yarns [79, 80], as depicted in Figure 2.15b. The compaction parameter can be directly calculated, whereas the distortion parameter requires measurement through inverse identification. In our study, we implement an inverse approach with an optimisation loop. The parameters determined for fabric B in [78] are used as the initial values in the optimization loop. The final parameters for the compaction and distortion are given in Table **??**.

Concerning the longitudinal shear, a uniaxial tension test was conducted in [77] on the woven fabric. During this test, elongation and longitudinal shear deformation occur. Then the parameter of transverse shear can be identified by an inverse approach after knowing the elongation behavior.

However for the biaxial NCF material, since it has no crimps, no longitudinal shear

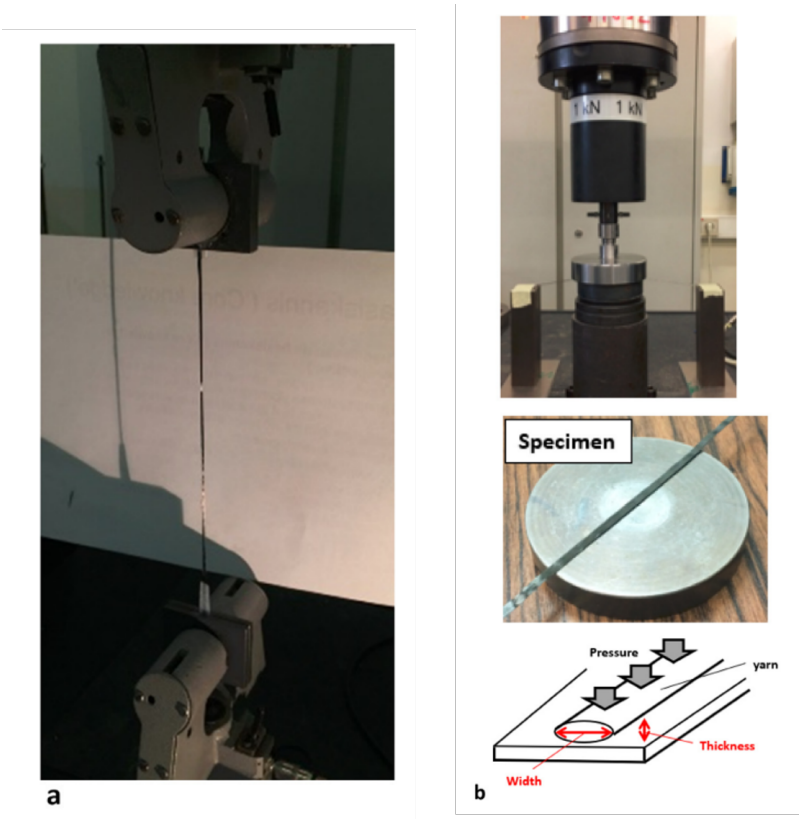

Fig. 2.15: Experimental test to identify the model of yarns [78] (a) Tensile test (b) Compaction test

deformation occur in this test. A new shear test is introduced in this section. A cantilever bending test was also conducted to characterize the out-of-plane bending stiffness of fiber yarn.

Longitudinal shear test of fiber yarn

The single yarn's shear test was performed on the electromechanical traction machine Lloyd 1kN. Fig.2.16a shows the schema of this test. One single yarn was cut at both ends, leaving only a few carbon fiber filaments (as less as possible) which were then arranged into a Z-shape. This specimen is then attached to the surfaces of the jaws using double-sided tape to provide a larger surface area for the clamping tool to hold, thus preventing the slippage between the tool and the specimen. The length of the middle shear zone was 100mm with the carbon fiber orientation strictly parallel to the stretching direction. The degree of freedom of the specimen is blocked in the direction of the thickness. We consider that we only require simple shear kinematics.

During the longitudinal shear test, slippage between the individual filaments within the carbon fiber yarns plays a significant role. As there is no constraint in the vertical direction of the stretch, the filaments tend to separate, resulting in a decrease in the shear force. To minimize this separation and accurately capture the shear behavior, it is essential to use a lower stretch speed and ensure a high-quality sample preparation, which guarantees reliable experimental results. Figure 2.17 illustrates the machine force

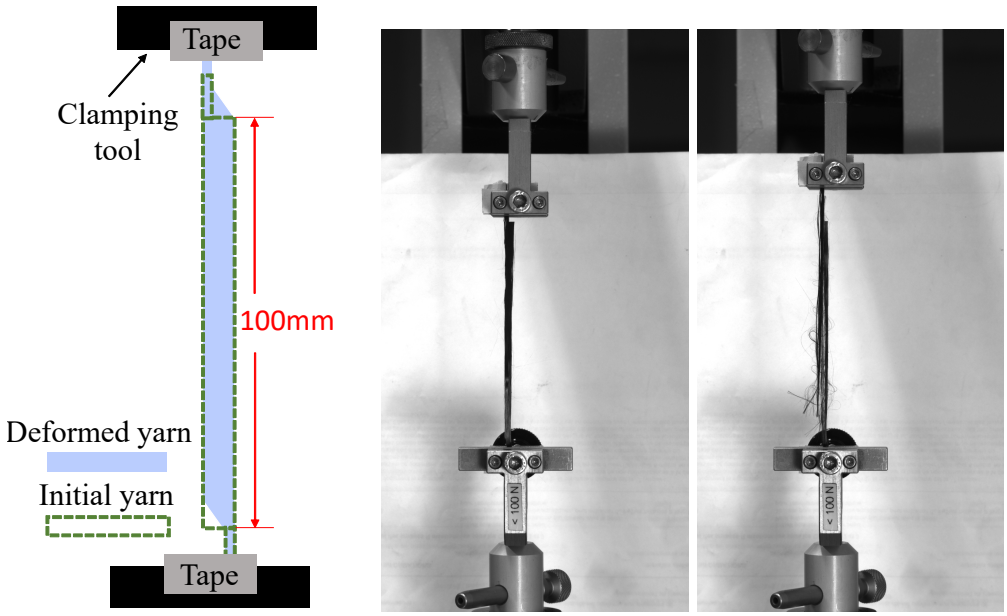

Fig. 2.16: Single yarn longitudinal shear test (a) Schema (b) Initial configuration (c) Deformed configuration

recorded by a 10N sensor during the longitudinal shear test. Initially, the shear force on the single fiber yarn increases, but as the testing machine continues to stretch, the shear force gradually decreases. This decrease in shear force is a direct consequence of the separation of the fiber filaments within the yarn.

In order to identify the longitudinal shear parameter, an inverse approach is employed. A numerical study on the sample with same dimensions was conducted and the parameter is shown in Table 2.3.

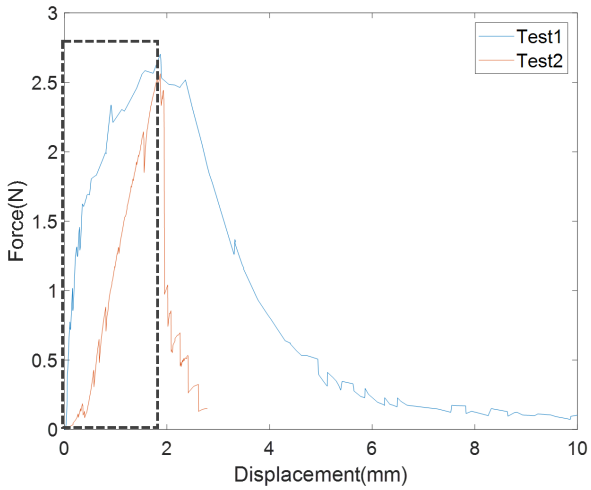

Fig. 2.17: Single yarn shear test: Machine Force versus Machine Displacement with data used indicated within the black dashed box

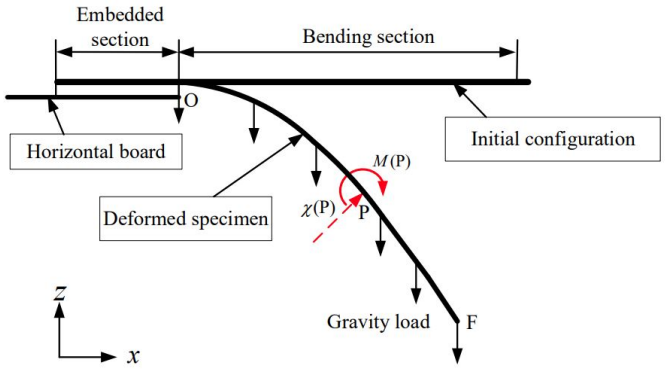

Fig. 2.18: Schema Pierce cantilever bending test [1]

Cantilever test for out-of plane bending behavior

The cantilever test is initially introduced by Peirce [81] who observed that the way a fabric drapes or flexes under its own weight depends on its stiffness, which is still in use nowadays [82, 83, 84]. One end of the specimen is fixed by the device and the other end is free, as shown in Figure 2.18. In this test, the relation between the bending moment M and the curvature χ is assumed to be linear. :

$$M = \frac{G}{\chi} \tag{2.32}$$

Where G is the bending stiffness.

The empirical relation between the flexural rigidity S and the mass has been established by Peirce in function of the inclination θ as:

$$S = \frac{G}{w} = \frac{l^3 \cos\left(\frac{\theta}{2}\right)}{8 \tan\theta} \tag{2.33}$$

Where w is area weight, l is the overhanging length, θ is the angle of inclination is measured from the horizontal to the secant line, which is drawn between the fixed end and the free end of the cantilevered fabric strip.

The Peirce bench consists of bending a test piece of fabric subjected to its own weight until the free end is in contact with an inclined plane at 41.5°. The amount of inclination simplifies Peirce's equation as:

$$S = \frac{l^3}{8} \tag{2.34}$$

Figure 2.19 shows the experiment of a standard cantilever bending test with an inclined plane at $41.5°$. The sample is one single yarn with $200\,\mathrm{mm}$ length. The overhanging length is $140\,\mathrm{mm}$ and the bending stiffness of studied bi-axial NCF G_{yarn} is $1.029\,\mathrm{N\,mm}$. All material parameters for the fiber yarn are presented in Table 2.3.

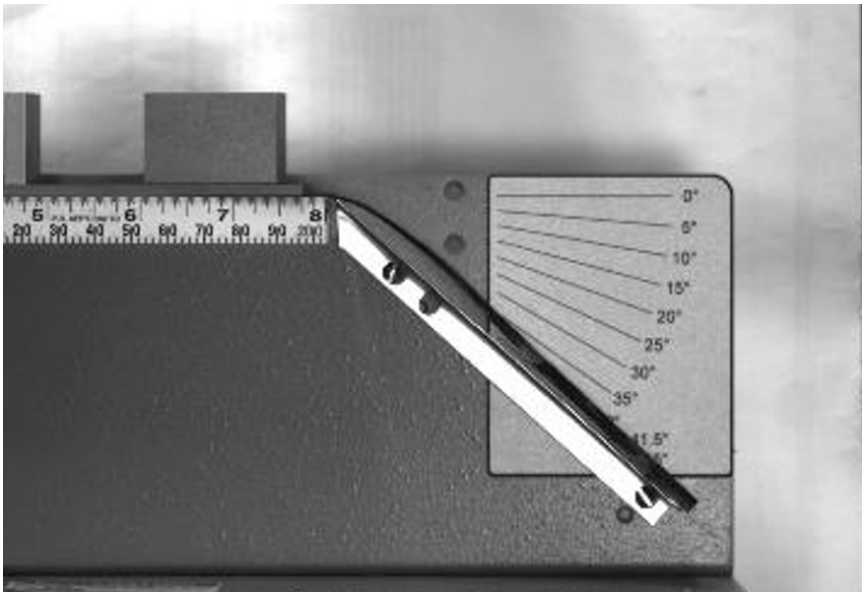

Fig. 2.19: Experimental cantilever bending test

Symbol	Value	Physical interpretation	Calibration method
K_{elong}	108 500 MPa	Tensile stiffness along the fibers	values from [78], Fabric B
K_{dist}	0.6 MPa	Transversal shear stiffness	
K_{comp}	1.25 MPa	Cross-sectional compaction stiffness	
p	1.84	Cross-sectional compaction exponent	
K_{sh}	2.2 MPa	Longitudinal shear stiffness	experimental test (see Figure 2.16)
G_{yarn}	1.029 N mm	Bending stiffness	experimental test (see Figure 2.19)

Tab. 2.3: Designation, value, physical interpretation, and calibration method of the material parameters in the Charmetant constitutive model used in this study

2.5 Finite element modeling of tricot stitch

The stitch plays a crucial role in influencing the mechanical behavior of NCF, particularly at the mesoscopic scale. It serves to connect the two plies of fiber yarns and has the potential to compress the yarns during deformation. The tightness of the stitch can have significant implications during the forming process. A tightly stitched NCF may result in more gaps forming, while a loosely stitched NCF may lead to increased slippage between the two plies of fiber yarns. To address these considerations, a thermo-elastic pre-tension step is implemented which involves reducing the temperature in order to tension the stitch which is modelled by expansible elements. Given that the cross-section of stitch is significantly smaller than its length, we simplify the geometry by representing it as a one-dimensional wire. Only its traction and bending behavior are taken into consideration. The experimental bending and traction characterization of an individual stitch are presented in this section.

2.5.1 Constitutive Material modeling of Stitch Deformation

The stitch in the FE model is commonly represented by two-node beam or bar elements. Figure 2.20 illustrates the configuration of a sheared NCF in the experiment. In the *zig-zag* stitch pattern of the $0°/90°$ bi-axial NCF, one segment of the stitch is consistently under tension, while the other segment is compressed, leading to the observation of bent stitches. Considering that a bar element does not account for the bending behavior of the stitch, it is preferable to utilize a beam element instead. Its bending stiffness and tensile stiffness need to be identified.

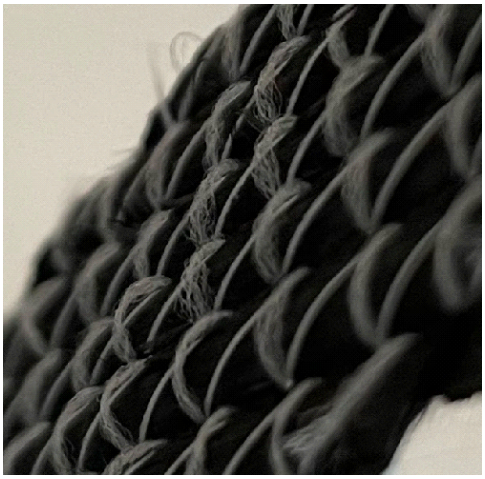

Fig. 2.20: Bent stitch during the shear deformation of bi-axial NCF

General section beam element

For a circular section stitch, a classic beam's bending stiffness G_s is computed based on its tensile module E_s and its sectional diameter D_s as:

$$G_s = E_s \cdot \frac{\pi \cdot D_s^4}{64} \tag{2.35}$$

This function will result in a higher bending stiffness for stitch used in bi-axial NCF. Therefore, a general section beam element is used in ABAQUS ($*Beam \quad General \quad Section$) in order to give a user-define inertia moment. Then the bending stiffness G_s is calculated directly by this inertia moment I_s as:

$$G_s = E_s \cdot I_s \tag{2.36}$$

A single stitch traction test was performed to determine its tensile modulus E_s, while a cantilever test was conducted to determine its bending stiffness G_s. The user-define inertia moment I_s is then obtained by dividing these two values.

Traction test

A single stitch is extracted from the bi-axial NCF and cut into approximately 250mm in length. At both ends, the stitch is wrapped around two small metal pieces, and the ends are secured with clamps. The initial length of the stitch is 90mm, and it is stretched until it reaches the point of fracture. The relationship between machine force and machine displacement is presented in Figure 2.21 and the tensile behavior of the stitch is assumed to be linear. The tensile modulus can be expressed as:

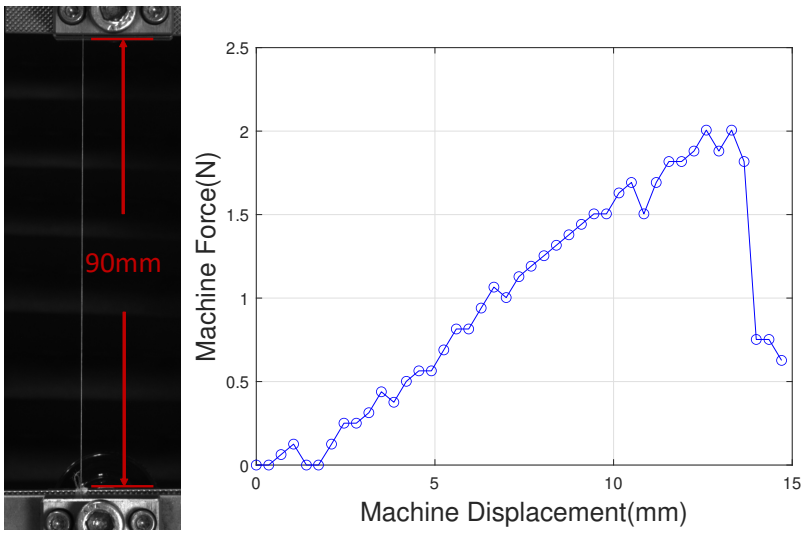

Fig. 2.21: Stitch traction test

$$E_s = \frac{F_s \cdot L_s}{A_s \cdot dL_s} \tag{2.37}$$

where F_s is the machine force and A_s is the cross section of the stitch, L_s is the initial length of stitch and dL_s is the stretch length.

Bending test

The bending behavior of the stitch in this study is assumed to be linear. We also conducted a Peirce bending test to determine the stitch bending behavior. Single stitch specimen was extracted from the NCF through cutting its neighboring stitch loop. However, it is inevitable that the extracted stitch will bend in the initial configuration as it wraps around the yarn. Although this does not affect tensile tests as the stitch is straightened during the test, it significantly impacts bending tests. To mitigate this effect, the extracted stitch was straightened for more than three months by placing weights on both ends and then the straightest part was selected.

As illustrated in Figure 2.22, the stitch was clamped at point B and inclined towards point A at an angle of inclination, denoted as θ. During the test, the overhanging length, referred to as l, was measured. To measure this length accurately, a pair of scissors was

used to cut the stitch at point B after the test was completed. The bending stiffness of the stitch G_s can be expressed as:

$$G_s = \frac{l_s^3 \cos\left(\frac{\theta}{2}\right)}{8 \tan\theta} \cdot \omega_s \tag{2.38}$$

Where l_s is the overhanging length of the stitch, θ is the angle of inclination, and $\omega_s = 4.33 \times 10^{-7}\,\mathrm{N\,mm^{-1}}$ is the weight per unit length of the stitch, calculated from the density of polyester ($1.38\,\mathrm{g\,cm^{-3}}$) and the sectional area of the stitch ($0.0314\,\mathrm{mm^2}$).

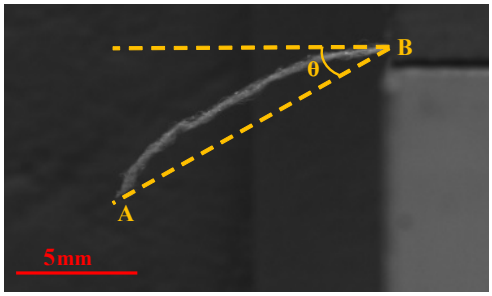

Fig. 2.22: Single stitch cantilever test

All material parameters for the stitch were calibrated through original experimental tests, as also referenced in Table 2.4.

Symbol	Value	Designation	Calibration method
E_s	$350\,\mathrm{MPa}$	Young's modulus	Tensile test (see Figure 2.21)
G_s	$0.000\,56\,\mathrm{N\,mm^2}$	Bending stiffness	Bending test (see Figure 2.22, see Equ. 2.38)
I_s	$0.000\,001\,6\,\mathrm{mm^4}$	Moment of inertia	Tensile and bending test (see Equ. 2.36)
r	$0.1\,\mathrm{mm}$	Cross-section radius	Tomography measurements
ϵ_x^{th}	0.12	thermal strain	Trial-and-error approach

Tab. 2.4: Designation, value, and calibration method of the material parameters for the stitch.

2.5.2 Pretension step

The slippage between the two plies of fiber yarns and between the stitch and yarns in the biaxial NCF is more significant compared to those in woven fabric. As a result, they cannot be overlooked in numerical studies, and addressing this issue is one of the main objectives of the mesoscopic modeling approach. Figure 2.23 illustrates the slip of the yarns in the biaxial NCF. A yarn is slipping through the stitches in its own longitudinal direction. Movement in the other two dimensions is restricted by either the other yarns or the stitches. In a shear test, depicted in Figure2.24, the initial yarns are colored white below the straight chain stitch (highlighted in red). Following the shear deformation, it is evident that the stitch remains relatively straight while the white part exhibits a stepped shape. The black region between them represents the slip that occurs between the stitch

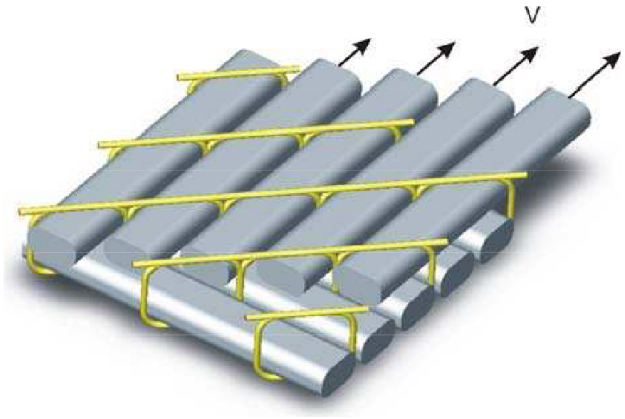

Fig. 2.23: Schematic of slip of the yarns relative to the stitches [85]

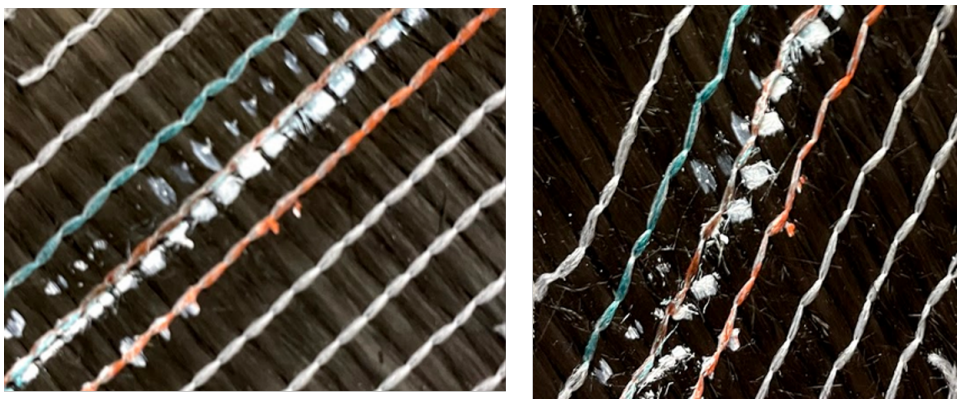

Fig. 2.24: Slip between stitch and yarn during a shear deformation

and yarns.
During the knitting process, the stitch was first stretched before it wrapped around the fiber yarns. It is necessary to reproduce the correct state of tension in the stitch threads and, therefore, account for frictional resistance to relative slip between the yarns and stitches. It is evident that if the stitch is only stretched at the boundary, the tension will not be uniformly distributed.

To address the issue of the complex interaction between fiber yarns and stitches in NCFs, various approaches have been proposed and developed in the literature. One approach is to use an additional artificial elastic bar element, as shown in figure2.25, to connect the nodes of fiber yarns with their adjacent nodes on the stitch, as proposed by G. Creech [4]. However, the Creech's model is a coarse model which can represent the mechanical behaviours and only aims to simulate the draping process without observing the local deformation. And including a high number of connection beam elements in our model seems impractical. Bel [6] introduced an anisotropic Coulomb friction law with sliding threshold to model the interaction. By setting a sliding force threshold, slips occur only for a nonzero tangential force in the case of a zero normal force. Another approach is proposed by Ten Thije [85] who found that the friction is partly of a Coulomb type and partly viscous. A partly viscous friction was then added in the finite element simulation.

In our study, we introduce a thermo-elastic pretension step to simulate this process

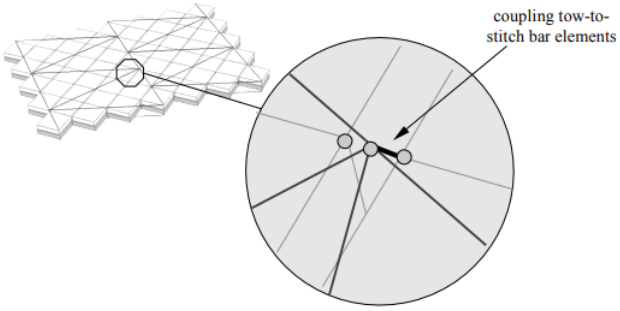

Fig. 2.25: Model of G. Creech by using an additional bar element

before the numerical study instead of implementing the special friction law. With the artificial dropping in temperature, the stitch naturally shrinks in order to simulate the state of tension in the stitching and the state of fiber compaction in the yarns. In Abaqus, the beam elements for the stitch are set as thermally expandable. Its thermal strain ϵ_x^{th} is given by the user defined beam expansion coefficient α and the change of temperature Δt as:

$$\epsilon_x^{th} = \alpha \cdot \Delta t \tag{2.39}$$

Since the deformation of stitch will then be limited by the warp and weft yarn,the given stitch tension σ_x can be expressed as:

$$\sigma_x = E_s \cdot (\epsilon_x - \epsilon_x^{th}) \tag{2.40}$$

Where E_s is the Young's modulus and ϵ_x is the strain of stitch. An inverse approach is used here to determine the thermal strain of stitch. Figure 2.26 illustrates the deformed configurations under various thermal strain parameters. In cases of insufficient thermal strain, the structure remains noticeably loose, and significant slip between the yarn and stitch, as well as between yarns, becomes apparent. Conversely, excessive thermal strain causes the fiber yarns to experience excessive and unrealistic compression. The final thermal strain is shown in Table 2.4

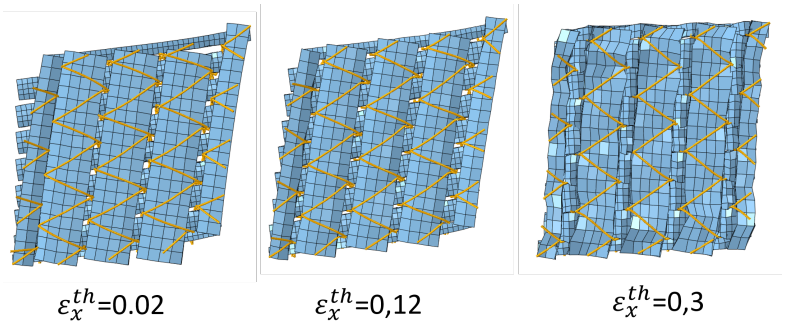

Fig. 2.26: Model deformed under different thermal strain

As we mentioned above, this shrinking step will cause the stitch being tensioned and lead to a compression of the fiber yarns. The gap between the adjacent fiber yarns will

then increase, as shown in Figure 2.27. The compression of the fiber yarn during this step was calculated and incorporated into the initial geometry model. The initial input dimensions of the warp yarn, h and w_c, are then adjusted to match the tomography measurements, h_{final} and w_{cfinal} respectively. The flow chart depicting the whole process for FE mesoscopic modeling is presented in 2.28. Meanwhile, the stitch compresses the shape of the fiber yarn section into a semi-elliptical form.

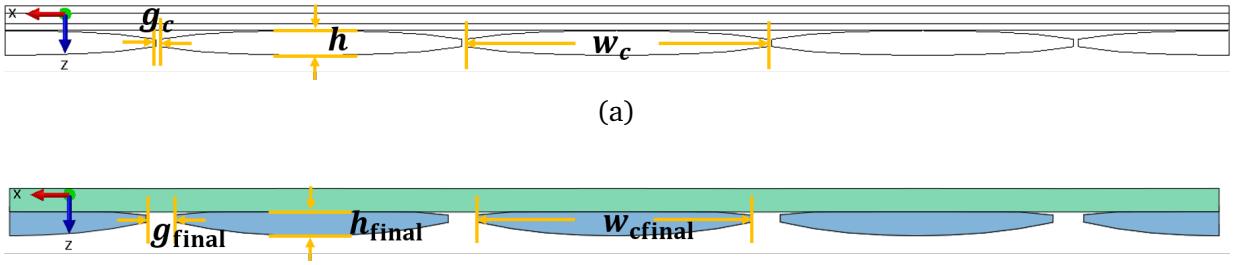

(a)

(b)

Fig. 2.27: Cross-sections of the Biaxial NCF geometrical model before (a) and after (b) the stitch pre-tension step.

The final assembly model is presented in the Figure 2.29.

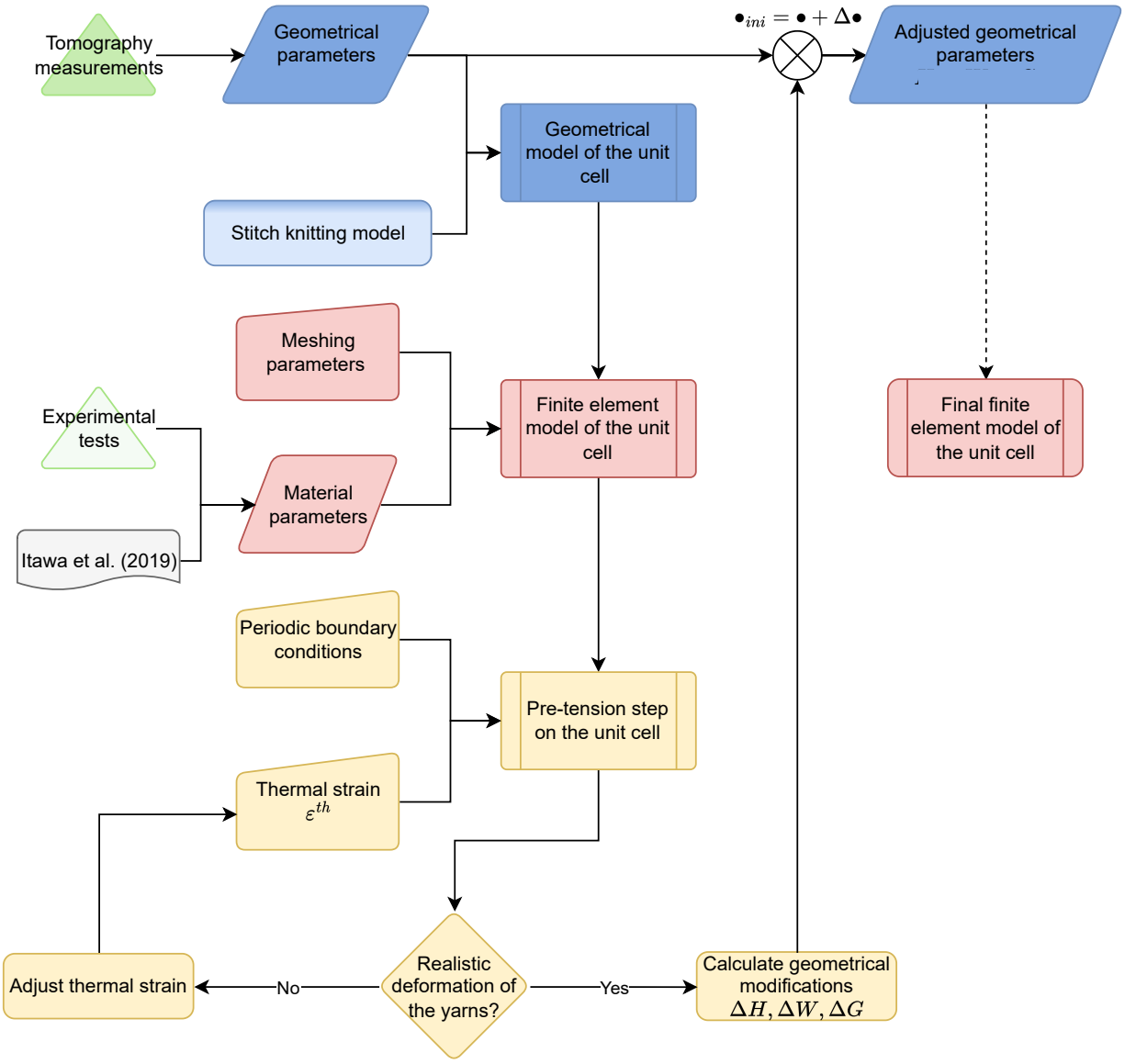

Fig. 2.28: Flow chart of FE mesoscopic modeling

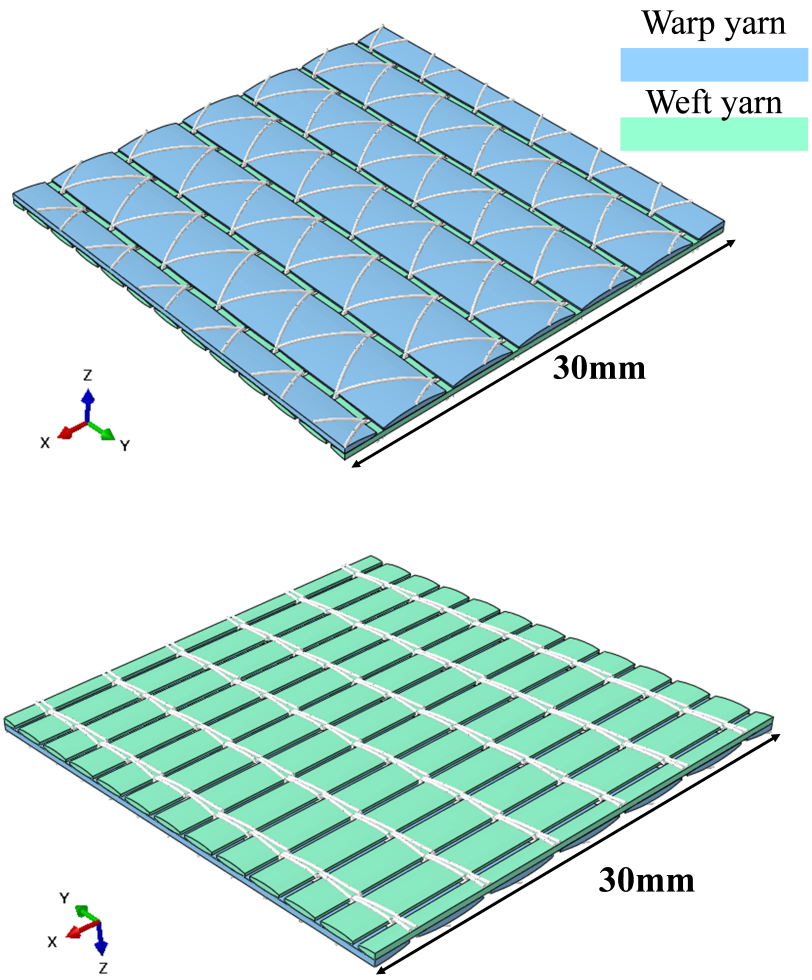

Fig. 2.29: Finite element model ($30 \times 30mm^2$) of Bi-axial NCF after pretension of stitch

2.6 Summary of Chapter 2

This chapter introduces a novel mesoscopic modeling approach for a biaxial NCF, consisting of two unidirectional fiber yarn layers with a tricot stitching pattern. The dimensions of carbon fiber yarns are determined using X-ray tomography, and the stitch model is expressed through a series of equations by dividing it into segments. The Matlab script allows for convenient adjustment of stitch geometry and yarn section, facilitating analysis of different stitching patterns in future studies.

The material model parameters for fiber rovings and stitching at the meso level are identified through experimental tests. The elongation, compaction, and shear behavior of each fiber yarn are represented by a hyperelastic law, and its bending behavior is incorporated using an additional embedded beam element. The stitch is modeled using a general section thermo expansion element, enabling decoupling of its tension and bending behavior, as well as modeling the interaction between fiber yarns and stitches through a novel pretension step.

In the next chapter, this 3D model will be validated to demonstrate its potential for simulating defects that occur at the meso scale, such as fiber bending and gaping and

show that it provides the opportunity for virtual analysis and material characterization.

CHAPTER 3

Validation of the mesoscopic model

The objective of this chapter is to validate the proposed mesoscopic model before utilizing it for larger-scale modeling. The validation process also aims to ascertain the accuracy of the model. To achieve this, an in-plane shear simulation was conducted on the unit cell, as well as on a bias-extension test sample. The deformed geometry and overall forces were then compared with the experimental picture frame test (PFT) and bias-extension test (BET) results, serving as a validation for this mesoscopic model. The model demonstrates its capability to conduct virtual material tests and identify local defects.

Contents

3.1 Observation from experiments

Various experimental tests are available and commonly utilized to validate numerical models. A biaxial tensile test is often used to validate the elongation behavior on woven fabric. In this test, two bars clamp the warp and weft yarns of the fabric individually, as depicted in Figure 3.1a [86, 87, 88]. Additionally, a compaction test is commonly employed to validate the compaction behavior, as shown in Figure 3.1b. However, in the case of NCFs, where the fiber yarns are straight without any undulations, the differences between tests conducted on fabrics and on single yarns are minimal. And these tests are insufficient to validate the model since the stitch structure has less impact.

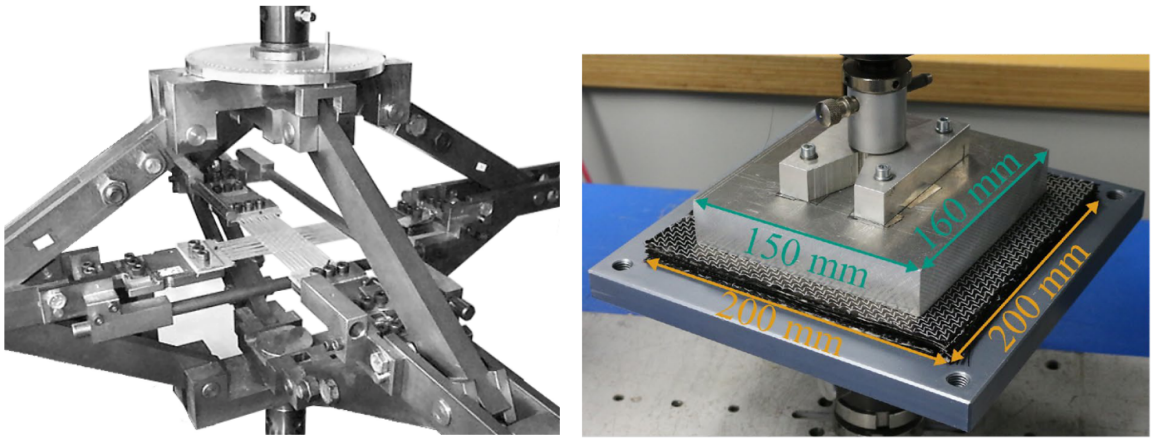

(a) (b)

Fig. 3.1: Experimental test to validate elongation behavior (a) Biaxial tension test [87] and compaction behavior (b) Compaction test [89]

Hence, we introduce the in plane shear experimental tests to validate the mesoscopic NCF model. In-plane shear deformation occurs when the weft and warp yarns rotate to a shear angle γ. Different stitch structures result in unique in-plane shear behaviors in NCFs due to the additional intra-ply stitches that limit the relative rotation of the yarns. Biaxial NCFs typically consist of two yarns oriented at $\pm 45°$ or $0°/90°$, and they are assembled using either tricot or chain stitches. Previous findings demonstrate that $\pm 45°$ tricot stitch biaxial NCFs exhibit positive and negative shear under different loading directions during shear deformation [90, 91, 92]. This corresponds to tension or compression of the stitches, respectively, as illustrated in Figure 3.2. When the reinforcement shears positively, the stress in traction of the stitching yarn requires a high shearing force while for a negative angle the stitch is stressed in compression and the force necessary for the deformation is low.

Conversely, the $0°/90°$ bi-axial NCF possesses a symmetric stitching structure, resulting in one stitch segment being under tension while the other remains loose. Consequently, it maintains a consistent force response regardless of the loading orientation ($+45°$ or $-45°$). Two experimental tests are mainly used by the researchers to analyse the in-plane shear behavior: the Picture frame test and the Bias-extension test [35]. All these tests are implemented on the electromechanical traction machine Lloyd $1\,\mathrm{kN}$.

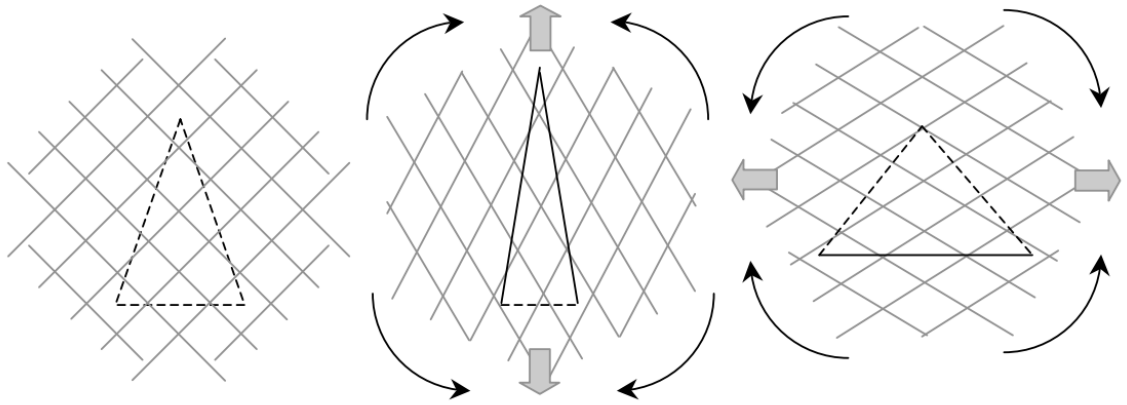

Fig. 3.2: $\pm 45°$ NCFs stitch segments under tension (solid black lines), compression (dashed black lines) during positive and negative pure shear loading (fibre directions shown as grey lines) [92]

3.1.1 Picture frame test

In the Picture Frame test, the NCF samples were cut into a cross shape (as shown in Figure 3.3a). The side length of the middle zone is $110\,\mathrm{mm}$ (fabric length L_{fabric}). Three holes are punched on each arm of the cross to attach it to a hinged frame consisting of four rigid bars with a length of $120\,\mathrm{mm}$ (frame length L_{frame}). The center square of non-crimp fabric was then embedded into the frame and it needed to ensure that the weft and warp fiber yarns remain parallel to the edge. The initial shear angle is assumed to be 0 when the weft and warp yarn are perpendicular to each other. The sample and the frame undergo a vertical machine displacement d of the top point, as shown in the schematic (Figure 3.3b).

A pure shear deformation is considered in the center square zone and findings indicate a negligible difference between the theoretical shear angle and the local shear angle [35, 93]. Thus, the shear angle γ is expressed by the kinematic equation:

$$\gamma = 90° - 2\arccos\left(\frac{\sqrt{2}L_{frame} + d}{2L_{frame}}\right) \tag{3.1}$$

This equation provided by [35] is the average value across the entire specimen, and the actual shear angle may vary at different points on the fabric.

The net force F_s is obtained by subtracting an empty frame force F_{frame} from the tested machine force F_m which is recorded by the load sensor. The shear force can then be calculated using the net force and the shear angle from the following equation:

$$F_s = \frac{F_m - F_{frame}}{2\cos\left(45 - \frac{\gamma}{2}\right)} \tag{3.2}$$

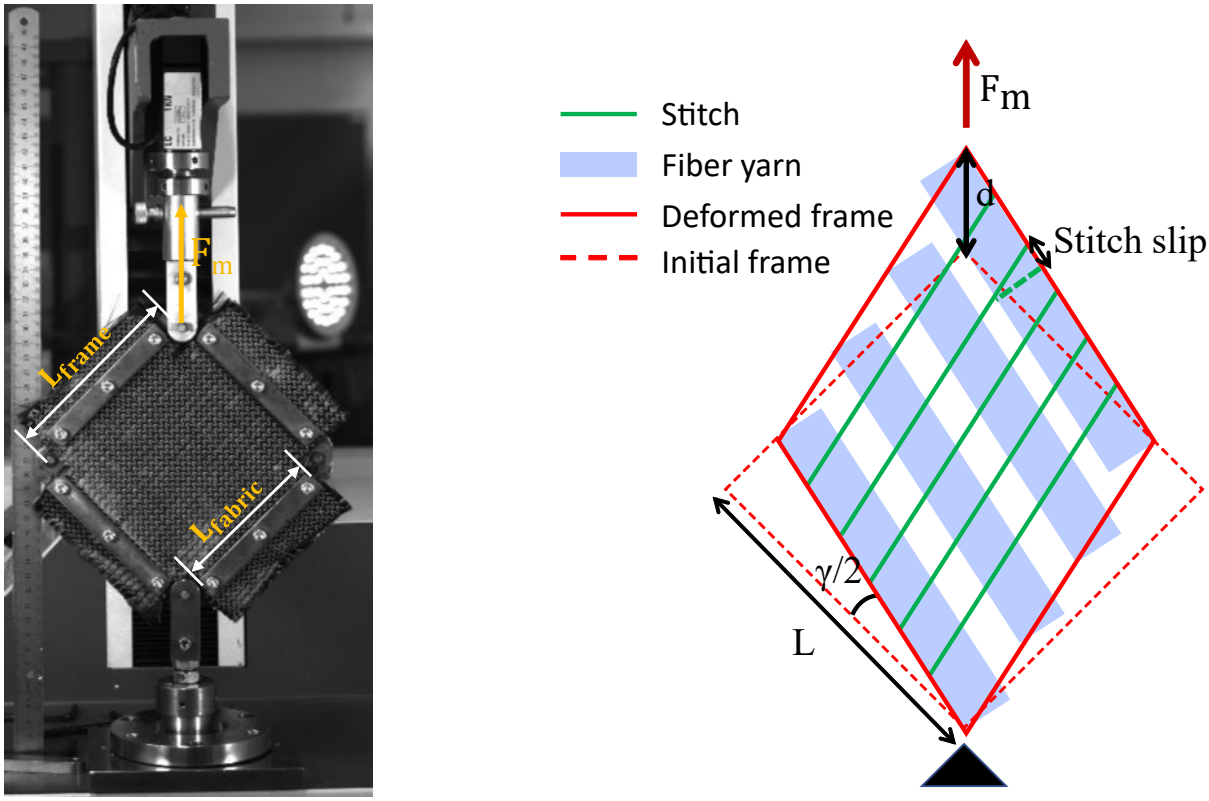

(a) (b)

Fig. 3.3: Picture Frame Test on bi-axial NCF (a) Initial configuration on experiments (b) schematic representation of bi-axial NCF inside the PFT.

To facilitate the comparison of the results obtained from this test with other shear stiffness quantification, whether attained through different tests or derived from numerical simulations, the net force exerted on the framework is not adequate. It becomes imperative to establish a parameter that reflects shear behavior, independent of the specific measurement instrument or sample dimensions. In [35, 94], a normalized shear force F_{nor} is calculated based on an energy method using the following equations:

$$F_{nor} = F_s \cdot \frac{L_{frame}}{L_{fabric}^2} \tag{3.3}$$

3.1.2 Bias-extension test

The bias-extension test is simpler to preform since it eliminates the potential for spurious tension occurring in the PFT [95]. In this test, biaxial NCF samples with dimensions of $80\,\mathrm{mm}$ in width and $240\,\mathrm{mm}$ in length were clamped at both ends and positioned such that the weft and warp yarns were initially oriented at $\pm 45°$ relative to the loading direction, as depicted in Figure 3.4a.. Subsequently, the samples underwent axial stretching at a constant rate of $25\,\mathrm{mm/min}$.

A standard bias-extension test assumes that:

- the fiber yarns are inextensible

- no sliding happens between the weft and warp yarns

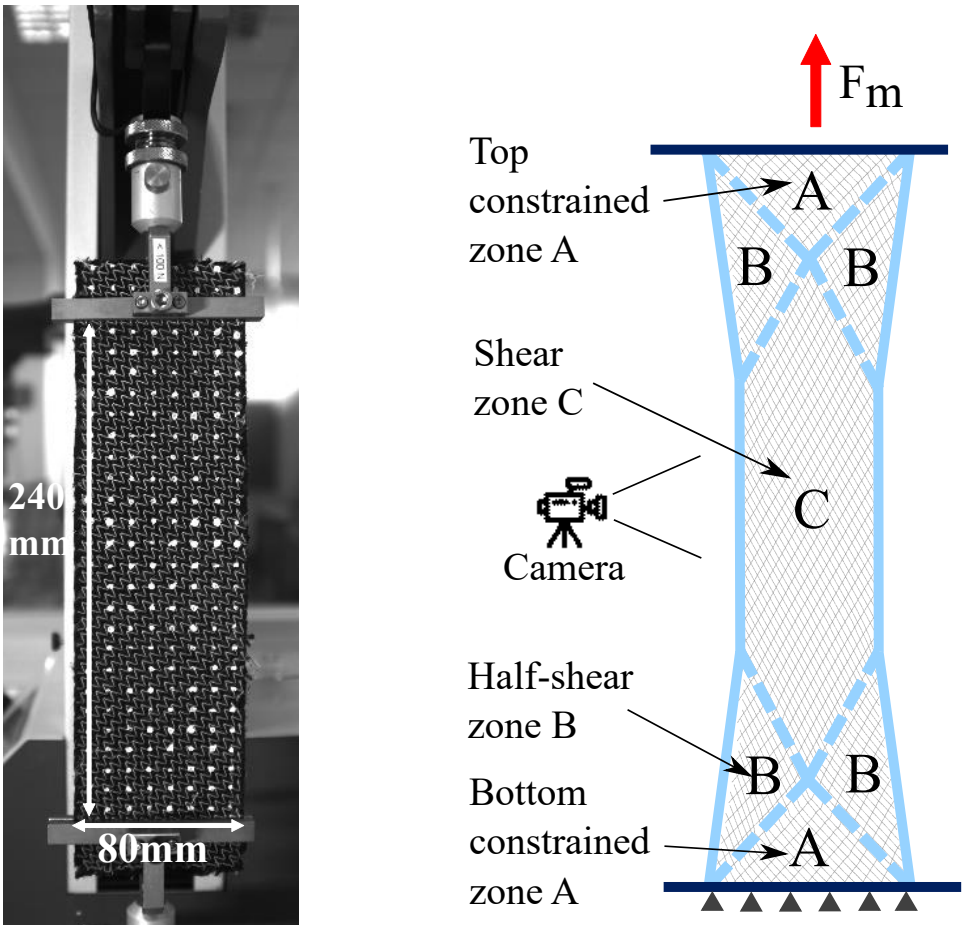

(a) (b)

Fig. 3.4: Bias Extension Test (a) Initial configuration with sample dimensions $240\,\mathrm{mm} \times 80\,\mathrm{mm}$ (b) Theoretical solution of BET with zones A (no-shear), B (half shear) and C (maximum shear).

Thus, after stretching the fabric from L to $L + d$ (L is the sample length and d is the machine displacement), three zone can be observed on the deformed shape as shown in Figure 3.4b: an undeformed zone A due to the clamp of one end of fibre yarn, a shear zone C which has free ends and a half shear zone B. Two relations are necessary to analyze the results which are the kinematic relation that relates the in-plane shear angle to the extension of the specimen and a relation between the shear force in the fabric and the measured machine force. The shear angle of the middle shear zone C can be calculated by the kinematic relation between the shear angle γ and the machine displacement d:

$$\gamma = \frac{\pi}{2} - 2\cos^{-1}\left(\frac{D+d}{\sqrt{2}D}\right) \tag{3.4}$$

where $D = H - W$ represents the length of the central shear zone C, H and W is the height and width of the sample.

The measured load F_m on the tensile machine is a global force of the specimen, which is not sufficient to compare with different specimens or devices or numerical results. Thus, a normalized shear force F_{sh} is calculated in BET using Equation 3.5, which comes from the virtual energy theorem applied to a three zone sample [35]. The calculation was done with the angle γ directly measured on the NCF. Note that Equation 3.5 remains valid only in the case where zone A exhibits no shearing, and zone B exhibits half shear of zone C.

$$\begin{aligned} F_{sh}(\gamma) = & \frac{1}{(2H-3W)\cos\gamma} \\ & \times \Big((\frac{H}{W}-1) \cdot F_m \cdot (\cos\frac{\gamma}{2} - \sin\frac{\gamma}{2}) \\ & -W \cdot F_{sh}(\frac{\gamma}{2}) \cos\frac{\gamma}{2} \Big) \end{aligned} \tag{3.5}$$

Since the shear force at the half shear zone B is an unknown value in Equation 3.5, an iterative algorithm was developed in MATLAB to calculate the normalised shear force. The flowchart is shown in 3.5. We assume that at a very small shear angle (less than 10^{-8}), the shear force is $0\,\mathrm{N}$.

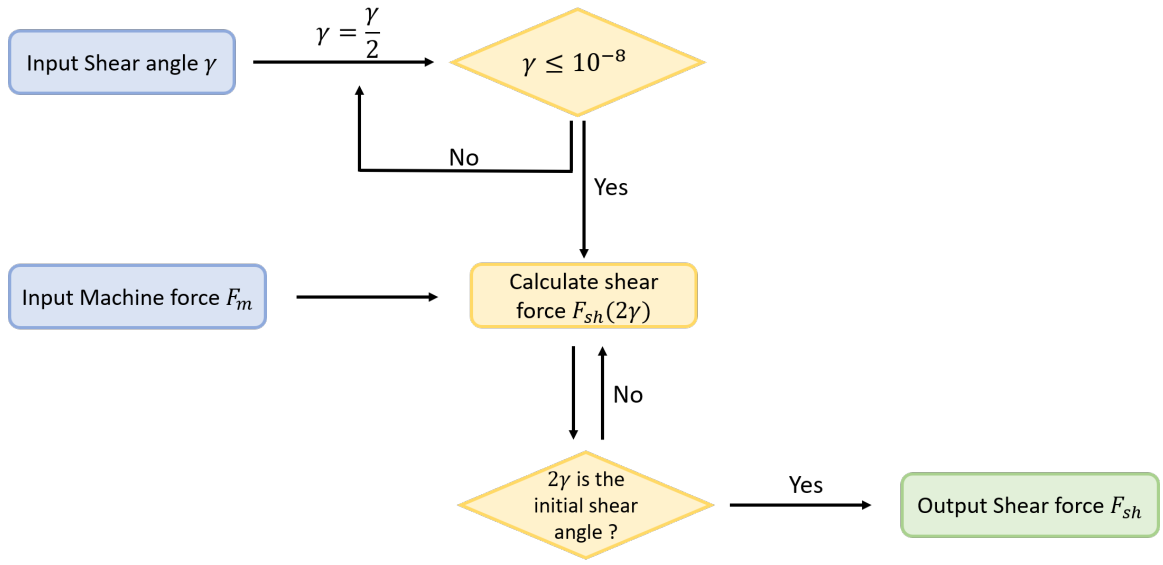

Fig. 3.5: Flowchart of the iterative algorithm for calculating BET shear force

Zoom-in view

One major advantage of the bias-extension test is the freedom of the yarn extremities at the center shear zone C, resulting in minimal or no tension in the yarns. However, this test holds the reinforcement in a relatively weaker manner, which can lead to slippage between the warp and weft yarns, especially at larger shear angles. Compared to woven fabric, NCFs experience increased sliding between the fiber yarn, stitch, and the two plies. Prior research findings, such as those from [39], indicate that the true shear angle is below 5° when the shear angle is less than 30°, but it increases beyond this threshold. Consequently,

relying solely on kinematic equations is insufficient for accurately calculating the shear angle. Instead, the orientation of the weft and warp yarns should be directly measured. The shear angle in Zone C can be determined by analyzing the timed images captured during the test [96]. Furthermore, it is crucial to accurately measure the gap between the fiber yarns throughout the entire deformation process. To detect the development of gap is another aspect of interest and can be used to validate the numerical model. Thus, the zoom-in view is required.

To obtain a clearer perspective of the center zone C, a closer camera is positioned for a zoom-in view. The camera captures images at intervals of $2\,\mathrm{mm}$ of machine displacement. As shown in Figure 3.6, the fiber yarns and the gaps between them can be observed clearly. Several yarns were marked in white dotted line and their edges were subsequently tracked in software Fiji. Five yarns were followed and ten positions are measured to get the average value. The rotation of the warp yarn is determined by subtracting its initial angle from the current warp yarn angle.

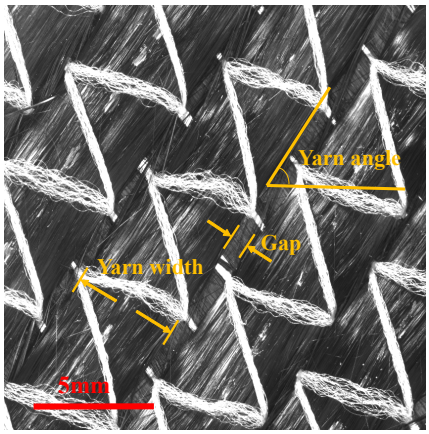

Fig. 3.6: Zoom-in view of the zone C in BET test (Machine displacement 20mm): Measurement of gaps, widths and angles on the yarns marked with white dots

3.2 Numerical simulation on unit cell

Beginning the numerical studies with a unit cell model is a recommended approach due to the reduced computational effort involved (memory space, calculation time...). We make the assumption that the undistorted configuration of the NCF exhibits periodicity, meaning that the complete reinforcement can be reconstructed by repeating a pattern, referred to as a unit cell. While the unit cell may not be unique, it serves as a representative volume element (RVE) for the material, representing the behavior of the homogenized equivalent material. Under a uniform transformation, each unit cell undergoes identical deformation, resulting in the macroscopic behavior of the reinforcement being the sum of all individual unit cell behaviors. Consequently, it becomes possible to compare the behavior of an isolated unit cell with the macroscopic behavior of the reinforcement. This comparative analysis will be performed later to identify and validate the constitutive law. Nevertheless,

we first establish the equations ensuring periodicity and boundary conditions, as well as select an appropriate unit cell model.

3.2.1 Choice of a unit cell model

The choice of the unit cell is not unique. Figure 3.7 illustrates two type of unit cell models. The type 1 model consists of two entire warp yarns and four weft yarns. It can be observed that at the boundary, the stitch loop connection is broken, causing some of the stitches to detach from the overall model. Moreover, most of the boundary zones have no material nodes for us to implement the equations, making it difficult to ensure the periodicities. For the type 2 model, the boundary is located at the midpoint of the yarn, eliminating the zone without material points. Previous research has demonstrated that the use of a type 1 model does not present any issues in biaxial tension or compression [97]. But in the case of in-plane shear simulation, the type 2 model is preferred.

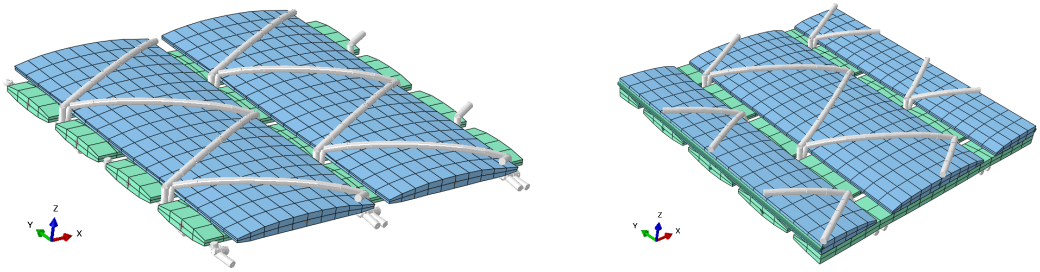

(a) (b)

Fig. 3.7: Two types of unit cell model (a) type 1 (b) type 2

3.2.2 Periodicities and boundary conditions

To ensure the periodicities of the structure, it is necessary to impose the boundary conditions on the unit cell. We use the periodicity of the displacement field which leads then to the writing of boundary conditions in displacement [98]. Figure 3.8 illustrates a displacement field $\underline{\phi}(\underline{X})$ which transforms the structure from its initial to deformed state.

The displacement field can be separated into two components: the macroscopic displacement field $\underline{\phi}_m(\underline{X})$, which is known and serves as the input for the simulation, and the periodic local displacement $\underline{w}(\underline{X})$, which is unknown and depends on the mechanical properties, causing the unit cell's deformed geometry to change [22, 97]. This superposition is expressed by the following equation:

$$\underline{\phi}(\underline{X}) = \underline{\phi}_m(\underline{X}) + \underline{w}(\underline{X}) \tag{3.6}$$

In order to ensure periodicity it is necessary to make sure that the local displacements of two opposite sides are equal. For example, X^+ and X^- are two opposite set of nodes

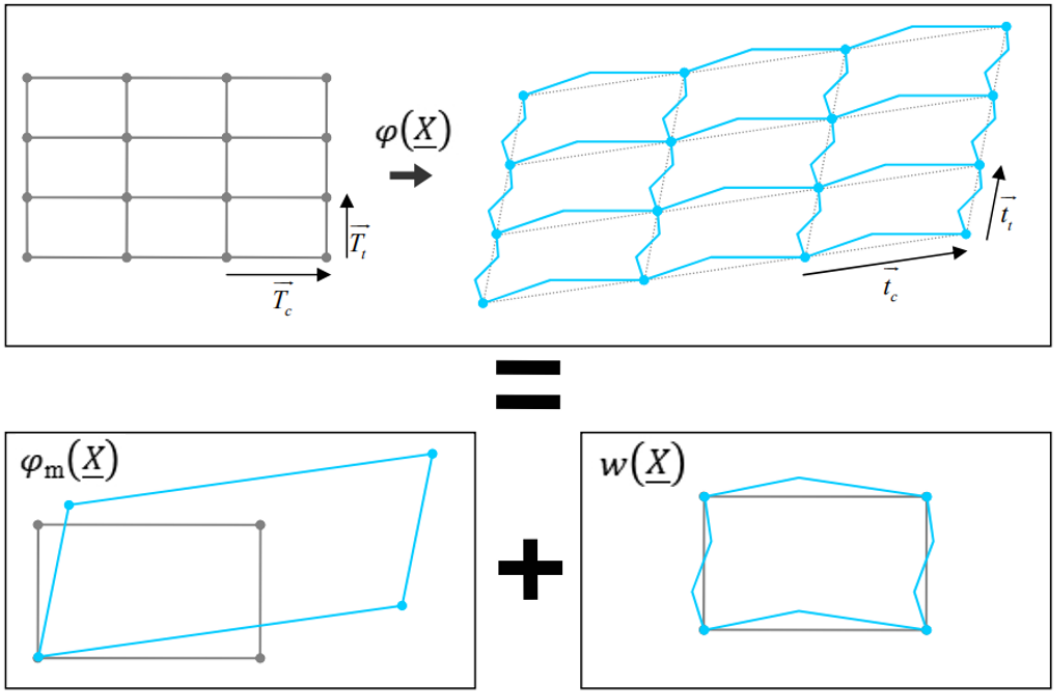

Fig. 3.8: Global deformation and local deformations of the elementary mesh making it possible to guarantee the conditions of periodicity of the field of displacement of the reinforcement subjected to a homogeneous global transformation [77]

showed in Figure 3.9. In order to fulfill periodicity, Equation 3.7 ensures that the local displacements of two opposite sides, $\underline{X}^+$ and $\underline{X}^-$, are equal.

$$\underline{w}(\underline{X}^+) = \underline{w}(\underline{X}^-) \tag{3.7}$$

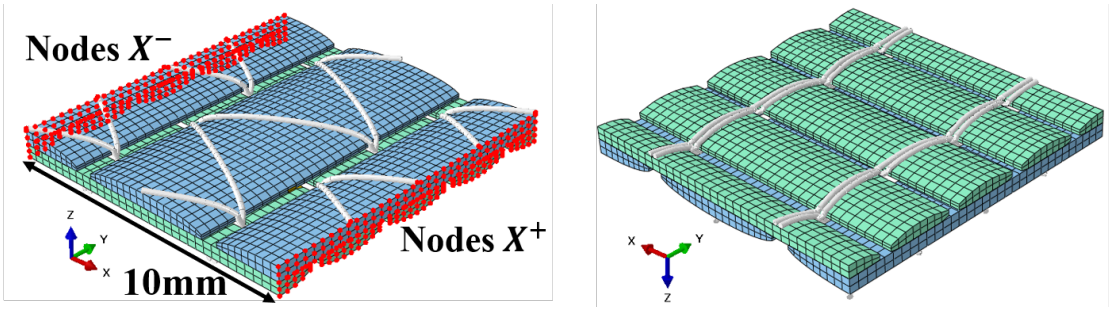

(a) (b)

Fig. 3.9: Finite element representative unit cell of Bi-axial NCF (a) upper side, warp yarn with zig-zag stitch (b) lower side, weft yarn with looped stitch.

Thus, by subtracting the displacement field of nodes on the $\mathbf{X}^-$ side from the displacement field of nodes on the $\mathbf{X}^+$ side, the unknown value of the local displacement field can be eliminated. Then the boundary conditions are applied on each material node pairs

of opposite sides by the following equations:

$$\underline{\phi}(\underline{X}^+) - \underline{\phi}(\underline{X}^-) = \underline{\phi}_m(\underline{X}^+) - \underline{\phi}_m(\underline{X}^-) \tag{3.8}$$

In ABAQUS, the keyword $*Equation$ enables us to define the linear multi point constraints (MPC). It is written in the following format:

$$A_1 u_i^P + A_2 u_j^Q + ... + A_n u_k^R = 0 \tag{3.9}$$

where u_i^P is a nodal variable at node P, degree of freedom i; and the A_n are coefficients that define the relative motion of the nodes.

In the ABAQUS Input file , one equation should be written in three lines, where the first line is the keyword $*Equation$, the second line is the number of terms in the equation and the third line includes all the parameters used in this equation.

In our case for the X axis boundary, The displacement of two corner nodes(rpr and rpl) needs to be defined, representing the macroscopic displacement field and will drive the deformation of the model. The Equation 3.8 can then be expressed as:

$$u_i^{X^+} - u_i^{X^-} - u_i^{rpr} + u_i^{rpl} = 0, (i = 1, 2, 3) \tag{3.10}$$

The equation can also be applied to the Y-axis boundary by making changes to the opposite nodes set Y^+ and Y^-, as well as the corner nodes rpt and rpb:

$$u_i^{Y^+} - u_i^{Y^-} - u_i^{rpt} + u_i^{rpb} = 0, (i = 1, 2, 3) \tag{3.11}$$

3.2.3 Unit cell in-plane shear simulation

In the in-plane shear simulation, a macroscopic displacement is applied to the two corners of the model in a direction that is $45°$ to the orientation of the fibers. The job is launched in ABAQUS Explicit solver with two CPU cores. The computation takes $16\,\mathrm{h}$. The deformed configurations of warp and weft views are shown in Figure 3.10. On the “zigzag" stitch pattern, it can be observed that one segment of stitch is stretched and the other one is compressed. The schema and kinematic equation utilized in the Picture Frame test can be applied to the analysis of pure shear deformation in this unit cell with considering that the length of the frame is equivalent to the length of the fabric. The shear force on the unit cell model is also normalized by Equation 3.3 and then it is used to compare with the experimental shear force.

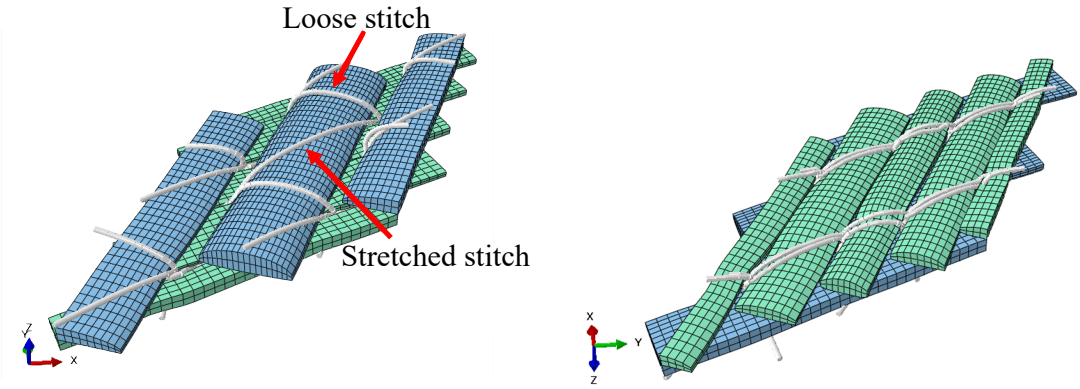

(a) (b)

Fig. 3.10: Deformed configuration of unit-cell under pure shear test (a) upper side, warp yarn with zig-zag stitch (b) lower side, weft yarn with looped stitch.

3.3 Numerical simulation of BET

Due to the imposition of stringent constraints, the unit cell model more closely resembles a Picture Frame test. Displacement boundary conditions are applied at the intersection of warp and weft yarns (position of two half yarn). The actual shear angle consistently matches the theoretical angle calculated using kinematic equations. In order to observe the sliding between weft and warp yarns, a simulation of BET is required. Additionally, the performance of the model need to be illustrated on a larger scale.

3.3.1 Model for BET simulation

As discussed in Chapter 3, the geometrical model of NCF is generated directly from a MATLAB script by defining the number of weft and warp yarns. Consequently, the model takes on a square or rectangular shape with weft and warp yarns oriented at $0°/90°$. To create the model to simulate the BET, it is necessary to automatically create a rectangle model with weft and warp yarn oriented $\pm 45°$. This involves rotating the model by $45°$ and then cutting it into a rectangular shape. Python script is utilized to select the desired model zone and perform the automated cutting process, as illustrated in Figure 3.11. The following parameters are defined for this purpose:

- Coordinate of the begin point
- Rectangle size
- Fiber yarn orientation
- Offset stitching

The size of the model after cutting is $240\,\mathrm{mm} \times 80\,\mathrm{mm}$ with 47,941 solid elements for fiber yarns and 51,249 beam elements for stitches as shown in Figure 3.12. The offset stitching is set as 0.

All the nodes on the left side are clamped and fixed, and on the right side are stretched. The computation was launched on the Cluster that consolidates independent computers

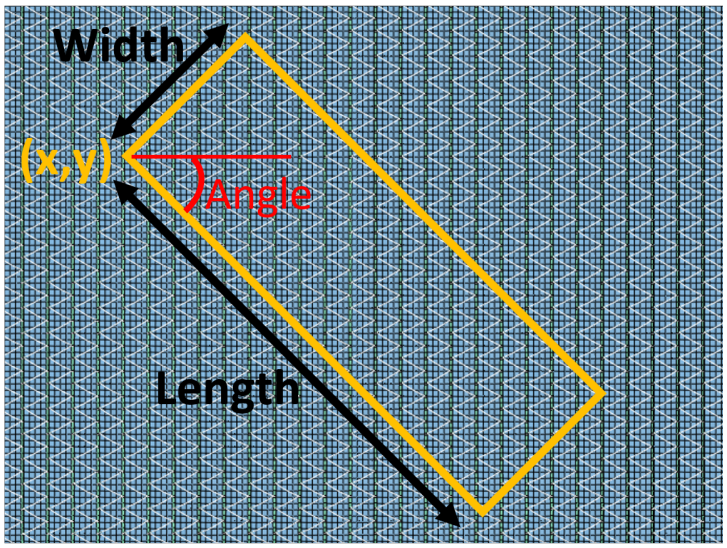

Fig. 3.11: Automatically cutting a BET model through a Python script

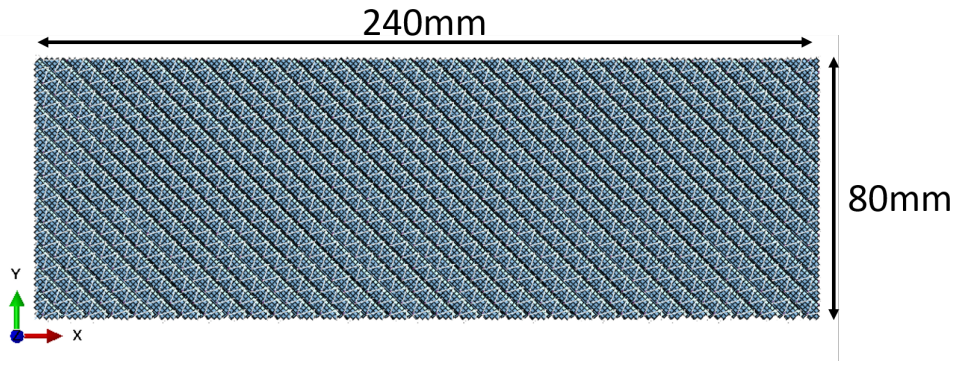

Fig. 3.12: BET model for numerical analysis

with a global management to utilize abundant resources. It took $80\,\mathrm{h}$ with 20 CPU cores and 64GB RAM.

3.3.2 Simulation results

The deformed configurations of the weft and warp yarns, after being stretched by $45\,\mathrm{mm}$, are depicted in Figure 3.13 (a) and (b). For comparison, the corresponding experimental test's warp view is presented in Figure 3.13. At the edge of the half shear zone B, inter-ply sliding can be observed, as shown in Figure 3.13 (b). This phenomenon was also observed in the experimental results (see Figure 3.13d) where unraveling of stitches occurred. Moreover, a zoom-in view of the center shear zone C (see Figure 3.13e) help us to observe the tensioned stitch and the compressed stitch which is in good agreement with the experimental results shown in Figure 3.13f.

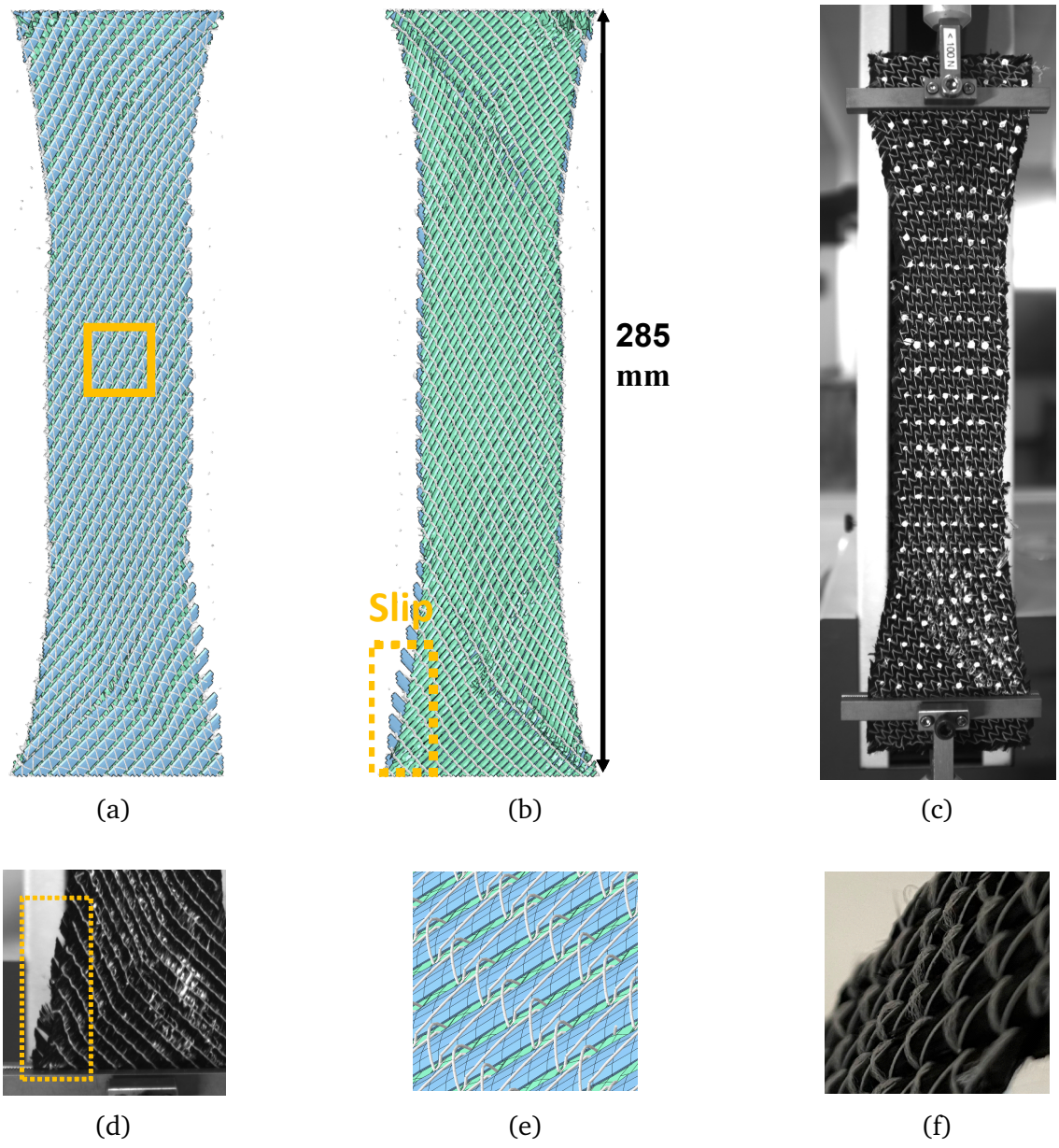

Fig. 3.13: Results of BET: Deformed configuration of simulated (a, wrap yarn, and b, weft yarn) and experimental BET (c, wrap yarn); (d) zoom-in view of the experimental edge revealing the occurrence of slips; zoom-in view of the simulated (e) and experimental (f) central shear zones with the presence of both under-tension and bent stitches.

Visualization of shear angle at mesoscopic scale

The macroscopic simulation allows for the direct visualization of the shear angle from the output file, as each finite element contains both directions of fiber yarns. However, in the mesoscopic model, the elements on the two plies are generated separately. As shown in Figure 3.14, the shear angle can be calculated by comparing the fiber orientation of elements on part 1 of the warp yarn to that of its corresponding elements on part 2 of the weft yarn. It is difficult to directly visualize the shear angles on the elements in the Abaqus output results, thus a post-analysis is necessary.

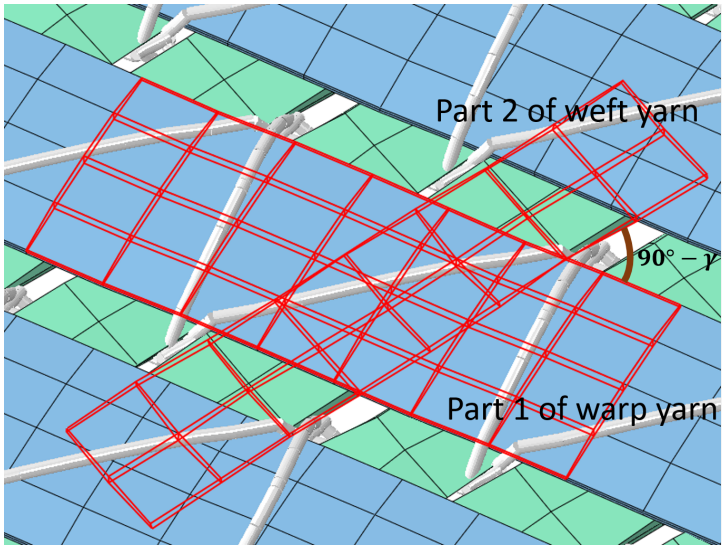

Fig. 3.14: BET model for numerical analysis

Since embedded beam elements in the center of the yarn can be used to represent the fiber orientation, extraction of data from solid elements to 2-node beams will simplify the process. The coordinates of the nodes and connection order of the elements of the embedded beam elements are then extracted and stored in Matlab. The coordinate in the yarn's thickness direction is disregarded since it does not affect the calculation of the shear angle. Figure 3.15a illustrates the orientation of the warp yarn (blue) and the weft yarn (red) in the BET simulation results. Each element in the warp yarn direction is then compared with the corresponding element in the weft yarn to identify intersections. Then the two elements will also be used to calculate the shear angle and the data is saved in this intersection. The MATLAB code utilizes the "Delaunay" function to create a 2D Delaunay triangulation of the intersections, which allows for the visualization of the shear angle in the bias-extension test, as depicted in Figure 3.15b. The three distinct zones can be easily distinguished.

The comparison of shear angle is shown in Figure 3.16

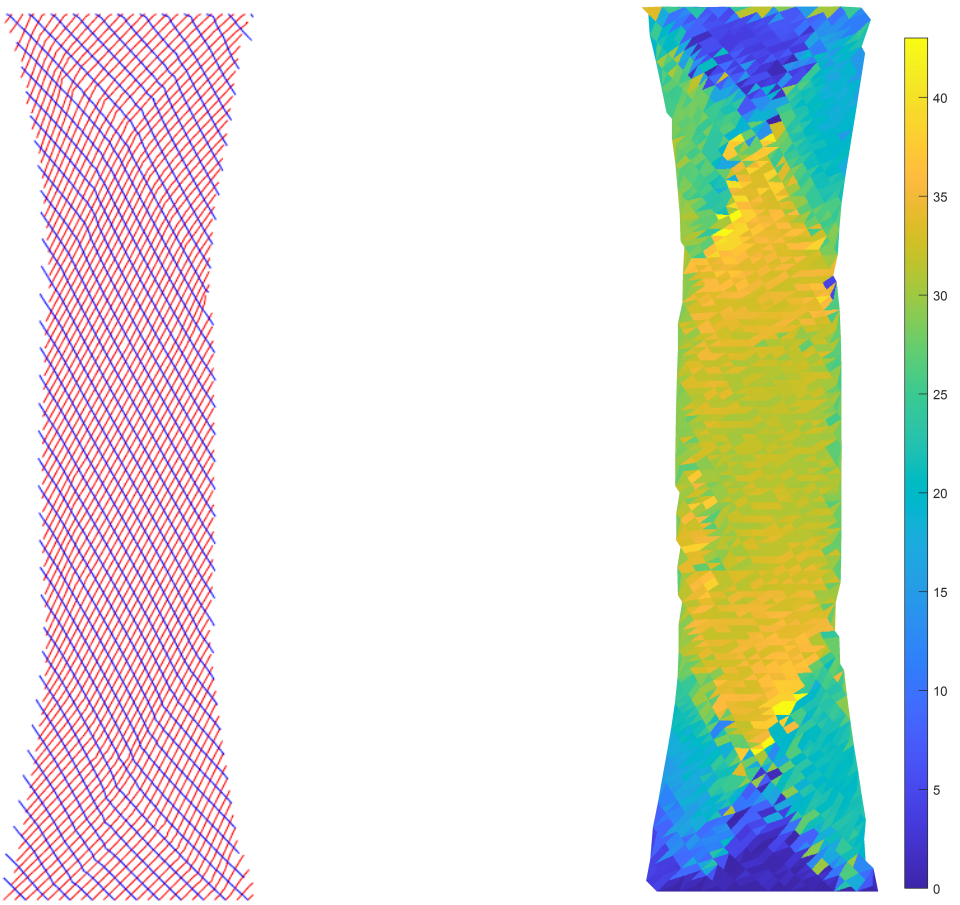

(a) (b)

Fig. 3.15: Calculation of effective shear angle in FEM results; (a) Yarn orientation of weft yarn (red) warp yarn (blue); (b) Shear angle between the two directions, in degree.

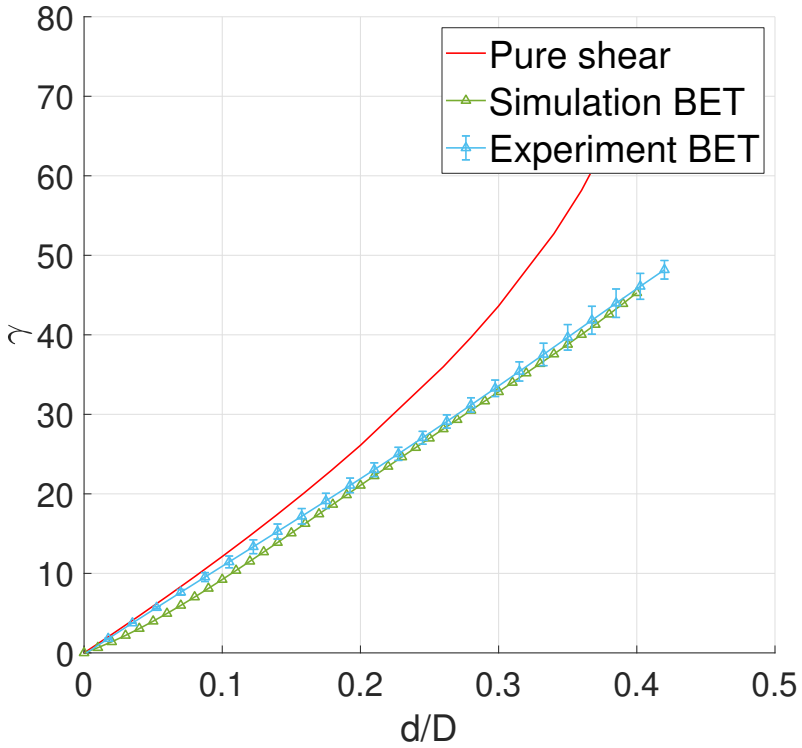

Fig. 3.16: Comparison of experimental and simulated effective shear angles in BET with theoretical shear angle in pure shear tests, without slippage.

3.4 Comparison and discussion

The comparison of experimental results and numerical simulation is conducted through a geometrical validation and a mechanical validation. The geometrical validation shows the ability of this model to detect local defects and the mechanical validation shows the potential of this model to conduct virtual material characterization.

3.4.1 Geometrical validation

During the forming process, the development of gaps and changes in the width of the fiber yarn are two primary factors that contribute to the formation of future resin-rich areas. In previous research, there exists no mesoscopic model of NCF that was developed for the detection of local defects. Such a model necessitates accurate geometric parameters and precise modeling of the stitch knitting pattern, along with a well-defined interaction between the yarn and stitch. Before conducting the forming simulations on our mesoscopic model, it is necessary to validate the local deformation by comparing the numerical results with experimental findings. In the simulation results, the width of the yarn is measured as the distance between two nodes on both the right and left sides, assuming no longitudinal shear deformation occurs in a single yarn. Some slight distortion of yarn occurs due to stitch tension, so the average value with an associated error bar is calculated and depicted in Figure 3.17a. The gap is defined as the distance between the left yarn node and the borderline of the right yarn, and the measurement results are displayed in Figure 3.17b. Since the gap and width values from experimental tests are obtained from cutting samples, while the geometric parameters of the numerical simulation are derived from tomography measurements, there may be slight differences in the initial values. Therefore, all values are normalized by their initial lengths for comparison purposes.

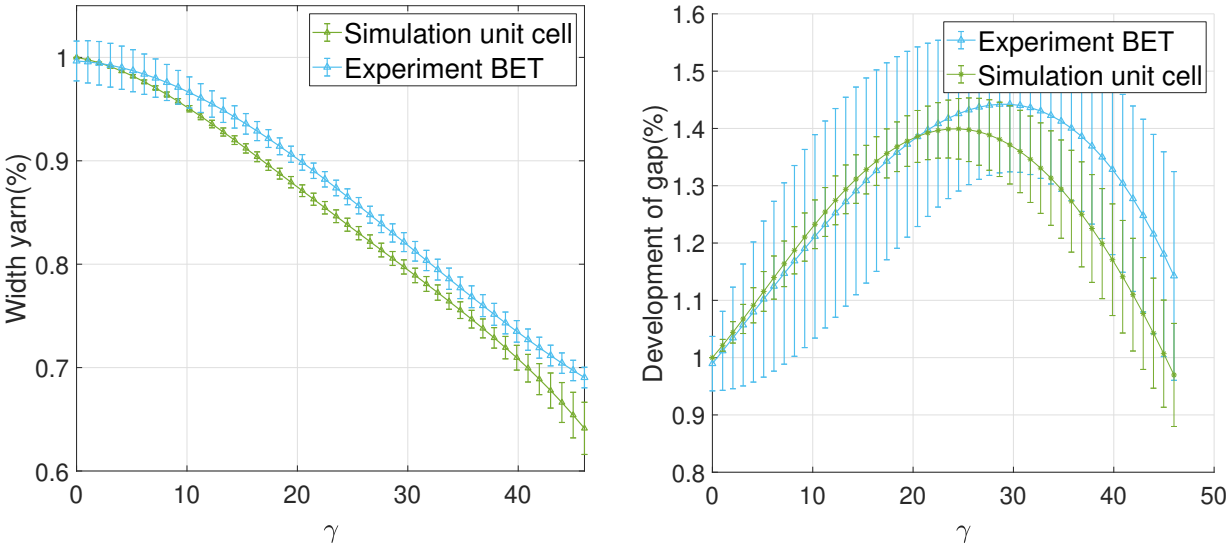

(a) (b)

Fig. 3.17: Comparison between simulation results and experimental tests: (a) Width of yarn vs. shear angle; (b) Development of gap vs. shear angle;

For woven fabrics, the shear curve exhibits distinct phases, as illustrated in Figure 3.18. In the initial phase, the mechanisms involved are the friction between the weft and warp yarns and the rotational forces at the crossing points [99]. The second phase occurs when the fiber yarns rotate to a critical blocking angle, causing adjacent fiber yarns to come into contact. This contact results in lateral compaction, which can be observed through mesoscopic imaging [100]. Subsequently, during the third phase, the force required for shearing experiences a substantial increase and may lead to the formation of wrinkles [101].

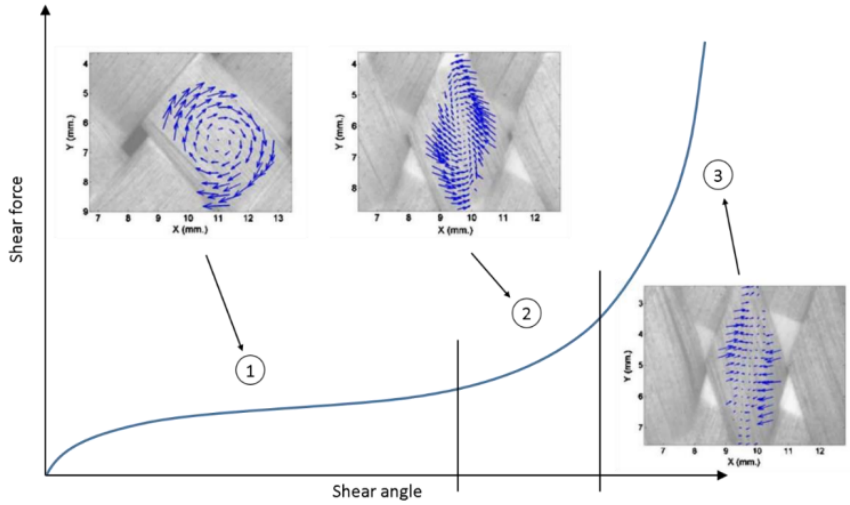

Fig. 3.18: Different phase in the shear curve of PFT on woven fabric [100]

In the case of NCFs, the absence of interlock structure between yarns does not constrain the fibers beyond a certain angle. These reinforcements therefore do not have a blocking angle. A notable observation is that the warp fiber yarn experiences continuous compression by the tensioned stitch, without requiring the contact between adjacent yarns. The gap between the fiber yarn is firstly increasing before $25 - 30°$ shear angle but subsequently decreases until it reaches zero, as shown in Figure 3.19.

In order to validate the accuracy of the measurements in both simulation and experiments, the broadness of the shear zone is compared. Figure 3.20 shows the broadness which can be considered as the sum of the width of yarn and the gap. The theoretical broadness is a known value calculated by the shear zone length L and the shear angle γ as:

$$B = L \cdot cos(\gamma) \tag{3.12}$$

The comparison between the theoretical broadness and the results obtained from experiments and numerical simulations is depicted in Figure 3.21, revealing a strong agreement between them.

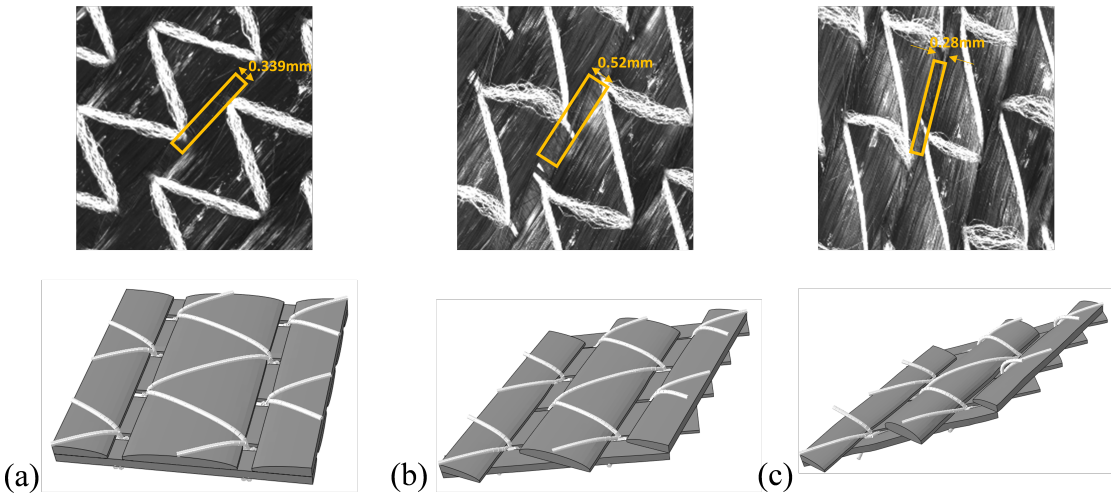

Fig. 3.19: Bias-extension test zoom-in view and unit cell in-plane shear simulation under different shear angle (a) initial configuration (b) $26°$ (c) $52°$

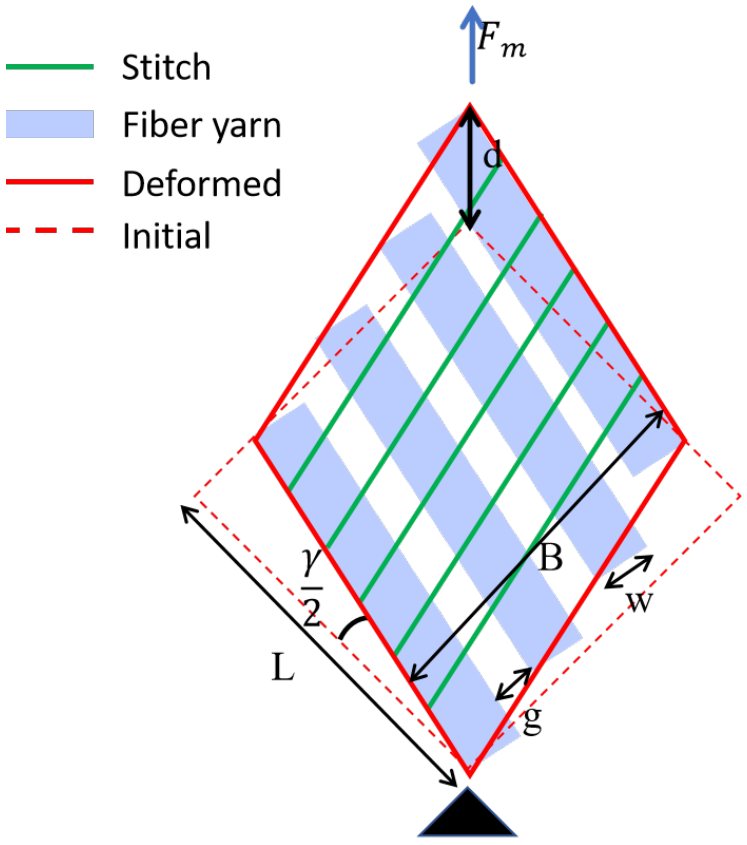

Fig. 3.20: Schematic of validated geometrical parameter: Gap g, width of yarn w and broadness B

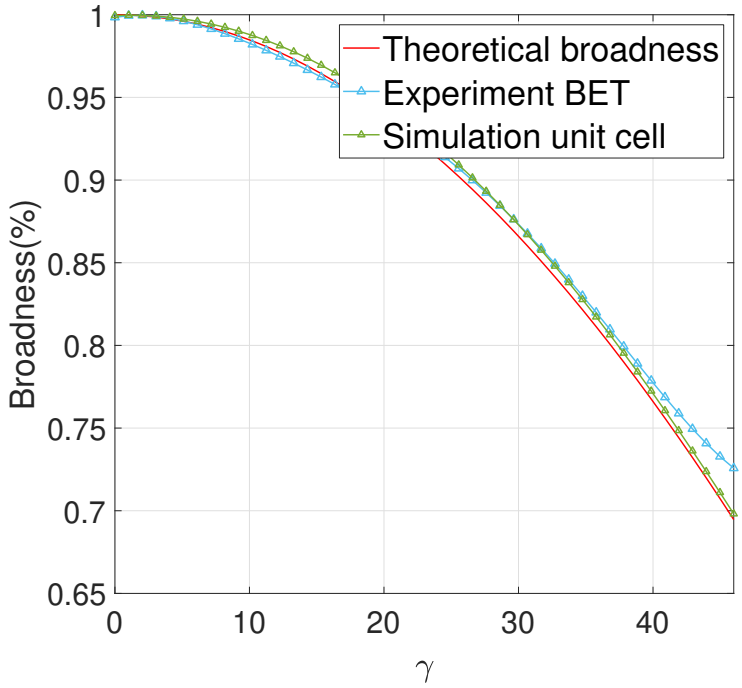

Fig. 3.21: Validation of measurement: Broadness vs. shear angle

3.4.2 Mechanical validation

The NCFs can be shaped on a double curve surface since the two layers of carbon fabric are linked by the stitches. Achieving this desired shaping involves in-plane shear deformation of the two layers of fiber yarns, taking advantage of the yarn's inextensibility. Hence, it is crucial to comprehend the in-plane shear behavior of NCFs prior to conducting macroscopic simulations for material forming tests, which require a larger number of experimental tests. By validating the accuracy of this modeling approach in characterizing the mechanical behavior, significant reduction in experimental efforts can be attained. In regards to in-plane shear deformation, the normalized shear forces of PFT and unit cell simulations are calculated using Equation 3.3, while those for BET tests and simulations are calculated using Equation **??**. A summary of the results is presented in Figure 3.22, demonstrating excellent agreement.

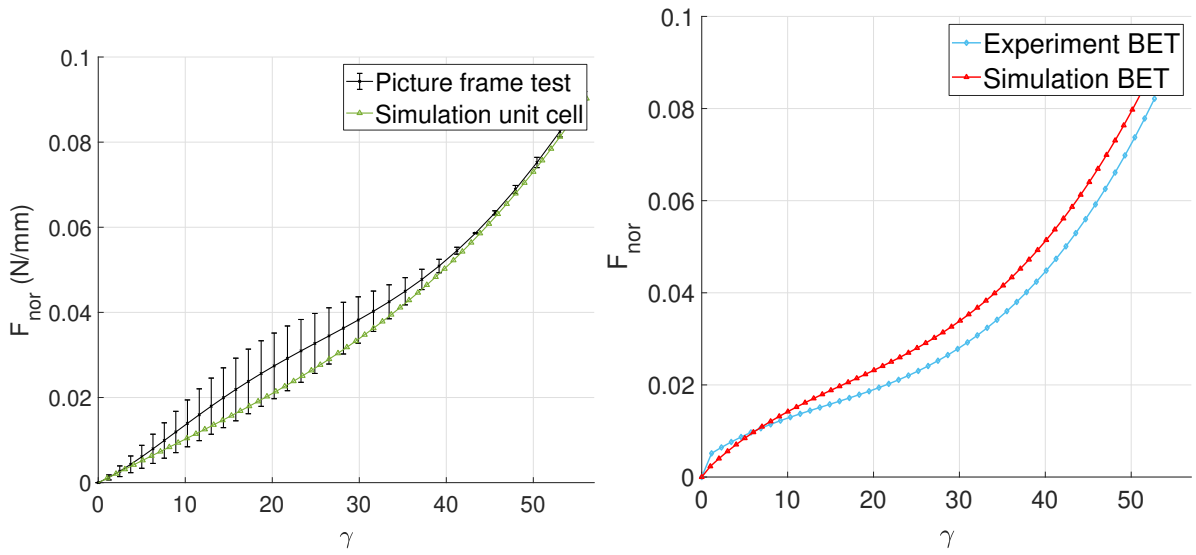

(a) (b)

Fig. 3.22: Normalized shear force vs. shear angle (a) PFT and unit cell modeling (b) BET and BET simulation

3.5 Summary of Chapter 3

In this chapter, the mesoscopic FE model of biaxial NCF is validated through an in-plane shear simulation. The experimental PFT and BET are employed for comparison with the numerical unit cell and BET simulation results. This modeling approach allows for direct visualization of yarn width, gap development, and inter-layer sliding. The excellent agreement between the shear forces obtained from the experimental test and the numerical simulation validates the potential of this model for virtual material testing, thereby significantly reducing reliance on extensive experimental tests.

CHAPTER 4

Numerical and experimental forming analysis of Non-crimp fabric

In this chapter, the experimental and numerical forming tests results of NCFs are presented. A large amount of experimental tests of NCFs were conducted in collaboration between INSA-LaMCoS and KIT-FAST in the AMECOMP project in order to investigate their forming behavior. Different academic punch shapes (Hemisphere, Tetrahedron, Square box), fabric types (Unidirectional NCF, biaxial NCF) and fiber orientations ($0°$, $45°$, $0°/45°$ double layer) were analyzed. The deformation behavior of the fabrics is captured throughout the entire process using a Digital Image Correlation (DIC) strain measurement method. The validated mesoscopic model of the biaxial NCF presented in the previous chapter is then used to simulate the forming process and compare it with the experimental results. The local defects are analyzed through both experimental and numerical observations.

Contents

4.1 Experimental forming tests

For efficient large-series production and improved process design, investigating the forming process is crucial to ensure form stability and adequate drapability. This process involves transforming 2D flat fabrics into a 3D shape through applied pressure by desired punch shape, with undergoing large deformations [8]. The large deformations experienced during this process have a direct impact on both the permeability and mechanical properties of the fabric. In the case of NCF, the deformation mechanisms rely on the unique combination of fiber orientation and bonding stitching pattern. Consequently, any alterations to the fiber structure during this process can significantly affect the overall structural performance of the fabric and may result in the occurrence of defects. Therefore, when analyzing the drapability of NCF, it is crucial to take into account key factors such as fabric types, fiber orientations, punch shapes, and the number of fabric layers. Before exploring complex industrial punch shapes, initial experimental tests were conducted on simpler academic shapes. These shapes were designed to represent the most challenging features, including double-curved surfaces and varying radii of edges and corners. The overview of experimental setup is presented in section 4.1.1. Two types of composite materials are used in the project: biaxial NCF and UD NCF. While the biaxial NCF was discussed in the previous section, the UD NCF consists of a single fiber direction within a single fabric layer. Glass fiber yarns are included to provide structural cohesion perpendicular to the carbon fiber yarn.

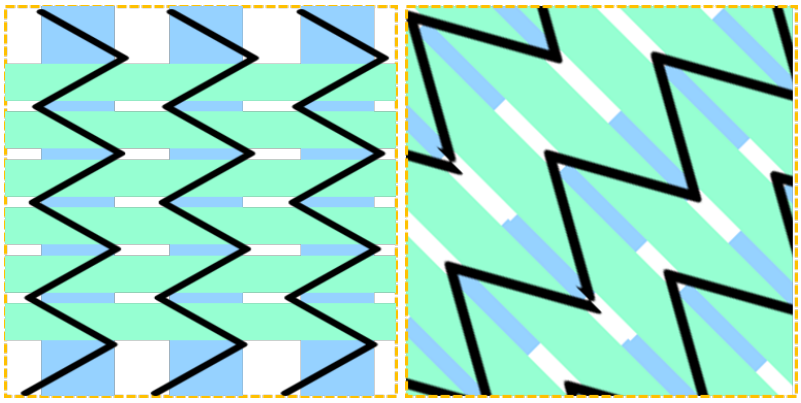

(a) (b)

Fig. 4.1: Fiber yarn orientation at initial state (a) $0°/90°$ (b) $\pm 45°$

Specimens were cut with different fiber orientations, as shown in Figure 4.1. Each type of test was performed twice: once on a sample with a white dot painted on it to measure macroscopic strain, and once on a sample without a white dot to confirm that the presence of the dot does not affect the results. The experimental results obtained from the biaxial NCF will be utilized to validate the scalability of mesoscopic model discussed in Section 4.2. The observed defects are presented in Section 4.3.

4.1.1 Forming experimental platform

The set-up developed for the experimental forming tests is presented in Figure 4.2. This consists of two modules: a mechanical module, housing the motion control system, punch, blank holder, and die for generating displacement and applying pressure; and an optical module, comprising two camera , mirror and lights for measurements. This forming experimental platform has been previously developed in LaMCoS and used for several researches [83, 102, 103].

The experimental set-up is placed on an electromechanical traction machine ZwichRoell 100KN where the motion part is driven by TestXpert software. The punch is connected to the motion part in order to deform the materials during the draping process. The blank holder and die are made transparent using methyl methacrylate (PMMA) material to allow for the acquisition of digital images by the optical module. The mirror is positioned at a $45°$ angle at the base, allowing the front camera to capture images from its reflection. A top-mounted camera is connected to the horizontal beam on the machine to capture images of the rear side for the double layer tests.

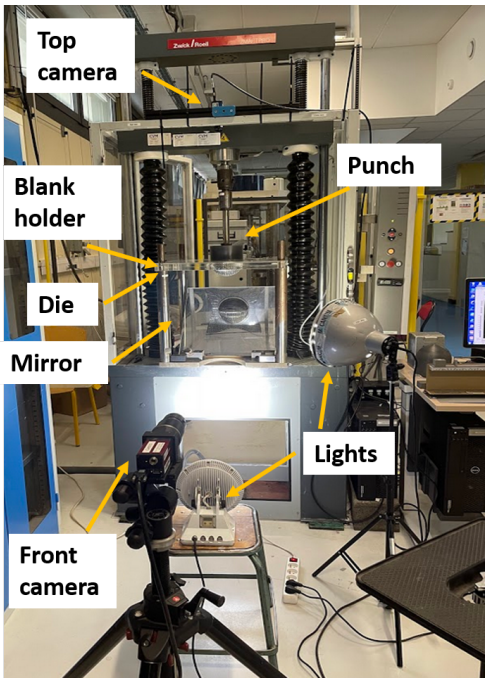

Fig. 4.2: Forming experimental platform setup

Three types of punches (hemisphere, tetrahedron, and square box), along with their corresponding shapes of blankholder and die, have been selected for the study. The hemisphere punch is the most commonly used academic shape in many researches for woven fabric and NCF. It is a rather simple double-curved geometry with a smooth curvature for the fabric draping. However in-plane shear deformation still happens and defects like gaping or wrinkles can also be observed. The radius of the hemisphere is $75\,\mathrm{mm}$, and the machine displacement for this shape is set at $75\,\mathrm{mm}$.

The tetrahedron exhibits a highly curved geometry with double curvature. Forming the tetrahedron is more challenging than shaping a hemisphere due to its smaller radius of

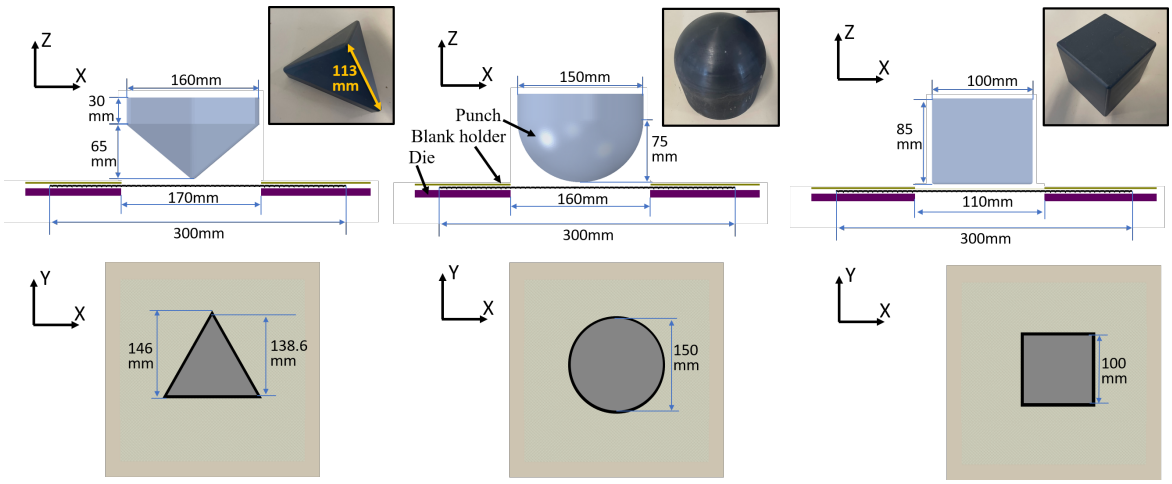

Fig. 4.3: Geometry setting of forming experiments

curvature. It is designed to simulate the slanted corners of complex components, resulting in higher shear angles and the occurrence of out-of-plane defects. The height of the tetrahedron shape is $65\,\mathrm{mm}$ and this punch also includes a vertical prism with a matching height of $35\,\mathrm{mm}$, equal to the die thickness. Thus the machine displacement for shaping this geometry is set at $95\,\mathrm{mm}$. The square box shape was initially developed for draping metallic materials. This shape has a significant depth, posing challenges for shaping, particularly at the corners. The majority of these tests analyzed woven fabric, with a smaller number focusing on NCFs. The square box has a side length $100\,\mathrm{mm}$ and the machine displacement is set as $85\,\mathrm{mm}$. Figure 4.3 illustrates the schematic and dimensions used for the forming tests on these three punch shapes.

4.1.2 Material preparation

In the previously presented Picture Frame and Bias Extension Tests, specimens were cut by hand since only a small number of specimens were required, and they were not of large dimensions. White dots were then manually painted one by one. However, for our large-scale forming tests which require a large amount of specimens, a more efficient method is necessary. At KIT-FAST, 100 samples of each UD and biaxial NCF were precisely and automatically cut from the same material roll using an automated cutting table supplied by Zünd Systemtechnik AG, Altstätten, Switzerland, and then sent to INSA-LaMCoS for experimental tests.

To apply the white dots pattern on the specimen, a transparent template measuring $150\,\mathrm{mm} \times 300\,\mathrm{mm}$ with punched evenly spaced holes at ten millimeter intervals was created. The template was then positioned on one side of the sample where white dots were desired for measurement. The white paint was applied using a brush, allowing it to permeate through the template holes and form the desired white dots. The white dot pattern for optical measurements is shown in Figure 4.4.

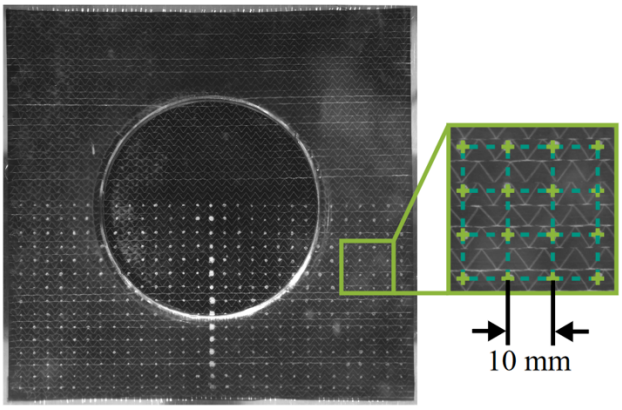

Fig. 4.4: White dot pattern for optical strain measurements [104]

4.1.3 Macroscopic strain measurement

The deformation is quantified using Digital Image Correlation (DIC) technology. An open-source DIC tool, developed using MathWorks MATLAB, was utilized to track the displacement of the white dot and has been effectively implemented for the analysis of forming test results [105]. The measurements primarily concentrate on the deformation

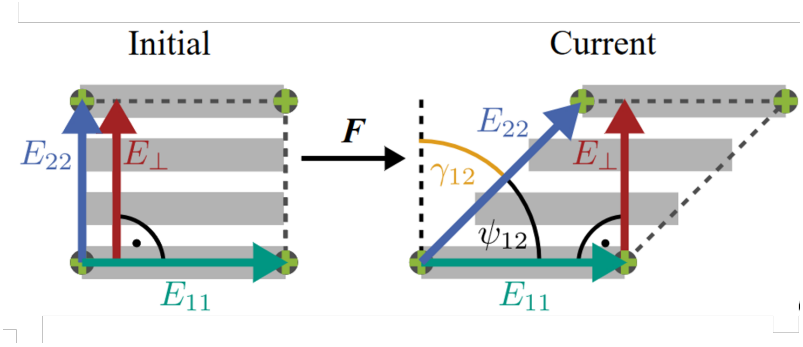

Fig. 4.5: Schematic of strain measures: Shear angle γ_{12}, transverse tensile strain E_{22} and perpendicular strain$E_{\perp}$ [104]

occurring in the 2D flat area, whereas the deformations in the draping area present a limitation. Three variables are quantified for both UD and biaxial NCF, including the shear angle between the two fiber yarns for biaxial NCF or between chain stitch and fiber yarn for UD NCF, the transverse tensile strain along the weft yarn direction for biaxial NCF and along the stitching direction for UD NCF, the perpendicular strain orient perpendicular to the warp fiber yarn.

As in-plane shear deformation is one of the primary deformation modes during the draping process, understanding this behavior necessitates measuring and analyzing the shear angle γ_{12} for both biaxial and UD NCF which is calculated according to

$$\gamma_{12} = \frac{\pi}{2} - \arccos\left(\frac{C_{12}}{\sqrt{C_{11}}\sqrt{C_{22}}}\right), \tag{4.1}$$

where $\underline{\underline{C}}$ is the right Cauchy-Green tensor.

In the case of transverse strain, biaxial and UD NCF exhibit dissimilarities. Biaxial NCF exhibits greater stiffness in the transverse direction due to the secondary fiber orientation, whereas the fiber yarns of UD NCF demonstrate lower stiffness as they are solely bonded by stitching in this direction. Perpendicular strain evaluates the separation distance

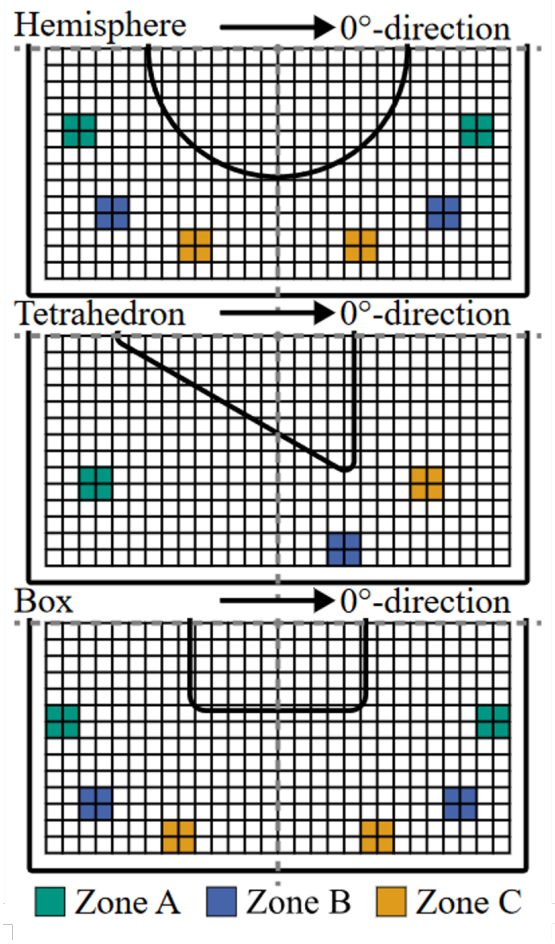

Fig. 4.6: Selected local zone for strain measurements [104]

between fiber yarns. It serves as an indicator for the occurrence of gaping ($E_\perp > 0$) as well as compression of fiber yarns ($E_\perp < 0$) at the macroscopic scale. It can be expressed as:

$$E_\perp = \sqrt{2\,E_{22} + 1}\sin(\psi_{12}) - 1, \tag{4.2}$$

In order to evaluate the evolution of the strain measures during the forming tests, three specific local zones are selected on the flat area for each punch shape, as depicted in Figure 4.6.

4.1.4 Results and discussions

The deformed configurations of all forming tests are captured by the top and front cameras at a rate of one frame per second. Each test includes approximately 180-200 photos,

enabling us to track the deformation throughout the process. The final configurations are depicted in Figure 4.7 and 4.8.

Punch force

The punch force serves as a direct measure of the energy needed to complete the draping process, and its magnitude is determined by both the mechanical properties of the fabric and the interactions between the samples and the tools. Figure 4.9 displays the punch force data captured by the load sensor on the machine. The punch force is normalized by the total mass m of the formed fabric in each test, providing an indirect normalization process that also enables a convenient comparison between single- and double-layer tests.

For the hemispherical and square box shapes, the differences in the normalized punch force between the biaxial and UD NCF are minimal. The double layer tests show little variation due to the low weight of the blank holder ($1.8\,\mathrm{kg}$). On the other hand, for the tetrahedron shape, the heavier blank holder weight ($6\,\mathrm{kg}$) contributes to a higher force in the double layer test of UD-NCF, which is comparable to the result of the single layer test of biaxial NCF. This phenomenon arises from the interaction between layers.

The hemisphere shape exhibits a smooth punch force curve due to its smooth, constant curvature at the edge. The tetrahedron shape, characterized by $65\,\mathrm{mm}$ beveled edges and $35\,\mathrm{mm}$ vertical edges, results in a surge in the force curve at the dotted line. This observation indicates that the formation of vertical edges is more challenging and requires more energy. In the [45°] and [90°] single-layer tests of the UD-NCF, the textile was partially entangled in certain corners during this transition, leading to the formation of larger gaps and resulting in a sudden increase in punch forces. The square box yields intriguing findings as its edges remain vertical, yet the force experiences a sudden slowdown in growth after $30\,\mathrm{mm}$ of draping. In the first stage, the in-plane shear angle of the fiber yarns increases rapidly due to the difficulty in forming a vertical shape, which can be observed in the results of the local zone analysis, as depicted in Figure 4.15. Consequently, a higher amount of energy is consumed during this stage. In the second stage, the shear angle has already reached a high value, and the primary mechanism at play is the friction between the tool and the fabric.

Outer contour

The fabric outer contour serves as a visual representation of the final shape resulting from material deformation, allowing for intuitive assessment of the extent of deformation. Comprising the accumulated material draw-in across various locations, the fabric contour functions as a holistic indicator of material draping. It can then be used to validate the numerical simulation results. Furthermore, the fabric after forming consists of one effective zone that represents the desired shape and one non-effective zone that needs to be removed in the subsequent process. Analyzing the outer contour after forming aids in minimizing material waste and production costs during manufacturing.

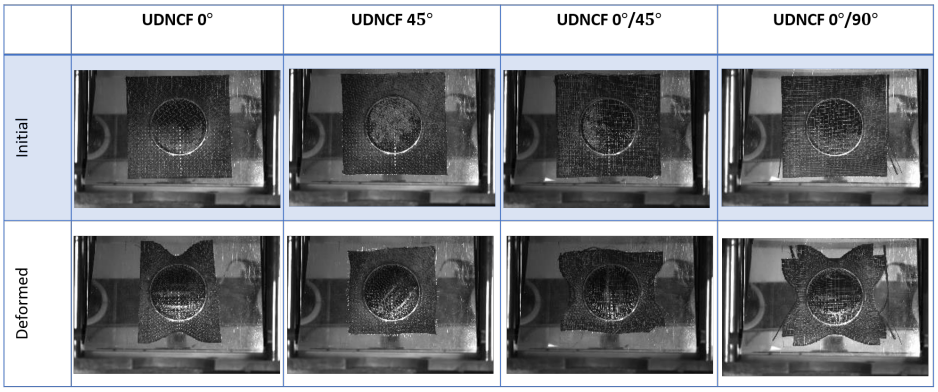

(a)

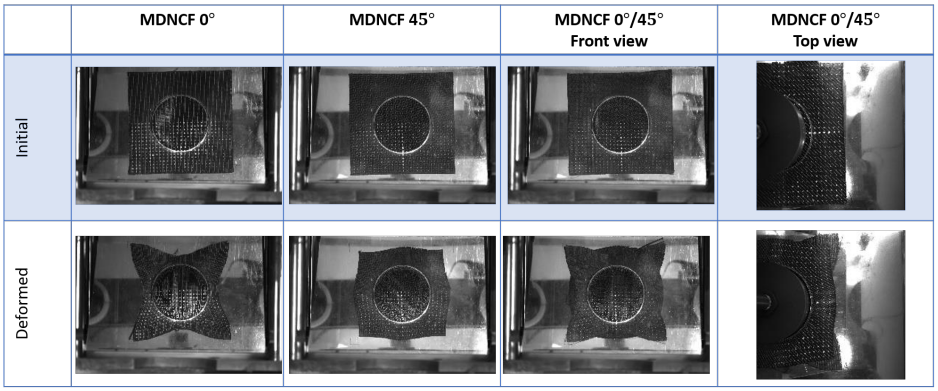

(b)

Fig. 4.7: Initial and final deformed configuration of Hemisphere forming of (a) UD-NCF (b) Biaxial NCF

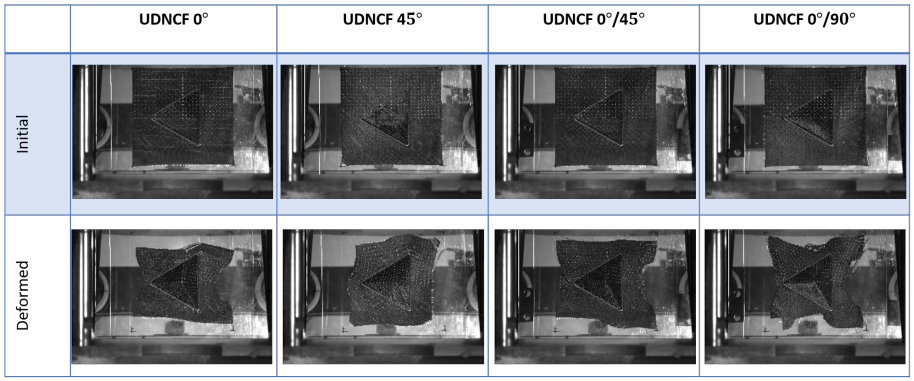

(a)

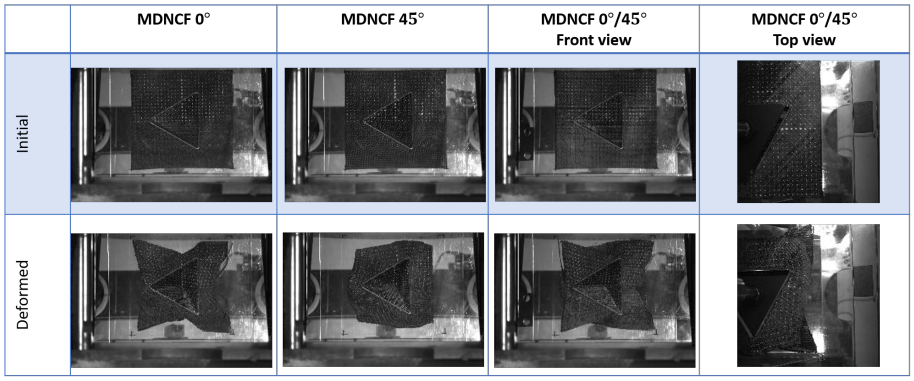

(b)

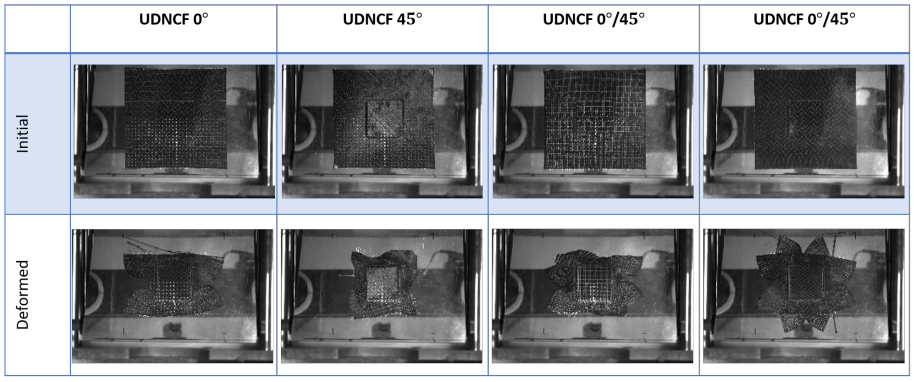

(c)

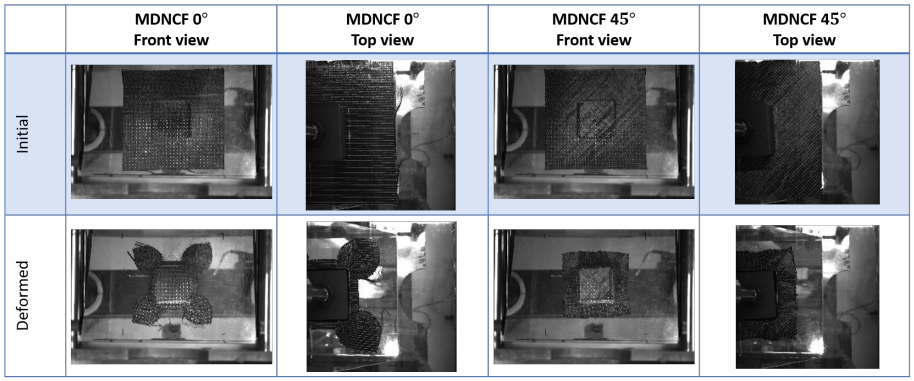

(d)

Fig. 4.8: Initial and final deformed configuration of tetrahedron forming of (a) UD-NCF (b) Biaxial NCF and square box forming of (c) UD-NCF (d) Biaxial NCF

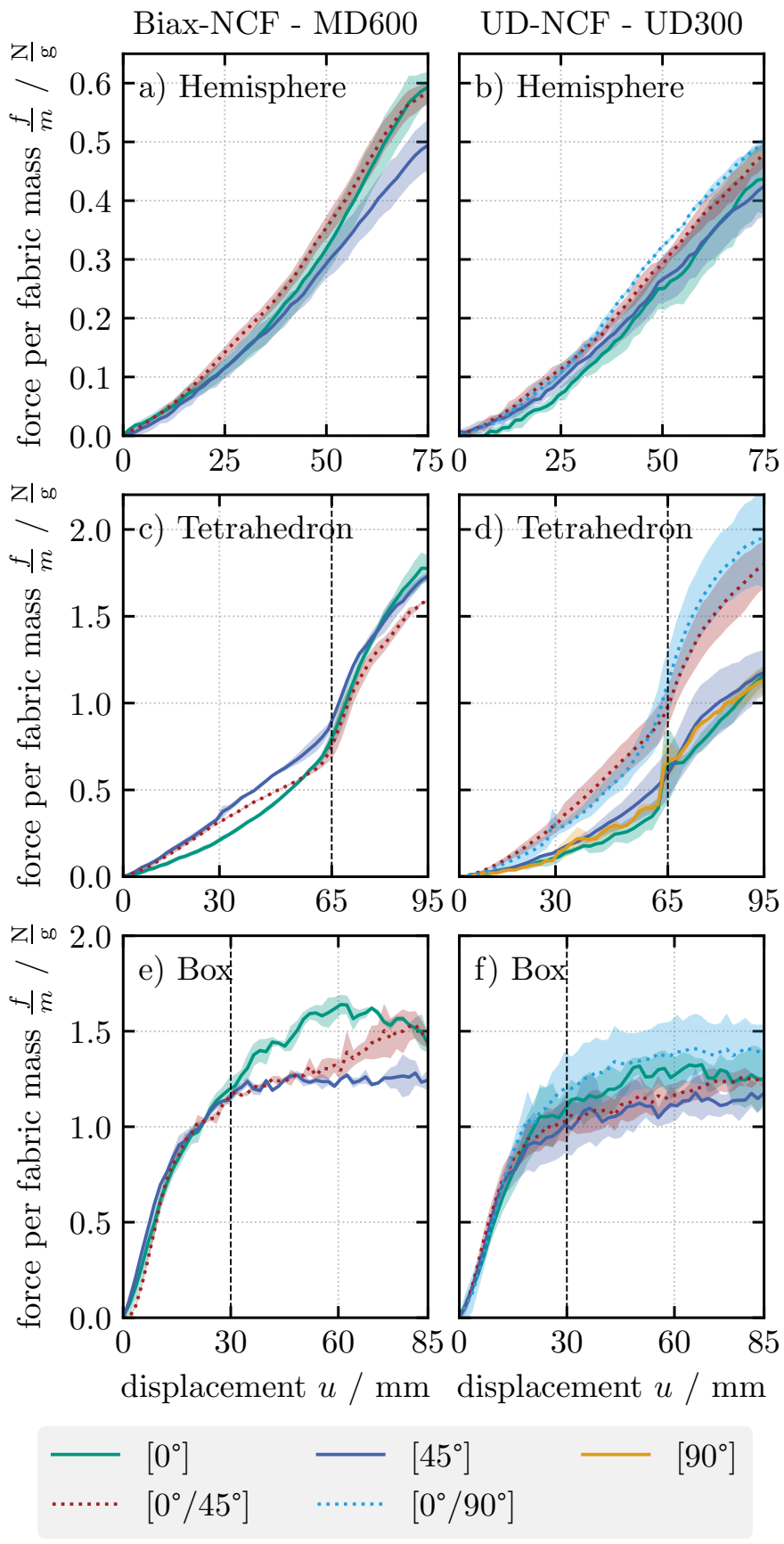

Fig. 4.9: Forces recorded from the load sensor on different forming tests [104]

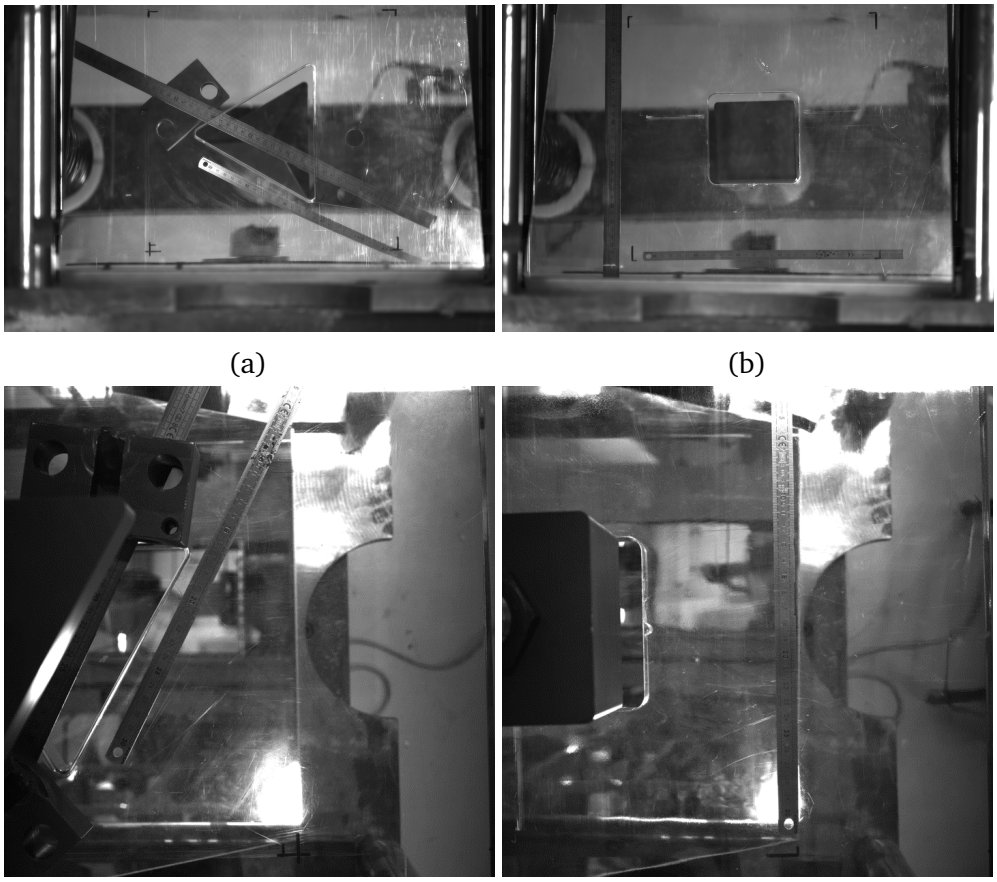

(a) (b)

(c) (d)

Fig. 4.10: Calibration system for (a) front camera for hemisphere and tetrahedron shape (b) front camera for square box shape (c) top camera for hemisphere and tetrahedron shape (d) top camera for square box shape

In the experiment, a ruler is placed next to the specimen as a calibration system which establishes a link between the pixel coordinates and the actual coordinate system, as shown in Figure 4.10. This calibration system allows for the representation of the true dimensions of an object in the image by mapping it onto the real coordinate system. The resulting outer contours of all tests are shown in Figure 4.11.

The biaxial NCF displays a nearly balanced structure characterized by a symmetrical stitching pattern and an approximately equal distribution of carbon fibers in both directions of reinforcement. Consequently, its maximum material draw-in occurs symmetrically in both fiber directions, leading to the formation of a quarter-symmetrical contour for both the point symmetrical hemisphere and box shape. For the axisymmetrical tetrahedron shape, the contours of the biaxial NCF exhibit half-symmetry. The UD NCF, due to its single preferred direction and half-symmetrical structure, results in half-symmetrical contours in hemisphere and square box tests, as well as in 0° and 90° tetrahedron tests. On the other hand, in a 45° tetrahedron test, the UD NCF loses its symmetry entirely.

Strain

The strains during the tests were measured with DIC approach. The analysis will focus solely on the flat area, as the measurement method used is limited to 2D. Analyzing the 3D area would necessitate finding a means to remove the textile from the mold, which is more commonly employed for fabrics that have a binder [106, 107].

The results of the forming tests for the hemisphere, tetrahedron, and square box are illustrated in Figure 4.12, 4.13 and 4.14, respectively. Each column in the figures represents the measured shear angle, transverse tensile strain, and perpendicular strain. The different lines in the figures correspond to tests conducted on various fiber orientations. For each value in each test, two captured images were selected: at the 75% and 100% punch deform position.

For the biaxial NCF, the transverse tensile strain is almost negligible across all tests due to the presence of a second fiber orientation that enhances stiffness. In contrast, UD NCF exhibits larger transverse strains. The stitches need to be tensioned to secure the fiber yarns. In the double layer test, the stitch tension is decreased due to the additional draw-in of the second layer. The perpendicular strain of biaxial NCF is mostly less than zero during the tests which indicates the compression of fiber yarns. After comparing the results of the shear angle and perpendicular strain, it is evident that the compression is positively correlated with the magnitude of the shear angle. As the shear angle increases, the compression becomes more significant.

Figure 4.15 illustrates the measurement of shear angles at three selected local zones for each shape. The shear angles in the local zone A and B in hemisphere forming tests, and local zone A and C in square box tests, demonstrate symmetrical shear deformation of biaxial NCF. The shear angle curve closely correlates with the punch force results, as it reflects the energy required to deform the fabric, with in-plane shear being one of the primary deformation mechanisms. In the case of the hemisphere shape, shear angles at all three zones increase smoothly due to the constant curvature of the hemisphere. However, for the tetrahedron and square box shapes, the small corner radius results in higher shear

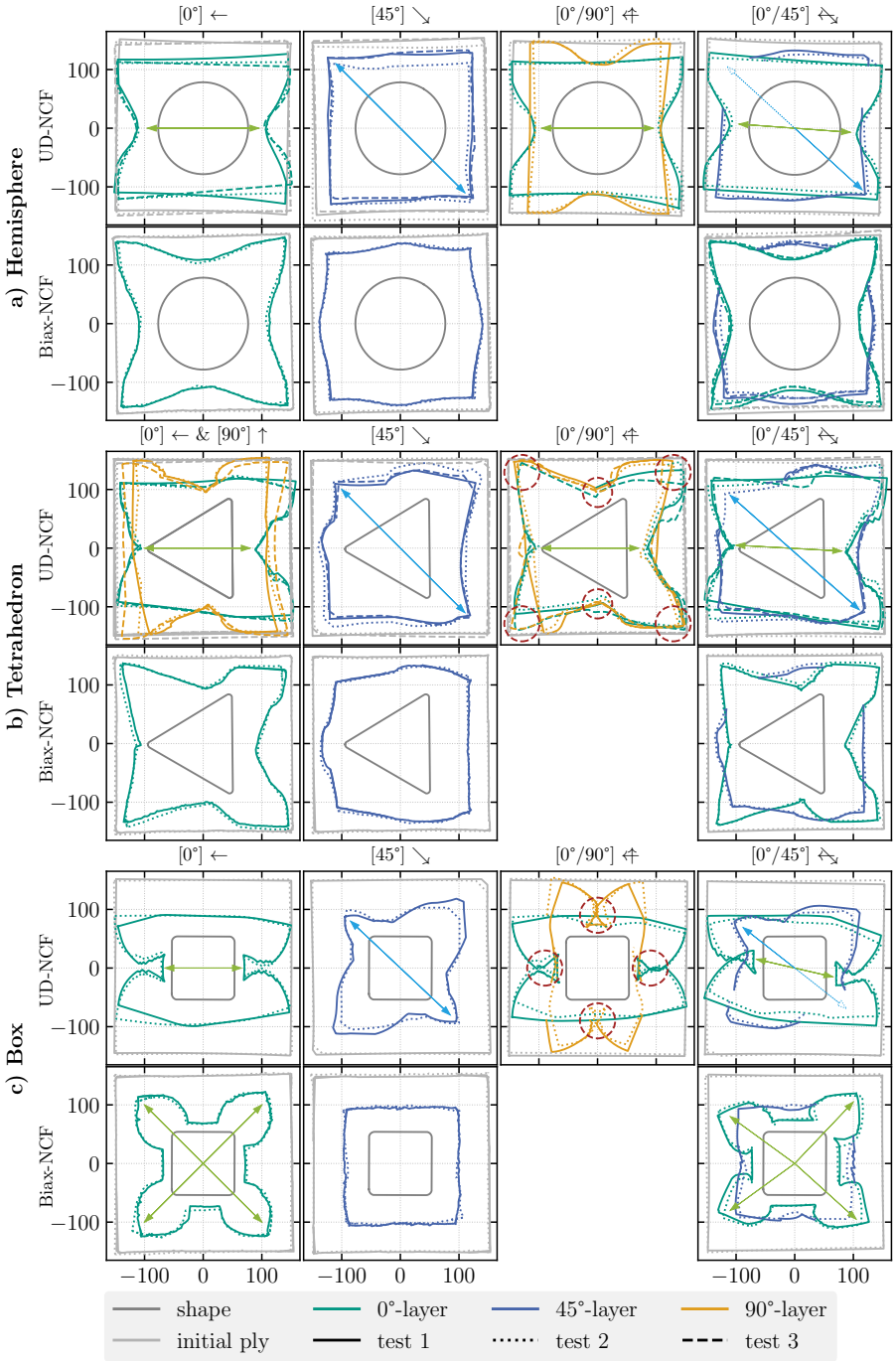

Fig. 4.11: Outer contour [104]

angles compared to those of the hemisphere shape. Additionally, the vertical shape with significant depth proves challenging to form, resulting in a significant increase in shear angle, as shown in the second stage of tetrahedron forming and first stage of square box forming.

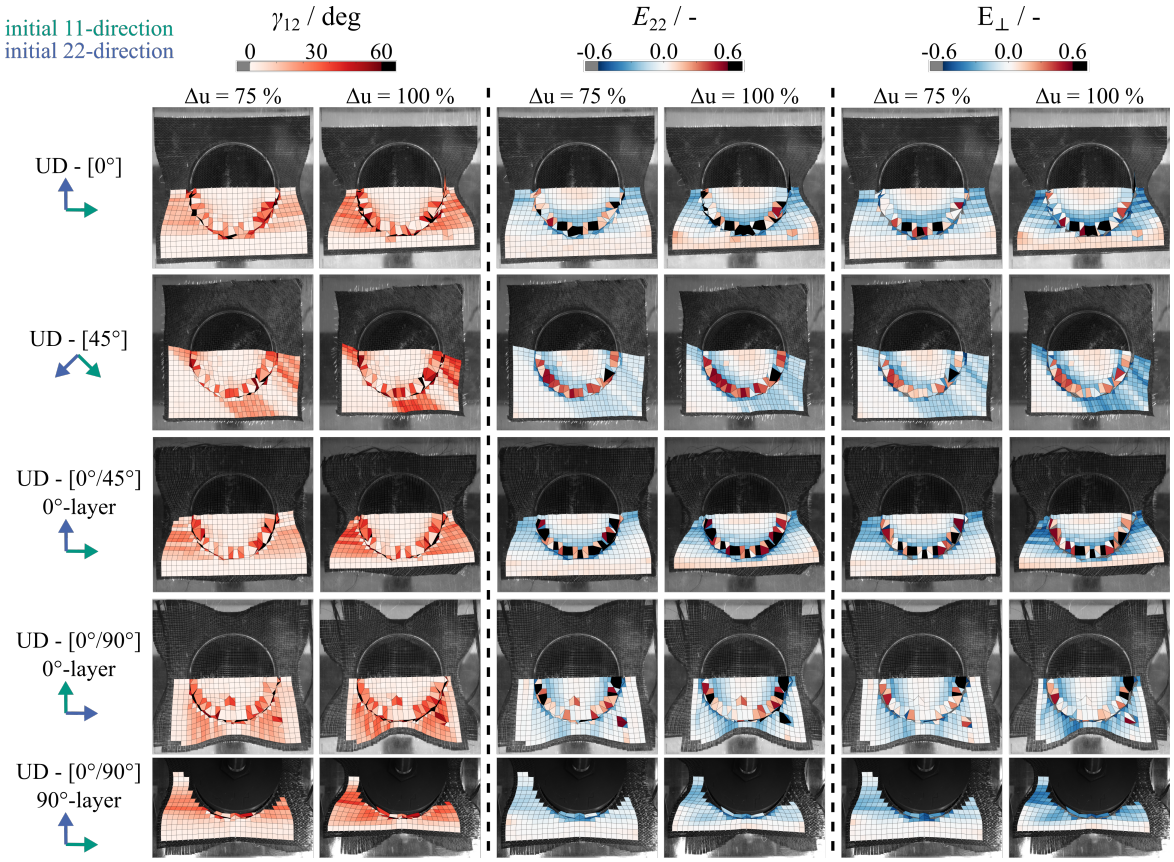

(a)

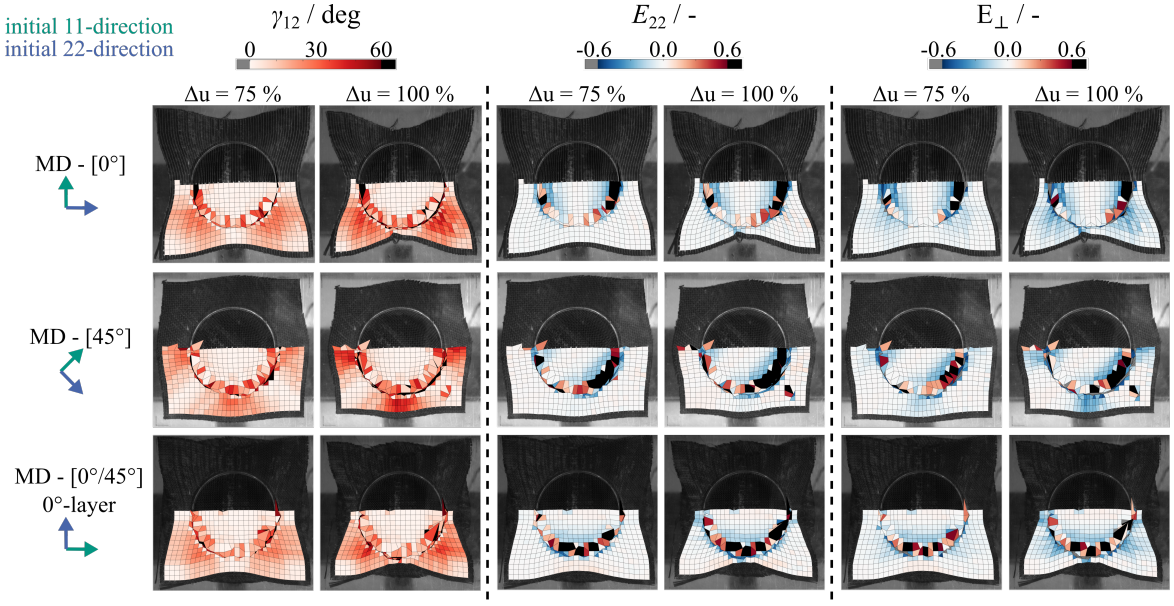

(b)

Fig. 4.12: Strain measurements of hemisphere forming (a) UD NCF (b) Biaxial NCF [104]

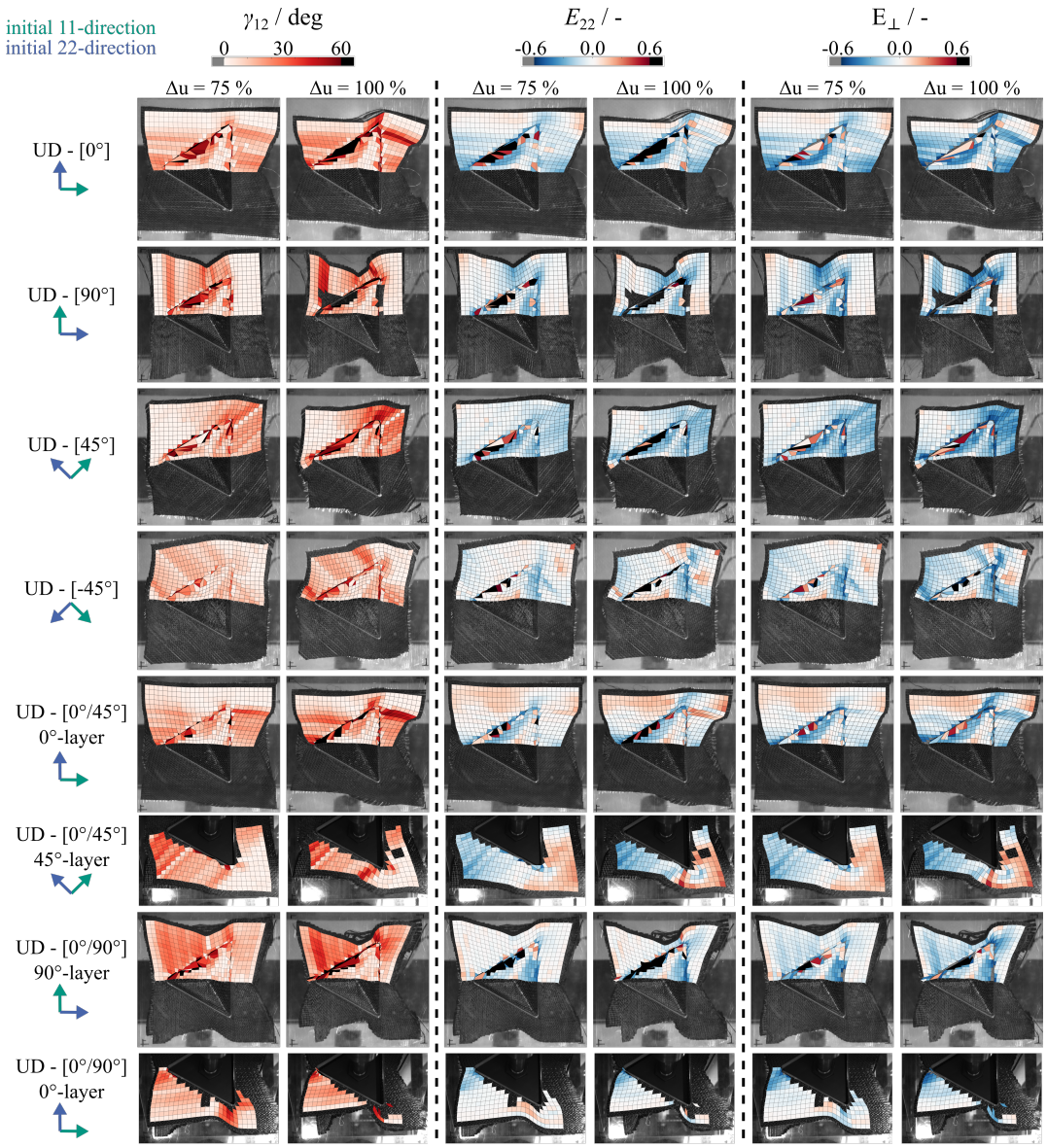

Fig. 4.13: Strain measurements of tetrahedron forming (a) UD NCF (b) Biaxial NCF [104]

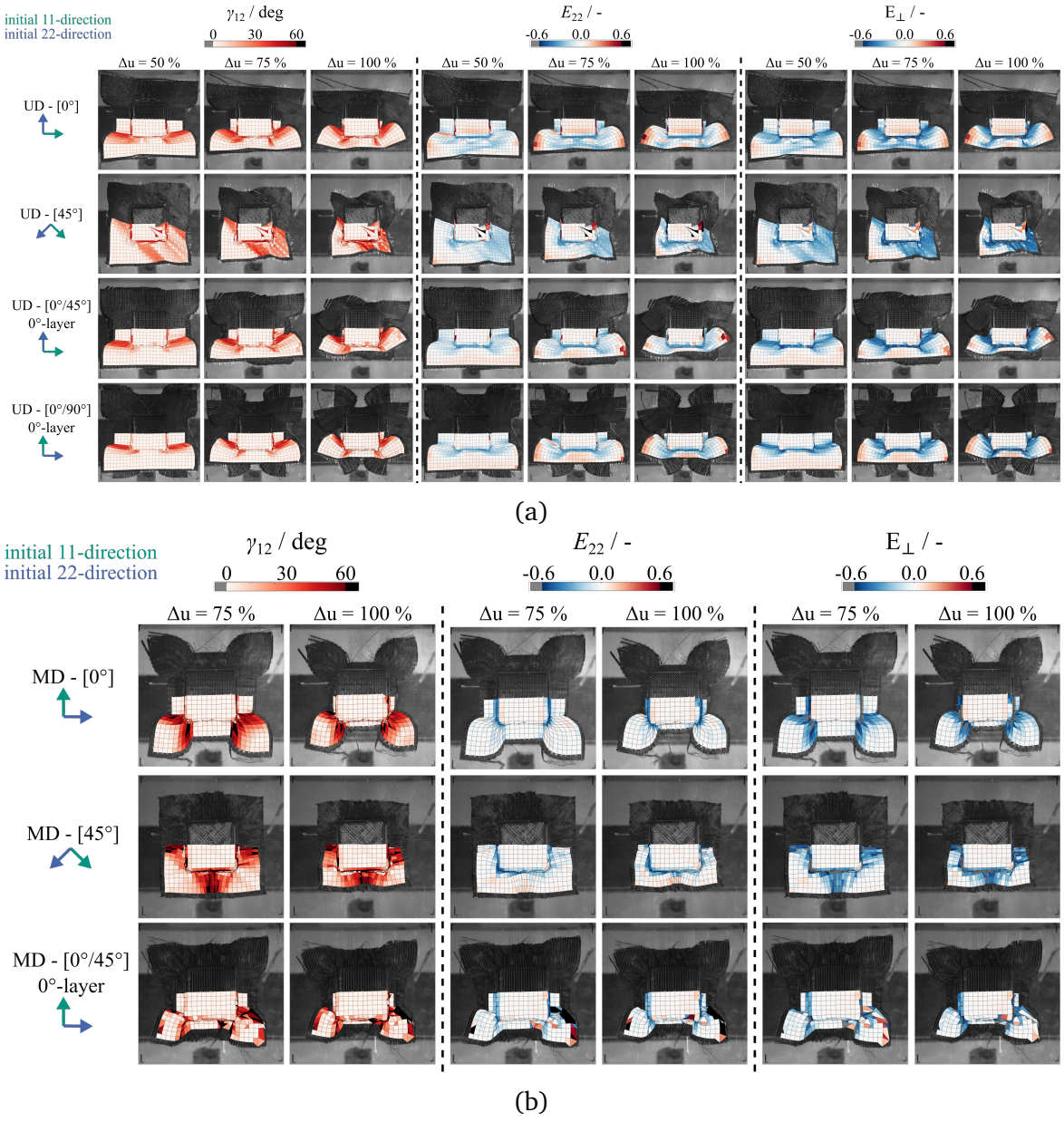

Fig. 4.14: Strain measurements of square box forming (a) UD NCF (b) Biaxial NCF [104]

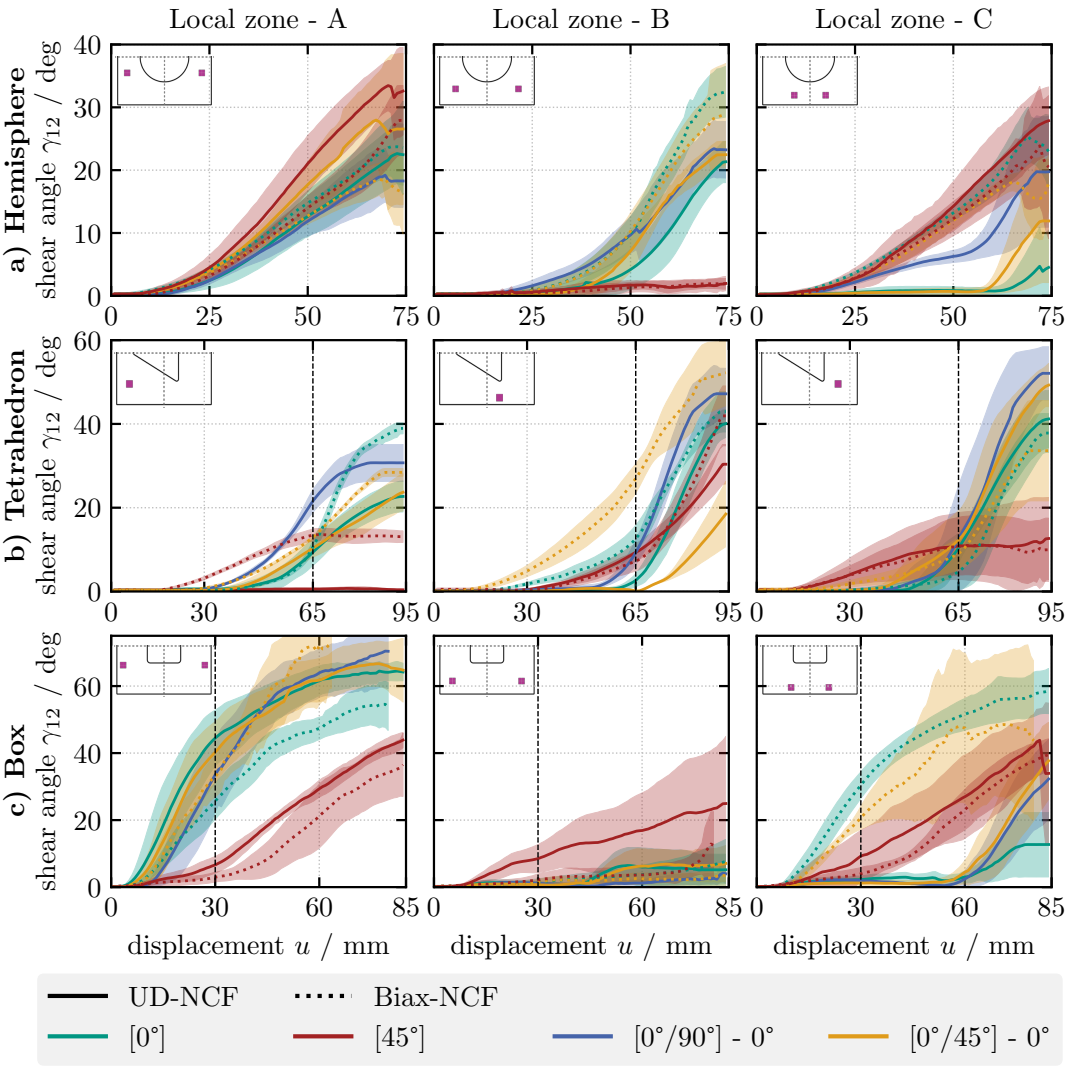

Fig. 4.15: Shear angle measured at local zones [104]

4.2 Numerical simulation results

In order to achieve efficient and defect-free manufacturing while minimizing the need for time-consuming and costly experimental tests, it is necessary to have a reliable simulation and optimization of the forming process. The fiber directions will change in the final composite part which will influence its mechanical behavior. And defects such as wrinkles and gapings may occur. Consequently, the simulation should accurately forecast the forming behavior by considering parameters such as fabric structure and optimizing the shaping device. Most forming simulations have centered on woven fabrics, with limited consideration given to NCFs. Moreover, none of the current simulations comprehensively capture all the local effects, which requires a mesoscopic modeling.

4.2.1 Simulation setup

The forming tests are numerically simulated using ABAQUS/Explicit. The mesoscopic model of bi-axial NCF that presented in the previous chapter is utilized. Due to the symmetry of bi-axial NCF, the symmetrical hemisphere and square box punches are modeled using a quarter-sized sample ($150\,\mathrm{mm} \times 150\,\mathrm{mm}$), while the axisymmetric tetrahedron shape is modeled using a half-sized sample ($150\,\mathrm{mm} \times 300\,\mathrm{mm}$) to minimize computation costs. The quarter-sized model consists of 57,840 solid elements for two plies of fiber yarns, 10,858 beam elements for the enhanced yarn beam, and 58,441 beam elements for stitches. The half-sized model contains twice the number of elements.

The model for the punch, die and blank holder for different shapes are shown in Figure 4.16. They have the same dimensions as those used in the experimental tests. In the forming tests, these tools experience minimal deformations; therefore, they are modeled as rigid bodies (ABAQUS R3D4 elements). The die and blank holder are fixed in their positions throughout the simulation, while a draping displacement is prescribed for the punch. Coulomb friction contact is employed for the interaction between the tools and the fabric.

For a quarter part used in the simulation, boundary conditions are applied to the two sides adjacent to the symmetrical point. The displacement of the right side is constrained in the X-axis direction, whereas the displacement of the top side is constrained in the Y-axis direction. For the stitches on the right side, they lack the constraint imposed by another stitch part. Consequently, they can move freely along the fiber yarn direction, but this minor displacement will not affect the final results.

All the simulation jobs are launched on the cluster with 20 CPU cores. The computation takes 6 days each, which is the maximum time allowed for one computation on Cluster. It can be extended using the restart function.

4.2.2 Hemisphere forming

The first launched simulation is the hemisphere forming on quarter-sized part of single layer of biaxial NCF. The draping displacement is set at $75\,\mathrm{mm}$. This quarter is then

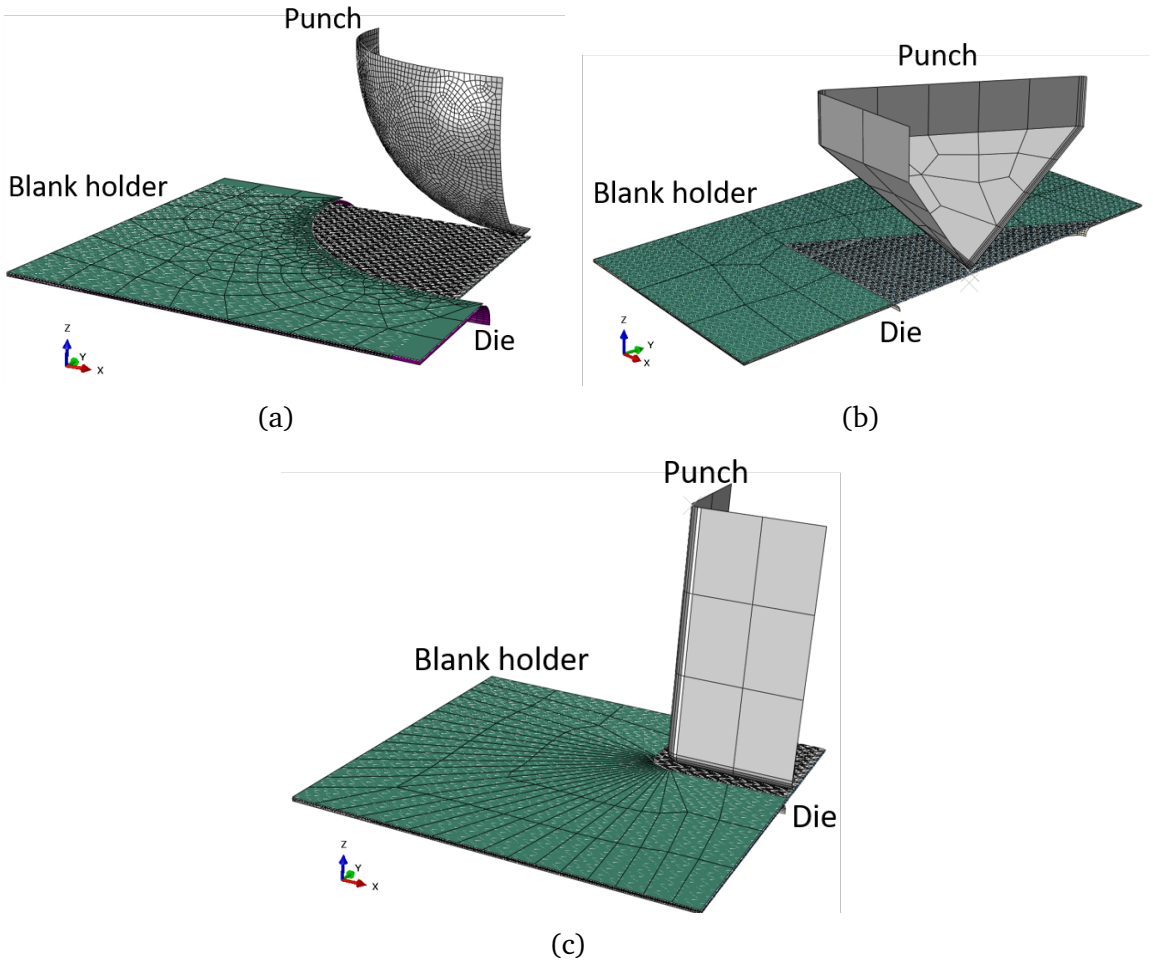

Fig. 4.16: Forming tools modeling (a) Hemisphere (b) Tetrahedron (c) Square box

mirrored to obtain the overall forming result. Figure 4.17 shows the 3D view of the final part. Figure 4.18 shows the 2D view obtained by (a) experiment and (b) simulation. A comparison of the deformations reveals that the simulation produces an edge shape of the reinforcement resembling the one obtained experimentally. The outer contour of the simulation results is also drawn through the image processing on the 2D view. Figure 4.19 displays the contour comparison. The red line represents the contour of the hemisphere forming results of 0° biaxial NCF, while the blue line depicts the simulation results. It can be observed that the simulation exhibits a similar material draw-in as the experimental result.

Another requirement for the simulation is its ability to accurately trace the yarn direction in the final composite part. The mesoscopic model utilizes the same approach presented in Chapter 3 in the Bias-extension Test to trace the fiber yarn direction. The two material directions are extracted from the numerical results. These directions are then employed to calculate the shear angles, which are subsequently compared with the experimental results, as shown in Figure 4.20. The colorbar range is set from 0° to 60°, with areas of higher shear angles denoted by a more intense red color. These areas of higher shear angles exhibit good agreement with the experimental results, where both tensioned and loosened stitches are observed.

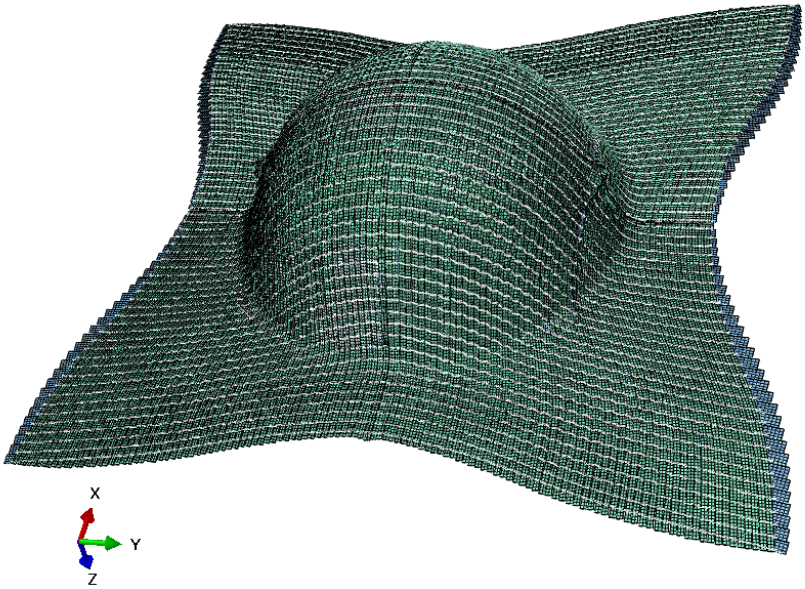

Fig. 4.17: 3D view of hemisphere forming simulation

The slippage between the warp and weft yarns can also be observed at the edge of the final shape, as depicted in Figure 4.21. The slip distance appears slightly larger in the simulation due to the inclusion of a half yarn on the boundary, which remains fixed throughout the process due to the loss of the stitch constraint. However, this observation still highlights the ability of the mesoscale model to capture interply slippage phenomena, which cannot be observed in macroscopic simulations.

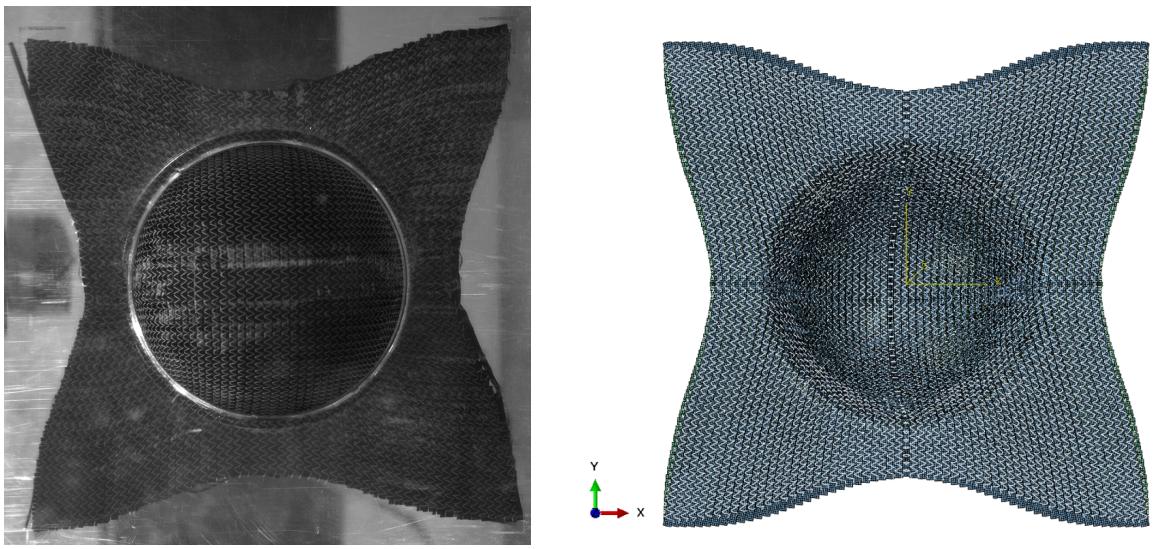

(a) (b)

Fig. 4.18: 2D view of hemisphere forming comparing (a) Experiment (b) Simulation

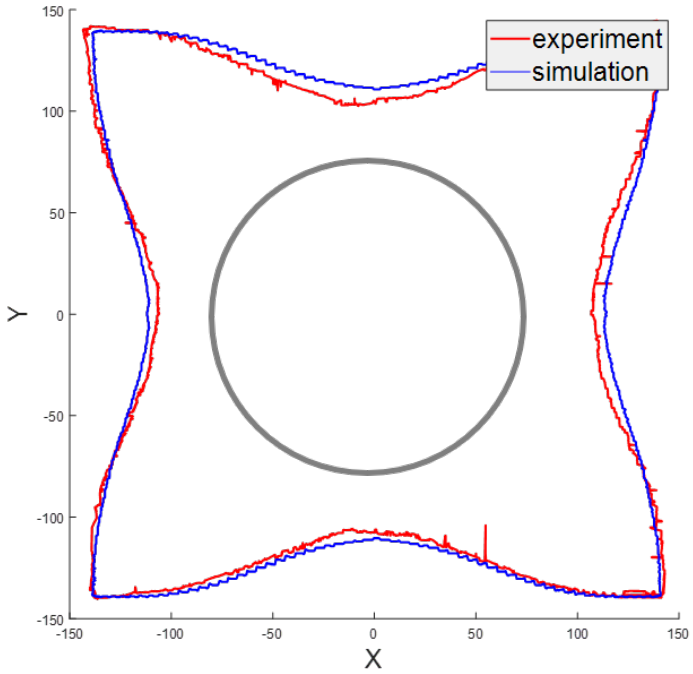

Fig. 4.19: Hemisphere forming contour comparison

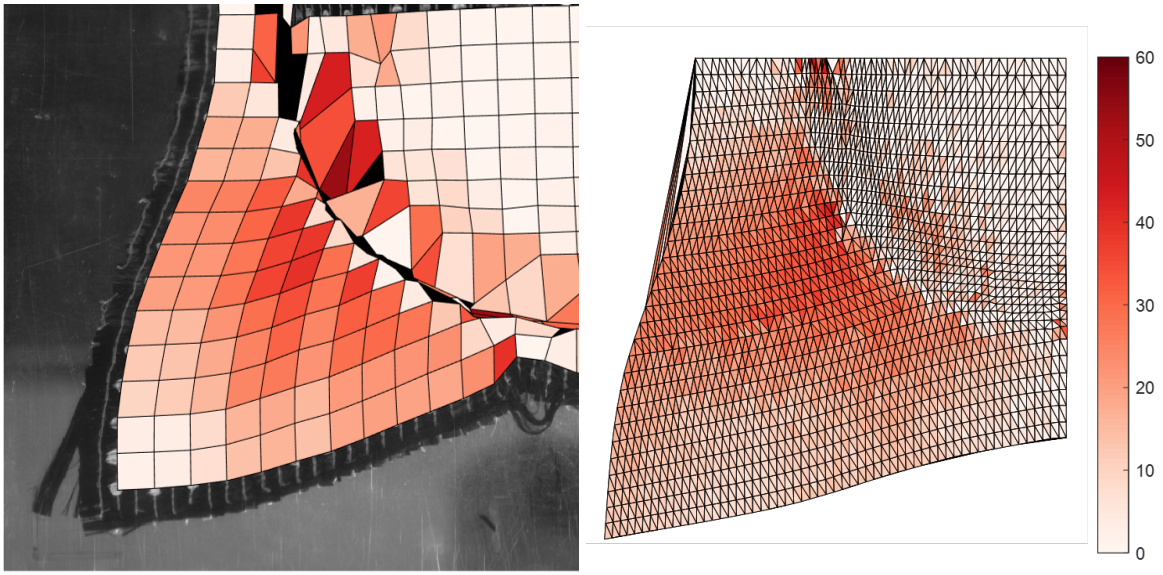

(a) (b)

Fig. 4.20: Visualisation of shear angle in hemisphere test (a) Experiment (b) Simulation

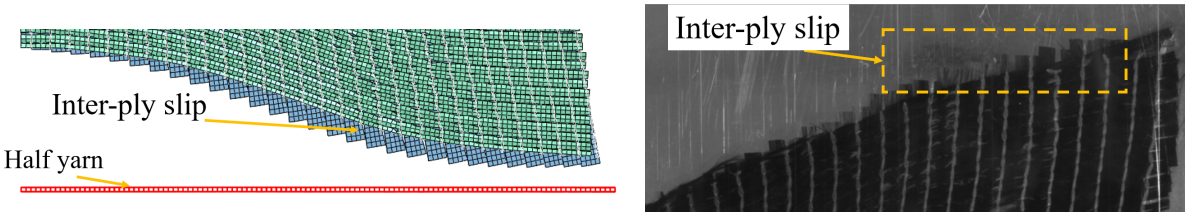

(a) (b)

Fig. 4.21: Slip between warp and weft yarn (a) simulation (b) experiment

4.2.3 Square box forming

The square box forming test is also launched on a quarter-size part. From the experimental results, we observe that at punch displacement $30\,\mathrm{mm}$, the shear angle has already reached a high value. After that, the increase of shear angle slows down, as well as the punch force. This first stage is where the fiber structure change and defects may happen. In order to reduce the calculation time, the draping displacement for square box simulation is set up as $40\,\mathrm{mm}$. The 3D view of the deformed shape is shown in Figure 4.22 and the 2D views obtained by experiment and simulation are shown in Figure 4.23. The comparison of the contour is shown in Figure 4.24 and similar material drawn-in can be observed.

The visualisation of shear angle in square box forming test is shwon in Figure 4.25.

4.2.4 Tetrahedron forming

The tetrahedron forming test is launched on a half part. The punch displacement is set at $60\,\mathrm{mm}$ since we will focus on the tetrahedron shape. The 3D view of the deformed shape is shown in Figure 4.26 and the 2D views obtained by experiment and simulation are shown in Figure 4.27. The comparison of the contour is shown in Figure 4.28.

Fig. 4.22: 3D view of square box forming simulation

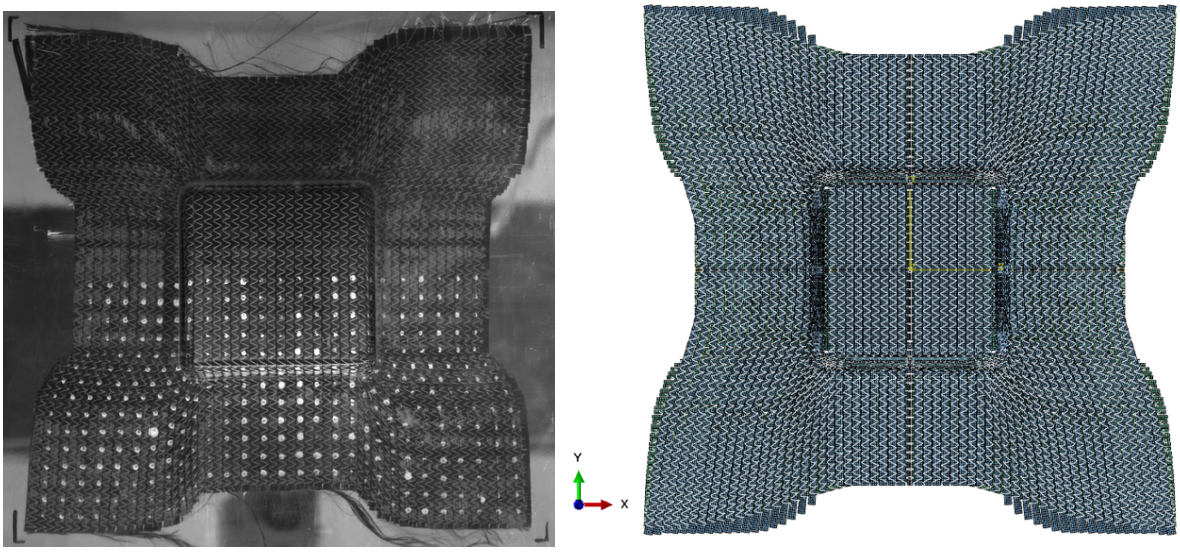

(a) (b)

Fig. 4.23: 2D view of square box forming comparing (a) Experiment (b) Simulation

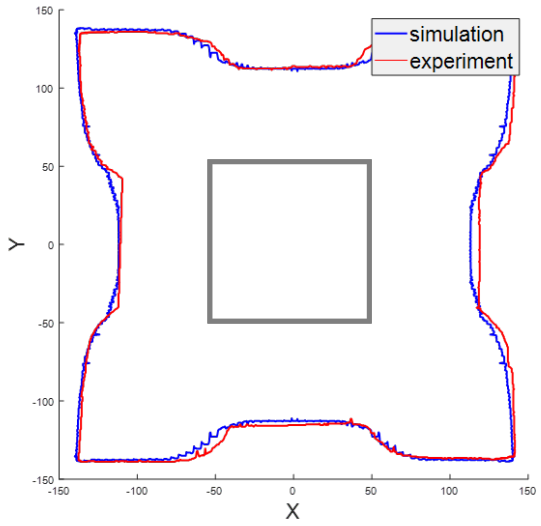

Fig. 4.24: Square box forming contour comparison

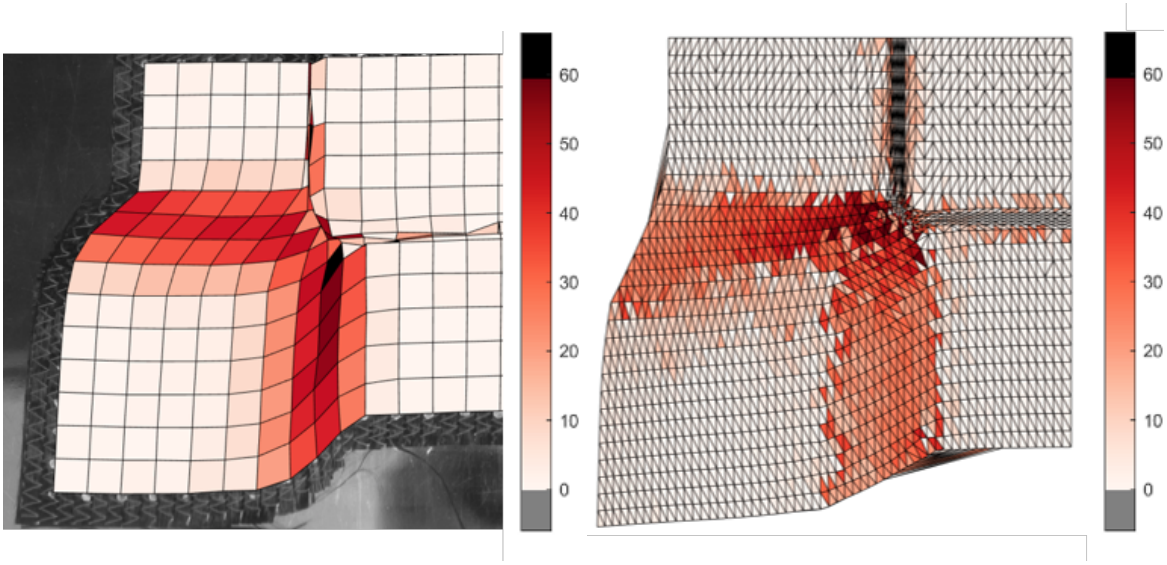

(a) (b)

Fig. 4.25: Visualisation of shear angle in square box forming test (a) Experiment (b) Simulation

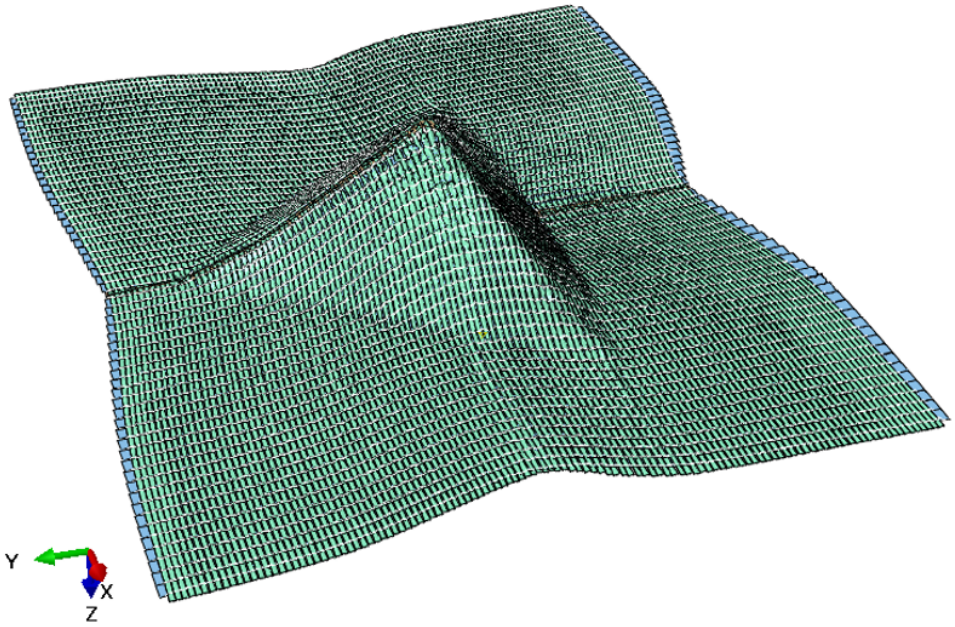

Fig. 4.26: 3D view of tetrahedron forming simulation

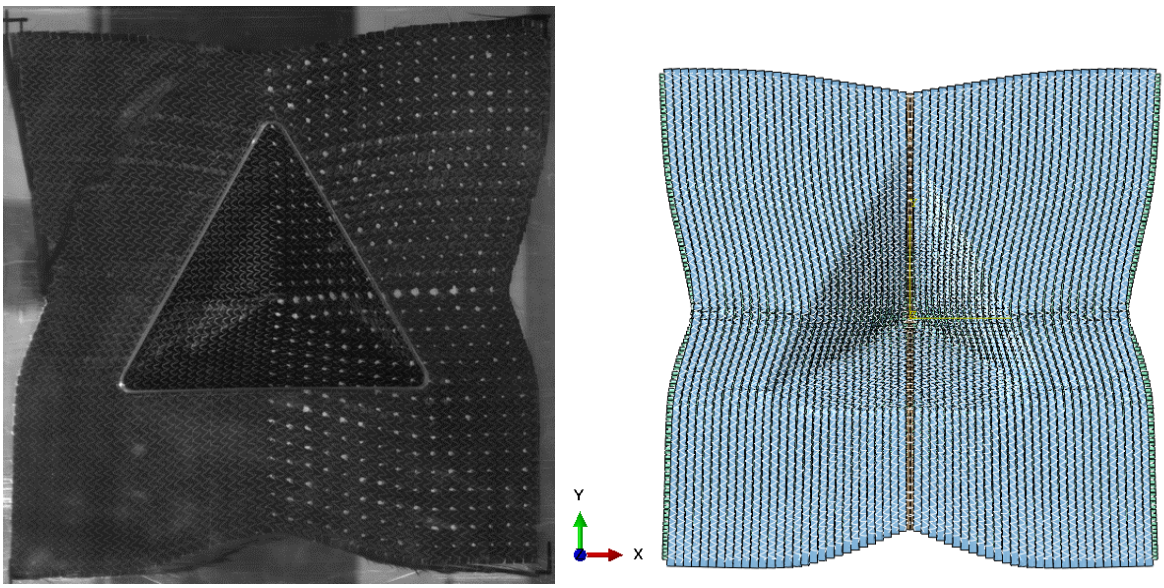

(a) (b)

Fig. 4.27: 2D view of Tetrahedron forming comparing (a) Experiment (b) Simulation

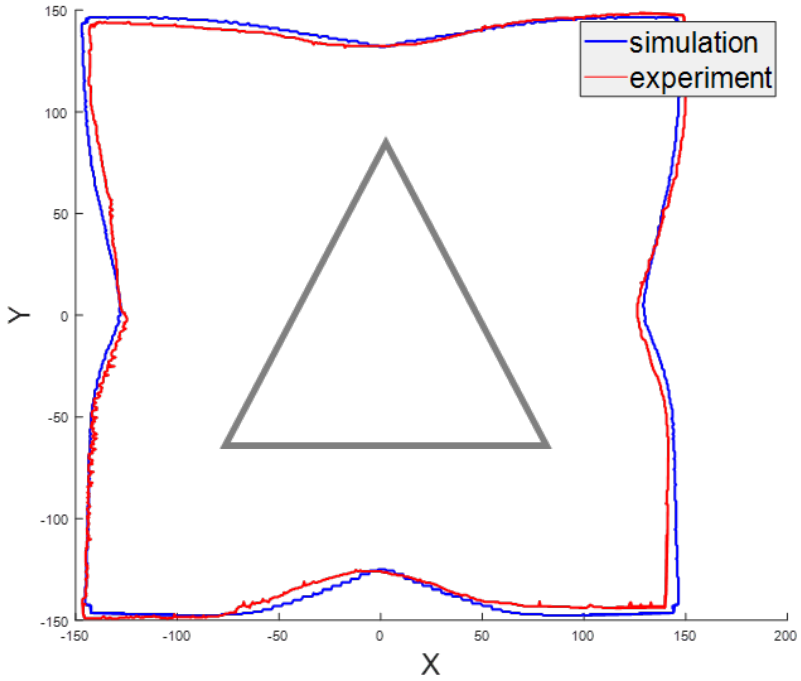

Fig. 4.28: Tetrahedron forming contour comparison

4.3 Observation of forming defects

Defects may occur during the forming process due to variations in part geometry, reinforcement type, and experimental setup. Detecting the presence of defects is a primary objective of conducting these forming tests and simulations. gaping and wrinkles are among the most common defects observed in NCFs. The wrinkles can be observed if the yarn is bent out-of plane, while a gaping defect occurs when the yarns move away from each other and leave a space without fibers.

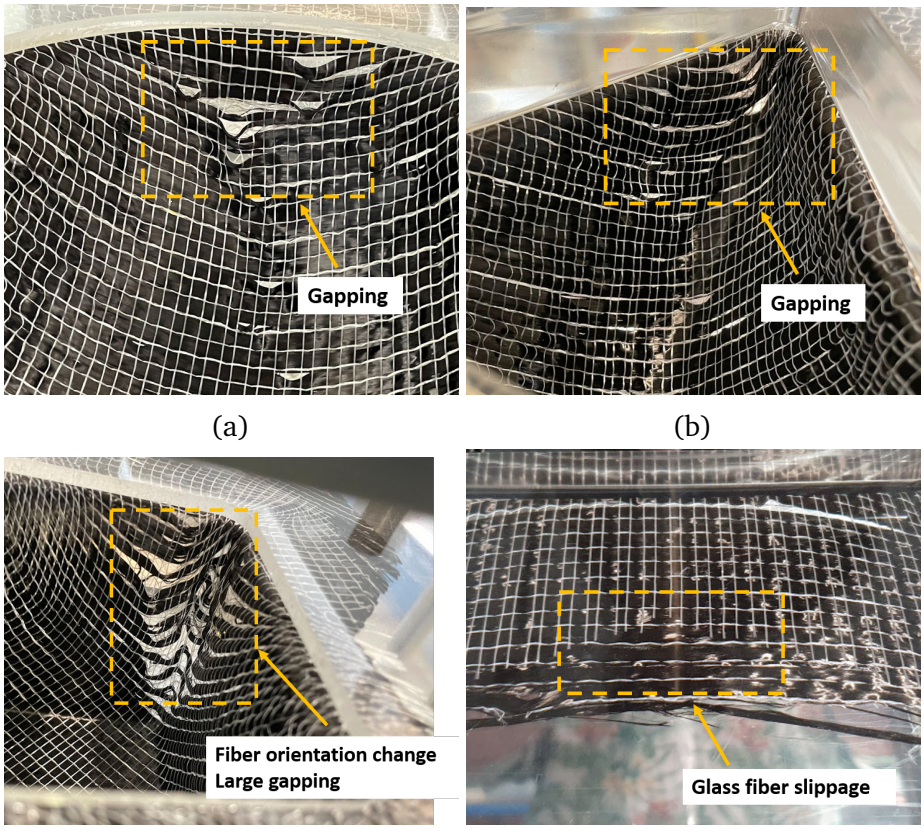

Fig. 4.29: Defects observed for UD NCF, gaping in (a) hemisphere forming (b) tetrahedron forming (c) square box forming, and (d) glass fiber slippage on the flat area in tetrahedron forming

Compared to biaxial NCF, UD-NCF has a lower stiffness along the glass fiber direction, causing large transverse tensile strains during forming. Consequently, gaping and slippage of glass fiber yarn are observed, as shown in Figure 4.29. Furthermore, substantial in-plane bending deformation of the fiber yarn occurs, resulting in a change in fiber orientation. This phenomenon is particularly prominent at the corners of the tetrahedron and square box shapes, where significant gaping is observed.

In the case of biaxial NCF, the structural integrity is enhanced through two fiber orientations and is further secured by stitches. Only minimal gaping is noticeable on a smooth hemisphere shape, as depicted in Figure 4.30a. No gaping is observed in the simulation results, as shown in Figure 4.30b. However, when dealing with the challenging

square box shape, gaping can be observed at the corners of the shape, as illustrated in Figure 4.30c. The square box forming simulation also exposes a significant gaping defect occurring in this region, as depicted in Figure 4.30d.

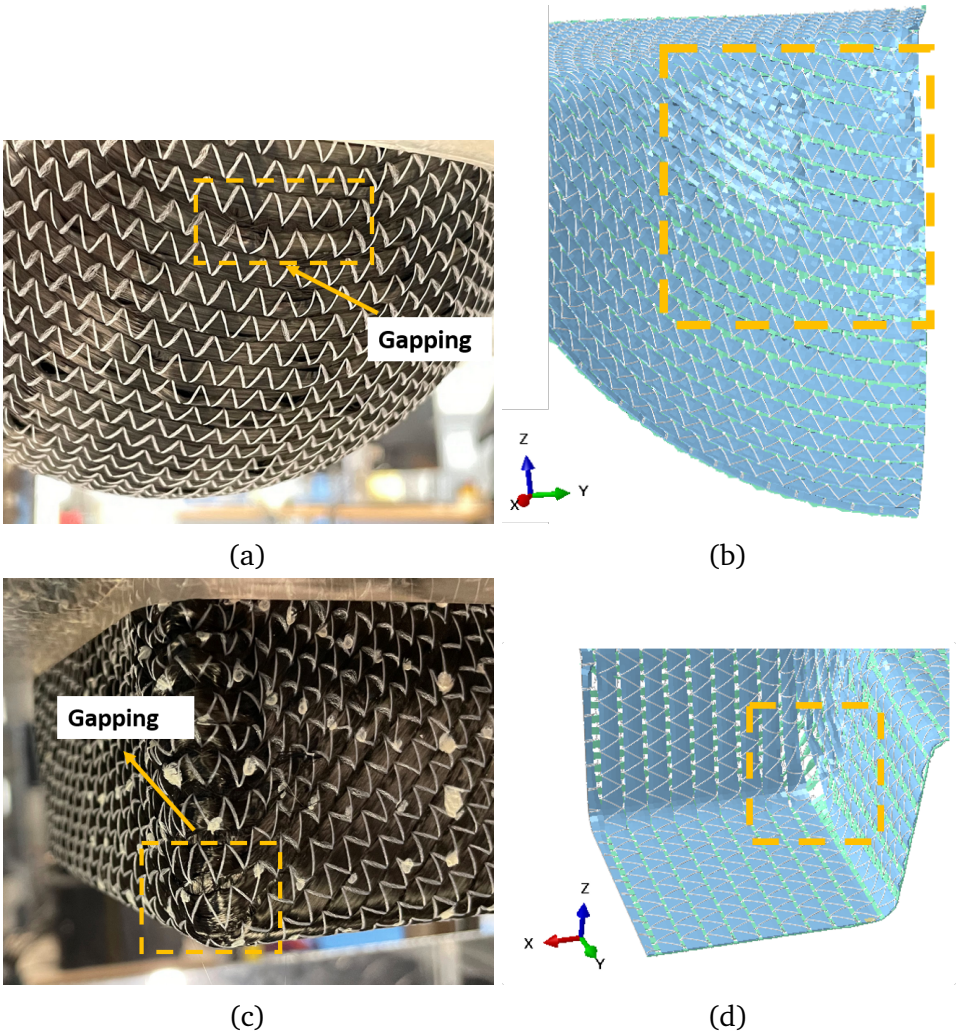

Fig. 4.30: Defects observed for biaxial NCF, gaping in hemisphere forming (a) experiment (b) simulation, and square box forming (c) experiment (d) simulation

4.4 Summary of Chapter 4

This chapter firstly presents an investigation of experimental forming tests on UD and biaxial NCF with different placed fiber orientations and punch shapes. A comprehensive analysis is conducted, considering punch forces, outer contour, macroscopic strains, and forming defects. The differences between UD and biaxial NCF are analyzed. Numerical simulations of the forming process on these different shapes are then performed using the presented mesoscopic finite element model of biaxial NCF. The accuracy of the models is validated by comparing the outer contour of the final configuration and shear angle with the experimental results. The occurrence of gaping defects is further analyzed and compared. It is found that the tetrahedron and square box shapes introduce more challenges, particularly at the corners where gaping can be observed after forming. The inter-ply sliding can also be observed which is an advantage of the mesoscale modeling.

Conclusion and perspectives

Conclusion

A parametric meso-scale FE model of biaxial NCF is generated based on the real geometry from the tomography results. The stitch's geometry is explicitly described and can be easily adjusted through the input geometrical parameters. The model considers the fiber yarns as a continuous medium and models them using solid elements, while the surrounding stitches are represented separately using beam elements. To accurately simulate the mesoscopic scale, the mechanical behavior of individual yarns and stitches are identified through dedicated mechanical tests, such as longitudinal shear tests on a fiber yarn, traction tests, and bending tests on a single stitch. An additional beam element is integrated into the solid elements of the yarn to account for its bending behavior, and yarn bending tests are conducted accordingly. A unique pretension step is defined to replicate the knitting of stitches and model the interaction between the yarns and stitches, considering the slip mechanisms in NCF.

The in-plane shear simulations on a unit cell model and on a bias-extension test model of biaxial NCF demonstrate the model's ability to detect local deformation. The tensioned and loose stitch segments, as well as the sliding between fiber yarns and stitches can be observed. The model also accurately predicts the evolution of gap widths and fiber yarns, which is compared closely with experimental measurements. Additionally, the model shows good agreement in normalized shear forces, indicating its capability for virtual material testing and potentially reducing the need for extensive experimental characterization tests in macroscopic simulations.The model's functionality extends to simulating and optimizing the forming process. A comparison of shear angles and outer contours of the fabric after forming using different punch shapes is presented. gaping defects can be observed which is a main advantage of this model. However, it is important to note that the computational demands of the mesoscopic model are substantial, and further optimization efforts are necessary for improved efficiency.

Perspectives

Several avenues of research could enrich these results:

- The hyperelastic model for the fiber yarn is insufficient to express the bending stiffness of the single fibers. The fiber yarn is modelled by an additional embedded beam element in this study which is an artificial approach. A second gradient approach could be developed instead to correctly describe the influence of both the bending stiffness of the fibres and the slip between the fibres.
- A pretension step is defined in this study and a thermal strain coefficient is defined for the stitches through a trial-and-error approach. Further tests like tow pull-out test can be conducted to understand the interaction between yarns and stitches and give an accurate thermal strain value.
- One notable challenge in mesoscopic simulation is the significant computational cost. A forming simulation on quarter size specimen model already requires one week to complete. It becomes evident that optimizing the computational cost is imperative for the practical and efficient application of the model in a broader context.
- The gaping defects are observable in the experimental results, but measuring them can be challenging due to the fabric's three-dimensional shape and the camera's two-dimensional perspective. Approach for measuring gaping is needed in order to compare it with the simulation results.

Appendices

APPENDIX A

List of publications

A.1 Conferences

1. International ESAFORM Conference 2023, 19-21 April 2023, Kraków, Poland
2. International conference on composite materials, 30 July - 4 August 2023, Belfast

A.2 Articles

1. Ruochen, Zheng & Schäfer, Bastian & Auriane, Platzer & Julien, Colmars & Naim, Naouar & Philippe, Boisse. (2023). A unit-cell mesoscale modelling of biaxial non-crimp-fabric based on a hyperelastic approach. 285-292. 10.21741/9781644902479-31.
2. Schäfer, Bastian & Ruochen, Zheng & Philippe, Boisse & Kärger, Luise. (2023). Investigation of the compaction behavior of uni- and bidirectional non-crimp fabrics. 331-338. 10.21741/9781644902479-36.
3. Schäfer, B., Zheng, R., Naouar, N. et al. Membrane behavior of uni- and bidirectional non-crimp fabrics in off-axis-tension tests. Int J Mater Form 16, 68 (2023). 10.1007/s12289-023-01792-x

Bibliography

[1] B. Chen. “Stress resultant shell approaches for simulations of textile composite reinforcement forming”. PhD thesis. INSA de Lyon, 2022 (cit. on pp. 9, 26, 65).

[2] T. Grieser and P. Mitschang. “Investigation of the compaction behavior of carbon fiber NCF for continuous preforming processes”. In: *Polymer Composites* 38 (Nov. 2015), n/a–n/a (cit. on pp. 10, 29).

[3] D. Durville. “Simulation of the mechanical behaviour of woven fabrics at the scale of fibers”. In: *International Journal of Material Forming* 3 (Sept. 2010) (cit. on pp. 11, 35).

[4] G. Creech and A. Pickett. “Meso-modelling of Non-Crimp Fabric composites for coupled drape and failure analysis”. In: *Journal of Materials Science* 41 (Jan. 2006), pp. 6725–6736 (cit. on pp. 11, 39–41, 52, 70).

[5] F. Schirmaier et al. “A macroscopic approach to simulate the forming behaviour of stitched unidirectional non-crimp fabrics (UD-NCF)”. In: *Composites Part A: Applied Science and Manufacturing* 102 (2017), pp. 322–335 (cit. on pp. 12, 44, 45).

[6] S. Bel et al. “Finite element model for NCF composite reinforcement preforming: Importance of inter-ply sliding”. In: *Composites Part A: Applied Science and Manufacturing* 43.12 (2012), pp. 2269–2277 (cit. on pp. 29, 70).

[7] A. Schnabel and T. Gries. “1 - Production of non-crimp fabrics for composites”. In: *Non-Crimp Fabric Composites*. Ed. by S. V. Lomov. Woodhead Publishing Series in Composites Science and Engineering. Woodhead Publishing, 2011, pp. 3–41 (cit. on p. 30).

[8] M. Ashir et al. “Development of innovative adaptive 3D Fiber Reinforced Plastics based on Shape Memory Alloys”. In: *Composites Science and Technology* 126 (2016), pp. 43–51 (cit. on pp. 29, 100).

[9] T. Ghafour. “Analyse des irréversibilités lors de la mise en forme des renforts de composites”. PhD thesis. Nov. 2018 (cit. on p. 30).

[10] S. MATHIEU. “MODÉLISATION DU COMPORTEMENT MÉCANIQUE LORS DU PROCÉDÉ DE MISE EN FORME ET PYROLYSE DES INTERLOCKS CMC”. PhD thesis. INSA de Lyon, 2014 (cit. on pp. 31, 38).

[11] M. E. Alves Fidelis et al. “The effect of fiber morphology on the tensile strength of natural fibers”. In: *Journal of Materials Research and Technology* 2.2 (2013), pp. 149–157 (cit. on p. 34).

[12] A. E. Engelbrecht-Wiggans and A. L. Forster. “Analysis of strain correction procedures for single fiber tensile testing”. In: *Composites Part A: Applied Science and Manufacturing* 167 (2023), p. 107411 (cit. on p. 34).

[13] J. W. Hearle. *High-performance fibres*. Elsevier, 2001 (cit. on p. 34).

[14] J. Hughes. “Strength and modulus of current carbon fibres”. In: *Carbon* 24.5 (1986). Proceedings of the Conference on Strength and Structural in Carbons and Graphites, pp. 551–556 (cit. on p. 34).

[15] A. C1557. “Standard Test Method for Tensile Strength and Young’s Modulus of Fibers”. In: () (cit. on p. 34).

[16] A. D3822. “Standard test method for tensile properties of single textile fibres Fibers”. In: () (cit. on p. 34).

[17] J. Huether et al. “An enhanced method to determine the Young’s modulus of technical single fibres by means of high resolution digital image correlation”. In: *Measurement Science and Technology* 29 (Dec. 2017) (cit. on p. 34).

[18] D. Depuydt et al. “Digital image correlation as a strain measurement technique for fibre tensile tests”. In: *Composites Part A: Applied Science and Manufacturing* 99 (2017), pp. 76–83 (cit. on p. 34).

[19] G. Zhou, X. Sun, and Y. Wang. “Multi-chain digital element analysis in textile mechanics”. In: *Composites Science and Technology* 64.2 (2004), pp. 239–244 (cit. on pp. 34, 35).

[20] F. Desplentere et al. “Micro-CT characterization of variability in 3D textile architecture”. In: *Composites Science and Technology* 65.13 (2005), pp. 1920–1930 (cit. on p. 36).

[21] N. Naouar et al. “3D composite reinforcement meso F.E. analyses based on X-ray computed tomography”. In: *Composite Structures* 132 (2015), pp. 1094–1104 (cit. on pp. 36, 48, 49).

[22] P. Badel et al. “Simulation and tomography analysis of textile composite reinforcement deformation at the mesoscopic scale”. In: *Composites Science and Technology* 68.12 (2008). Deformation and Fracture of Composites: Analytical, Numerical and Experimental Techniques, with regular papers, pp. 2433–2440 (cit. on pp. 36, 37, 84).

[23] P. Latil et al. “Towards the 3D in situ characterisation of deformation micromechanisms within a compressed bundle of fibres”. In: *Composites Science and Technology* 71.4 (2011), pp. 480–488 (cit. on p. 36).

[24] E. Maire and P. J. Withers. “Quantitative X-ray tomography”. In: *International Materials Reviews* 59.1 (2014), pp. 1–43 (cit. on p. 36).

[25] N. Naouar. “Analyse mésoscopique par éléments finis de la déformation de renforts fibreux 2D et 3D à partir de microtomographies X”. Theses. INSA de Lyon, Sept. 2015 (cit. on pp. 36, 49, 50).

[26] F. Dumont. “Contribution à l’expérimentation et à la modélisation du comportement mécanique de renforts de composites tissés”. PhD thesis. INSA de Lyon, 2003 (cit. on pp. 36, 37).

[27] A. Gasser, P. Boisse, and S. Hanklar. “Mechanical behaviour of dry fabric reinforcements. 3D simulations versus biaxial tests”. In: *Computational Materials Science* 17.1 (2000), pp. 7–20 (cit. on p. 37).

[28] P. Potluri and T. Sagar. “Compaction modelling of textile preforms for composite structures”. In: *Composite Structures* 86.1 (2008). Fourteenth International Conference on Composite Structures, pp. 177–185 (cit. on pp. 37, 38).

[29] F. C. Eugène Cosserat. “Théorie des Corps déformables”. In: *Nature* (1909) (cit. on p. 39).

[30] R. Mindlin. “Second gradient of strain and surface-tension in linear elasticity”. In: *International Journal of Solids and Structures* 1.4 (1965), pp. 417–438 (cit. on p. 39).

[31] M. Magno and J.-F. Ganghoffer. “Un modèle mésoscopique en grandes perturbations de matériaux textiles – Application à l’armure toile”. In: *Comptes Rendus de l’Académie des Sciences - Series IIB - Mechanics* 329.2 (2001), pp. 149–152 (cit. on p. 39).

[32] I. Azehaf. “Modélisation du comportement mécanique et de la perméabilité des renforts tissés”. In: 2017 (cit. on p. 39).

[33] S. Bickerton et al. “Investigation of draping and its effects on the mold filling process during manufacturing of a compound curved composite part”. In: *Composites Part A: Applied Science and Manufacturing* 28.9 (1997), pp. 801–816 (cit. on p. 41).

[34] B. Schäfer et al. “Investigation of the compaction behavior of uni- and bidirectional non-crimp fabrics”. In: Apr. 2023, pp. 331–338 (cit. on pp. 41, 42).

[35] J. Cao et al. “Characterization of mechanical behavior of woven fabrics: Experimental methods and benchmark results”. In: *Composites Part A: Applied Science and Manufacturing* 39.6 (2008), pp. 1037–1053 (cit. on pp. 41, 43, 78–80, 82).

[36] X. Peng et al. “Experimental and numerical analysis on normalization of picture frame tests for composite materials”. In: *Composites Science and Technology* 64.1 (2004), pp. 11–21 (cit. on p. 41).

[37] P. Harrison, M. Clifford, and A. Long. “Shear characterisation of viscous woven textile composites: a comparison between picture frame and bias extension experiments”. In: *Composites Science and Technology* 64.10 (2004), pp. 1453–1465 (cit. on pp. 41, 43).

[38] I. Taha, Y. Abdin, and S. Ebeid. “Comparison of picture frame and Bias-Extension tests for the characterization of shear behaviour in natural fibre woven fabrics”. In: *Fibers and Polymers* 14 (Feb. 2013) (cit. on p. 42).

[39] L. Li et al. “In-plane shear investigation of biaxial carbon non-crimp fabrics with experimental tests and finite element modeling”. In: *Materials Design* 63 (2014), pp. 757–765 (cit. on pp. 43, 82).

[40] B. Ben Boubaker, B. Haussy, and J. Ganghoffer. “Discrete models of woven structures. Macroscopic approach”. In: *Composites Part B: Engineering* 38.4 (2007), pp. 498–505 (cit. on pp. 43, 44).

[41] D. Jauffres et al. “Discrete mesoscopic modeling for the simulation of woven-fabric reinforcement forming”. In: *International Journal of Material Forming* 3 (Sept. 2010), pp. 1205–1216 (cit. on pp. 43, 44).

[42] M. Khan et al. “Numerical and experimental analyses of woven composite reinforcement forming using a hypoelastic behaviour. Application to the double dome benchmark”. In: *Journal of Materials Processing Technology* 210.2 (2010), pp. 378–388 (cit. on p. 44).

[43] X. Peng and J. Cao. “A continuum mechanics-based non-orthogonal constitutive model for woven composite fabrics”. In: *Composites Part A: Applied Science and Manufacturing* 36.6 (2005), pp. 859–874 (cit. on p. 44).

[44] X. Peng and Z. U. Rehman. “Textile composite double dome stamping simulation using a non-orthogonal constitutive model”. In: *Composites Science and Technology* 71.8 (2011), pp. 1075–1081 (cit. on p. 44).

[45] A. Charmetant, E. Vidal-Sallé, and P. Boisse. “Hyperelastic modelling for mesoscopic analyses of composite reinforcements”. In: *Composites Science and Technology* 71.14 (2011), pp. 1623–1631 (cit. on pp. 44, 57–59).

[46] E. Guzman-Maldonado et al. “Thermomechanical analysis, modelling and simulation of the forming of pre-impregnated thermoplastics composites”. In: *Composites Part A: Applied Science and Manufacturing* 78 (2015), pp. 211–222 (cit. on p. 44).

[47] E. Guzman-Maldonado et al. “Simulation of thermoplastic prepreg thermoforming based on a visco-hyperelastic model and a thermal homogenization”. In: *Materials Design* 93 (2016), pp. 431–442 (cit. on p. 44).

[48] P. Boisse, B. Zouari, and J.-L. Daniel. “Importance of in-plane shear rigidity in finite element analyses of woven fabric composite preforming”. In: *Composites Part A: Applied Science and Manufacturing* 37.12 (2006). The 11th US–Japan Conference on Composite Materials, pp. 2201–2212 (cit. on p. 44).

[49] N. Hamila, P. Boisse, and S. Chatel. “Semi-Discrete Shell Finite Elements for Textile Composite Forming Simulation”. In: *International Journal of Material Forming* 2 (Aug. 2009), pp. 169–172 (cit. on p. 44).

[50] N. Naouar et al. “Meso-FE modelling of textile composites and X-ray tomography”. In: *Journal of Materials Science* 55 (2020), 16969–16989 (cit. on pp. 48, 49).

[51] Krieger et al. “Shear and drape behavior of non-crimp fabrics based on stitching geometry”. In: *International Journal of Material Forming Official Journal of the European Scientific Association for Material Forming Esaform* (2018) (cit. on p. 48).

[52] F Robitaille et al. “Geometric modelling of industrial preforms: Warp-knitted textiles”. In: *Proceedings of the Institution of Mechanical Engineers, Part L: Journal of Materials: Design and Applications* 214.2 (2000), pp. 71–90 (cit. on p. 48).

[53] S. Lomov et al. “Nesting in textile laminates: geometrical modelling of the laminate”. In: *Composites Science and Technology* 63.7 (2003), pp. 993–1007 (cit. on p. 48).

[54] G. Jiang et al. “Geometric Model for Multi-axial Warp-knitted Fabric Based on NURBS”. In: *Fibres and Textiles in Eastern Europe* 105 (May 2014), pp. 91–97 (cit. on p. 48).

[55] W. Wu and W. Li. “Parametric modeling based on the real geometry of glass fiber unidirectional non-crimp fabric”. In: *Textile Research Journal* 89 (Jan. 2019), p. 004051751882484 (cit. on pp. 48, 52).

[56] A. Long and L. Brown. “8 - Modelling the geometry of textile reinforcements for composites: TexGen”. In: *Composite Reinforcements for Optimum Performance*. Ed. by P. Boisse. Woodhead Publishing Series in Composites Science and Engineering. Woodhead Publishing, 2011, pp. 239–264 (cit. on p. 49).

[57] I. Verpoest and S. V. Lomov. “Virtual textile composites software WiseTex: Integration with micro-mechanical, permeability and structural analysis”. In: *Composites Science and Technology* 65.15 (2005). 20th Anniversary Special Issue, pp. 2563–2574 (cit. on pp. 49, 50).

[58] S. Lomov et al. “Meso-level textile composites simulations: Open data exchange and scripting”. In: *Journal of Composite Materials* 48 (Feb. 2014), pp. 621–637 (cit. on p. 49).

[59] Y. Liu et al. “Prediction of linear and non-linear behavior of 3D woven composite using mesoscopic voxel models reconstructed from X-ray micro-tomography”. In: *Composite Structures* 179 (2017), pp. 568–579 (cit. on p. 49).

[60] S. Lomov. “4 - Understanding and modelling the effect of stitching on the geometry of non-crimp fabrics”. In: *Non-Crimp Fabric Composites*. Ed. by S. V. Lomov. Woodhead Publishing Series in Composites Science and Engineering. Woodhead Publishing, 2011, pp. 84–102 (cit. on p. 49).

[61] J. e. a. Schindelin. “Fiji: an open-source platform for biological-image analysis”. In: *Nature Methods* 9.7 (2012), pp. 676–682 (cit. on p. 50).

[62] C. Chen and S. Cheng. “Mechanical Properties of Fiber Reinforced Composites”. In: *Journal of Composite Materials* 1.1 (1967), pp. 30–41 (cit. on p. 52).

[63] S. Lomov et al. “Textile composites: modelling strategies”. In: *Composites Part A: Applied Science and Manufacturing* 32.10 (2001), pp. 1379–1394 (cit. on p. 52).

[64] T. Ishikawa and T.-W. Chou. “Nonlinear Behavior of Woven Fabric Composites”. In: *Journal of Composite Materials* 17.5 (1983), pp. 399–413 (cit. on p. 52).

[65] P. Qiao and J. Wang. “Transverse Shear Stiffness of Composite Honeycomb Cores and Efficiency of Material”. In: *Mechanics of Advanced Materials and Structures* 12.2 (2005), pp. 159–172 (cit. on p. 52).

[66] H.-J. Chun, H.-W. Kim, and J.-H. Byun. “Effects of through-the-thickness stitches on the elastic behavior of multi-axial warp knit fabric composites”. In: *Composite Structures* 74.4 (2006), pp. 484–494 (cit. on p. 52).

[67] D. Goyal et al. “Effect of Various Parameters on Effective Engineering Properties of 2 × 2 Braided Composites”. In: *Mechanics of Advanced Materials and Structures* 12.2 (2005), pp. 113–128 (cit. on p. 52).

[68] S. Lomov. “4 - Understanding and modelling the effect of stitching on the geometry of non-crimp fabrics”. In: *Non-Crimp Fabric Composites*. Ed. by S. V. Lomov. Woodhead Publishing Series in Composites Science and Engineering. Woodhead Publishing, 2011, pp. 84–102 (cit. on p. 55).

[69] X. Peng and J. Cao. “A dual homogenization and finite element approach for material characterization of textile composites”. In: *Composites Part B: Engineering* 33.1 (2002), pp. 45–56 (cit. on p. 57).

[70] S. V. Lomov et al. “Meso-FE modelling of textile composites: Road map, data flow and algorithms”. In: *Composites Science and Technology* 67.9 (2007), pp. 1870–1891 (cit. on p. 57).

[71] A. Bower. *Applied Mechanics of Solids*. Oct. 2009, pp. 1–795 (cit. on p. 58).

[72] “Chapter 4 Hyperelasticity”. In: *Mathematical Elasticity Volume I: Three-Dimensional Elasticity*. Ed. by P. G. Ciarlet. Vol. 20. Studies in Mathematics and Its Applications. Elsevier, 1988, pp. 137–198 (cit. on p. 58).

[73] P. Boisse et al. “Bending and wrinkling of composite fiber preforms and prepregs. A review and new developments in the draping simulations”. In: *Composites Part B: Engineering* 141 (2018), pp. 234–249 (cit. on pp. 60, 61).

[74] Q. Steer et al. “Modeling and analysis of in-plane bending in fibrous reinforcements with rotation-free shell finite elements.” In: *International Journal of Solids and Structures* 222-223 (2021), p. 111014 (cit. on p. 60).

[75] A. Madeo et al. “Thick fibrous composite reinforcements behave as special second-gradient materials: three-point bending of 3D interlocks”. In: *Zeitschrift für angewandte Mathematik und Physik* (2015) (cit. on p. 60).

[76] O. Döbrich et al. “Decoupling the bending behavior and the membrane properties of finite shell elements for a correct description of the mechanical behavior of textiles with a laminate formulation”. In: *Journal of Industrial Textiles* 44 (2014), pp. 70 –84 (cit. on p. 60).

[77] A. Charmetant. “Approches hyperélastiques pour la modélisation du comportement mécanique de préformes tissées de composites”. In: 2011 (cit. on pp. 62, 85).

[78] A. Iwata et al. “Coupled meso-macro simulation of woven fabric local deformation during draping”. In: *Composites Part A: Applied Science and Manufacturing* 118 (2019), pp. 267–280 (cit. on pp. 62, 63, 66).

[79] S. V. Lomov et al. “Compression resistance and hysteresis of carbon fibre tows with grown carbon nanotubes/nanofibres”. In: *Composites Science and Technology* 71.15 (2011), pp. 1746–1753 (cit. on p. 62).

[80] P. Potluri and T. Sagar. “Compaction modelling of textile preforms for composite structures”. In: *Composite Structures* 86.1 (2008). Fourteenth International Conference on Composite Structures, pp. 177–185 (cit. on p. 62).

[81] F. F. T. Peirce B.Sc. F.Inst.P. “26—THE “HANDLE” OF CLOTH AS A MEASURABLE QUANTITY”. In: *Journal of the Textile Institute Transactions* 21.9 (1930), T377–T416 (cit. on p. 65).

[82] P. Boisse et al. “Bending and wrinkling of composite fiber preforms and prepregs. A review and new developments in the draping simulations”. In: *Composites Part B: Engineering* 141 (2018), pp. 234–249 (cit. on p. 65).

[83] R. Bai et al. “Physics-based evaluation of the drapability of textile composite reinforcements”. In: *Composites Part B: Engineering* 242 (2022), p. 110089 (cit. on pp. 65, 101).

[84] M. Ghazimoradi et al. “Characterizing the macroscopic response and local deformation mechanisms of a unidirectional non-crimp fabric”. In: *Composites Part A: Applied Science and Manufacturing* 156 (2022), p. 106857 (cit. on p. 65).

[85] R. ten Thije and R. Akkerman. “Finite element simulation of draping with non-crimp fabrics”. English. In: *Proceedings of the 15th ICCM Conference (ICCM-15) 27 June-1 July 2005, Durban, South-Africa*. Ed. by V. Verijenko et al. 15th International Conference on Composite Materials, ICCM-15, 2005, ICCM ; Conference date: 27-06-2005 Through 01-07-2005. Elsevier, June 2005 (cit. on p. 70).

[86] S. Kawabata, M. Niwa, and H. Kawai. “5—THE FINITE-DEFORMATION THEORY OF PLAIN-WEAVE FABRICS. PART III: THE SHEAR-DEFORMATION THEORY”. In: *The Journal of The Textile Institute* 64.2 (1973), pp. 62–85 (cit. on p. 78).

[87] K. Buet Gautier. “Analyse et simulation du comportement mecanique des renforts composites tisses”. Thèse de doctorat dirigée par Boisse, Philippe Sciences appliquées Orléans 1998. PhD thesis. 1998, 129 P. (Cit. on p. 78).

[88] A. Willems et al. “Optical strain fields in shear and tensile testing of textile reinforcements”. In: *Composites Science and Technology* 68.3 (2008), pp. 807–819 (cit. on p. 78).

[89] B. Schäfer et al. “Investigation of the compaction behavior of uni- and bidirectional non-crimp fabrics”. In: Apr. 2023, pp. 331–338 (cit. on p. 78).

[90] L. Li et al. “In-plane shear investigation of biaxial carbon non-crimp fabrics with experimental tests and finite element modeling”. In: *Materials & Design* 63 (2014), pp. 757–765 (cit. on p. 78).

[91] Q. Steer. “Modélisation de la mise en forme des renforts fibreux cousus (NCF) : Etude expérimentale et numérique de l’influence de la couture”. PhD thesis. Dec. 2019 (cit. on p. 78).

[92] G. Creech. “Mesoscopic Finite Element modelling of non-crimp fabrics for drape and failure analyses”. PhD thesis. 2006 (cit. on pp. 78, 79).

[93] S. Lomov et al. “Carbon composites based on multiaxial multiply stitched preforms. Part 3: Biaxial tension, picture frame and compression tests of the preforms”. In: *Composites Part A: Applied Science and Manufacturing* 36.9 (2005), pp. 1188–1206 (cit. on p. 79).

[94] X. Peng et al. “Experimental and numerical analysis on normalization of picture frame tests for composite materials”. In: *Composites Science and Technology* 64.1 (2004), pp. 11–21 (cit. on p. 80).

[95] S. Bel, P. Boisse, and F. Dumont. “Analyses of the Deformation Mechanisms of Non-Crimp Fabric Composite Reinforcements during Preforming”. In: *Applied Composite Materials - APPL COMPOS MATER* 19 (June 2012), pp. 1–16 (cit. on p. 80).

[96] P. Harrison, J. Wiggers, and A. Long. “Normalization of Shear Test Data for Rate-independent Compressible Fabrics”. In: *Journal of Composite Materials* 42.22 (2008), pp. 2315–2344 (cit. on p. 83).

[97] P. Badel, E. Vidal-Sallé, and P. Boisse. “Computational determination of in-plane shear mechanical behaviour of textile composite reinforcements”. In: *Computational Materials Science* 40.4 (2007), pp. 439–448 (cit. on p. 84).

[98] C. Miehe and J. Dettmar. “A framework for micro–macro transitions in periodic particle aggregates of granular materials”. In: *Computer Methods in Applied Mechanics and Engineering* 193.3 (2004), pp. 225–256 (cit. on p. 84).

[99] M. H. Kashani et al. “The Role of Intra-Yarn Shear in Integrated Multi-Scale Deformation Analyses of Woven Fabrics: A Critical Review”. In: *Critical Reviews in Solid State and Materials Sciences* 43.3 (2018), pp. 213–232 (cit. on p. 94).

[100] B. Zouari, J.-L. Daniel, and P. Boisse. “A woven reinforcement forming simulation method. Influence of the shear stiffness”. In: *Computers & Structures* 84.5 (2006), pp. 351–363 (cit. on p. 94).

[101] A. Hosseini et al. “Identifying the distinct shear wrinkling behavior of woven composite preforms under bias extension and picture frame tests”. In: *Composite Structures* 185 (2018), pp. 764–773 (cit. on p. 94).

[102] B. Chen et al. “A hypoelastic stress resultant shell approach for simulations of textile composite reinforcement forming”. In: *Composites Part A: Applied Science and Manufacturing* 149 (2021), p. 106558 (cit. on p. 101).

[103] E. Guzman-Maldonado et al. “Experimental and numerical analyses of the mechanical behavior during draping of non-orthogonal bi-axial non-crimp fabric composite reinforcements”. In: *Materials Design* 218 (2022), p. 110682 (cit. on p. 101).

[104] B. Schäfer et al. “Experimental analysis of the forming behavior of uni- and bidirectional non-crimp fabrics for different geometries”. In: *Composites Part B: Engineering* (submitted) (cit. on pp. 103, 104, 108, 111, 113–116).

[105] C. Eberl. *Digital Image Correlation and Tracking*. MATLAB Central File Exchange, 2023 (cit. on p. 103).

[106] A. Mallach et al. “Experimental comparison of a macroscopic draping simulation for dry non-crimp fabric preforming on a complex geometry by means of optical measurement”. In: *Journal of Composite Materials* 51.16 (2017), pp. 2363–2375 (cit. on p. 110).

[107] L. Kärger et al. “Prediction of forming effects in UD-NCF by macroscopic forming simulation – Capabilities and limitations”. In: *Proceedings of the 24th International Conference on Material Forming* (2021) (cit. on p. 110).

FOLIO ADMINISTRATIF

THESE DE L'INSA LYON, MEMBRE DE L'UNIVERSITE DE LYON

NOM : ZHENG
(avec précision du nom de jeune fille, le cas échéant)

DATE de SOUTENANCE : 14/12/2023

Prénoms : Ruochen

TITRE : Simulation de la mise en forme de renforts NCF de composites basée sur des approches mesoscopiques

NATURE : Doctorat

Numéro d'ordre : 2023ISAL0128

Ecole doctorale : Ecole Doctorale N°162 Mécanique, Energétique, Génie civil, Acoustique

Spécialité : Génie Mécanique

RESUME : Pour assurer une fabrication efficace et sans défauts des renforts en fibres, tout en minimisant les tests expérimentaux coûteux et longs, il est nécessaire de développer des techniques fiables de simulation et d'optimisation du processus de mise en forme. Les composites NCF offrent des performances structurelles exceptionnelles mais leur complexité de mise en forme découle de mécanismes de déformation spécifiques, notamment des motifs de couture complexes reliant les fibres entre elles. Dans cette étude, nous proposons une approche de modélisation mésoscopique traitant les mèches comme un milieu continu et représentant les coutures environnantes avec des éléments poutres pour capturer leurs caractéristiques de déformation. En utilisant une loi hyperélastique et une précontrainte pour simuler la tension due aux coutures, notre modèle est validé par des simulations de déformation en cisaillement et des bias-extension tests, permettant une caractérisation virtuelle des matériaux et réduisant les efforts expérimentaux. De plus, notre méthode fournit des descriptions explicites des mèches et des coutures, facilitant l'analyse de différents motifs de couture et la personnalisation des matériaux NCF pour des applications spécifiques. Nous introduisons également une méthode de post-traitement pour suivre l'orientation des fibres et détecter les défauts locaux tels que le "gaping", améliorant ainsi la qualité et l'efficacité de la fabrication.

MOTS-CLÉS : Renfort composite, modélisation par éléments finis, Echelle mesoscopique, Mise en forme

Laboratoire (s) de recherche : Laboratoire de Mécanique des Contacts et des Structures (LAMCOS), INSA-Lyon

Directeur de thèse: MORESTIN Fabrice

Président de jury : HIVET Gilles

Composition du jury : HIVET Gilles, MOULIN Nicolas, GAUTIER Karine, MORESTIN Fabrice, NAOUAR Naim, COLMARS Julien, PLATZER Auriane